



Universiteit  
Leiden  
The Netherlands

## Atmospheres of hot alien Worlds

Brogi, M.

### Citation

Brogi, M. (2014, June 5). *Atmospheres of hot alien Worlds*. Retrieved from <https://hdl.handle.net/1887/25873>

Version: Publisher's Version

License: [Licence agreement concerning inclusion of doctoral thesis in the Institutional Repository of the University of Leiden](#)

Downloaded from: <https://hdl.handle.net/1887/25873>

**Note:** To cite this publication please use the final published version (if applicable).

Cover Page



Universiteit Leiden



The handle <http://hdl.handle.net/1887/25873> holds various files of this Leiden University dissertation.

**Author:** Brogi, Matteo

**Title:** Atmospheres of hot alien Worlds

**Issue Date:** 2014-06-05

Atmospheres  
of  
hot alien Worlds



# Atmospheres of hot alien Worlds

Proefschrift

ter verkrijging van  
de graad van Doctor aan de Universiteit Leiden,  
op gezag van Rector Magnificus prof.mr. C.J.J.M. Stolker,  
volgens besluit van het College voor Promoties  
te verdedigen op donderdag 5 juni 2014  
klokke 10.00 uur

door

Matteo Brogi

geboren te Grosseto, Italië  
in 1983

Promotiecommissie

Promotors: Prof. dr. I. A. G. Snellen  
Prof. dr. C. U. Keller

Overige leden: Prof. dr. C. Dominik University of Amsterdam  
Prof. dr. K. Heng University of Bern  
Prof. dr. E. F. van Dishoeck  
Dr. M. A. Kenworthy  
Prof. dr. H. J. A. Röttgering

*Ai miei genitori,  
per aver creduto in me,  
permettendomi di realizzare un sogno*





---

# Contents

---

<b>1</b>	<b>Introduction</b>	<b>1</b>
1.1	Planet properties from transits and radial velocities . . . . .	2
1.2	Atmospheric characterization of exoplanets . . . . .	4
1.2.1	Atmospheres of transiting planets . . . . .	4
1.2.2	Challenges of space- and ground-based observations . . . . .	7
1.2.3	Ground-based, high resolution spectroscopy . . . . .	8
1.2.4	A novel data analysis . . . . .	10
1.3	Close-in planets and their environment . . . . .	10
1.3.1	From atmospheric escape to catastrophic evaporation . . . . .	12
1.4	This thesis . . . . .	12
<b>2</b>	<b>The orbital trail of the giant planet <math>\tau</math> Boötis b</b>	<b>17</b>
2.1	The CRIRES observations . . . . .	18
2.2	Data reduction and analysis . . . . .	19
2.2.1	Initial data reduction . . . . .	19
2.2.2	Removal of telluric line contamination . . . . .	19
2.2.3	Cross correlation and signal extraction . . . . .	21
2.3	The CO detection and the planet velocity trail . . . . .	23
2.4	The planet orbit and mass . . . . .	28
2.5	The planet atmosphere . . . . .	30
2.5.1	Atmospheric models . . . . .	30
2.5.2	Comparison of model spectra to the data . . . . .	31
2.6	Discussion . . . . .	32
2.6.1	Spin-orbit alignment . . . . .	32
2.6.2	Molecular abundances and lack of an inversion layer . . . . .	32
2.7	Conclusions . . . . .	33
<b>3</b>	<b>Detection of molecular absorption in the dayside of 51 Peg b?</b>	<b>37</b>
3.1	Introduction . . . . .	38
3.2	Observations and Data Reduction . . . . .	40
3.2.1	Telescope and instruments . . . . .	40
3.2.2	Basic data analysis . . . . .	40
3.2.3	Stellar subtraction . . . . .	41
3.2.4	Removal of the telluric contamination . . . . .	41
3.2.5	Atmospheric models . . . . .	42
3.2.6	Cross correlation . . . . .	42
3.3	The cross-correlation signal . . . . .	45
3.4	The non-detection on the third night . . . . .	48
3.4.1	Issues with instrument, data and data analysis . . . . .	48
3.4.2	Astrophysical causes . . . . .	50
3.5	Characterization of exoplanet 51 Peg b . . . . .	51

3.5.1	Planet mass and system inclination . . . . .	51
3.5.2	The atmosphere of 51 Pegasi b . . . . .	51
3.6	Conclusions and future prospects . . . . .	54
<b>4</b>	<b>CO and H<sub>2</sub>O in the atmosphere of the non-transiting planet HD 179949 b</b>	<b>59</b>
4.1	Introduction . . . . .	60
4.2	The system HD 179949 . . . . .	61
4.3	Observations and data analysis . . . . .	62
4.3.1	Telescope, instrument and observations . . . . .	62
4.3.2	Extraction of the one-dimensional spectra . . . . .	62
4.3.3	Bad-pixel correction and wavelength calibration . . . . .	63
4.3.4	Removal of telluric lines . . . . .	64
4.4	Extraction of the planet signal . . . . .	64
4.4.1	Model spectra . . . . .	66
4.4.2	Cross correlation and signal retrieval . . . . .	67
4.4.3	Degeneracies in the atmospheric models . . . . .	68
4.5	Results . . . . .	69
4.5.1	Single-molecule detections . . . . .	69
4.5.2	Planet mass and orbital inclination . . . . .	70
4.5.3	Statistical tests on the measured signal . . . . .	72
4.5.4	Constraints on the C/O ratio . . . . .	73
4.6	Discussion and future prospects . . . . .	76
<b>5</b>	<b>Evidence for the disintegration of KIC 12557548 b</b>	<b>83</b>
5.1	Introduction . . . . .	84
5.2	Analysis of <i>Kepler</i> data . . . . .	84
5.2.1	Transit light curve . . . . .	86
5.3	The dust model . . . . .	88
5.4	Results and discussion . . . . .	90
5.4.1	Dependence on depth . . . . .	91
5.4.2	Constraints on particle size . . . . .	91
5.4.3	The size of the parent body . . . . .	92
5.5	Conclusions . . . . .	92
<b>6</b>	<b>A search for rotation and atmospheric circulation in HD 189733 b</b>	<b>93</b>
6.1	Introduction . . . . .	94
6.2	Observations . . . . .	96
6.3	Data analysis . . . . .	97
6.3.1	Extraction of the one-dimensional spectra . . . . .	97
6.3.2	Correction of bad-pixels and odd-even effect . . . . .	97
6.3.3	Alignment of spectra and wavelength calibration . . . . .	98
6.3.4	Removal of the stellar spectrum . . . . .	99
6.3.5	Removal of telluric lines . . . . .	100
6.4	Modeling and extracting the planet signal . . . . .	101
6.4.1	Modeling the planet spectra . . . . .	101
6.4.2	Modeling the planet broadening profile . . . . .	102

6.4.3	Cross correlation and signal retrieval . . . . .	104
6.5	Results . . . . .	106
6.5.1	Planet signal from models with single trace gases . . . . .	106
6.5.2	Planet signal from models with all molecular species . . . . .	107
6.5.3	Impact of SYSREM algorithm on the measured signal . . . . .	109
6.5.4	Absence of signal in the partially-observed transit . . . . .	111
6.6	Discussion . . . . .	111
6.A	Modeling and removal of the stellar spectrum . . . . .	115
6.A.1	Creating the telluric spectrum . . . . .	115
6.A.2	Creating the stellar spectrum . . . . .	115
6.A.3	Fitting the CO lines . . . . .	116
6.A.4	Subtracting the CO lines . . . . .	116
<b>7</b>	<b>Future exoplanet characterization at high spectral resolution</b>	<b>117</b>
7.1	Advantages of high-resolution spectroscopy . . . . .	117
7.2	Current limits of high-resolution spectroscopy . . . . .	118
7.3	The coming years . . . . .	119
7.4	The next decade: Extremely Large Telescopes . . . . .	121
7.5	Final remarks . . . . .	123
	<b>Samenvatting</b>	<b>125</b>
	<b>Riepilogo</b>	<b>129</b>
	<b>List of publications</b>	<b>133</b>
	<b>Curriculum Vitae</b>	<b>135</b>
	<b>Acknowledgments</b>	<b>137</b>

# 1

---

## Introduction

---

The origin of planetary systems and the existence of life elsewhere in the Universe are arguably among the most fascinating subjects of modern astrophysics. For centuries mankind could only speculate about the existence of planets orbiting stars other than the Sun (exoplanets), and even in relatively modern times the technological challenges for discovering such bodies were too overwhelming. The last two decades revolutionized the field of exoplanets, so that we are currently living the golden era of their discoveries. Thanks to dedicated surveys and telescopes, operating both in space and from the ground, planet hunters have found more than a thousand objects<sup>1</sup>, and a sample three times bigger awaits confirmation.

Perhaps the most surprising characteristic of the known exoplanets is their diversity, which has no analogs in the Solar System. Figure 1.1 shows the known planets to date in a semi-major axis, planet mass diagram ( $a$ ,  $M_{\text{P}}$ ). The top-left corner of the diagram pictures a population of giant planets in very close orbits, much closer to their parent star than Mercury is to the Sun, which are called *hot Jupiters*. The existence of this population challenged the main-stream theories of planet formation and evolution at the time of the first discoveries (Mayor & Queloz 1995; Marcy & Butler 1996; Butler et al. 1997), and led to the introduction of planet migration during the early stages of planet formation (Lin et al. 1996; Rasio et al. 1996). A more recent surprise was the discovery of bodies intermediate between the size of the Earth and that of Uranus. Despite no such object is observed around the Sun, they seem to be the most common planets in our Galaxy (Fressin et al. 2013; Petigura et al. 2013).

The two examples above suggest that, in the general picture of planet formation and evolution, our Solar System is uncommon, and must be placed in context by deriving the properties of exoplanets as accurately as possible. These include their masses and radii, the orbital parameters, and the atmospheric structure and composition. Studying exoplanet atmospheres is a crucial task for identifying habitable planets and detecting possible signatures of life, which is one of the ultimate goals of exoplanet sciences.

Up to now, the majority of the exoplanet detections have been achieved by using two indirect methods, namely the radial velocity and transit techniques. The direct detection of a planet, which implies imaging the light of the planet separately from that of the host star, is instead a challenging task, which has only recently been demonstrated to be successful (Chauvin et al. 2005; Kalas et al. 2008; Marois et al. 2008). It is so far limited to young, self-luminous planets in large orbits (tens to hundreds of astronomical units), although state-of-the-art instruments such as SPHERE at the ESO Very Large Telescope (Beuzit et al. 2006) or the Gemini Planet Imager

---

<sup>1</sup>Source: [exoplanet.eu](http://exoplanet.eu)

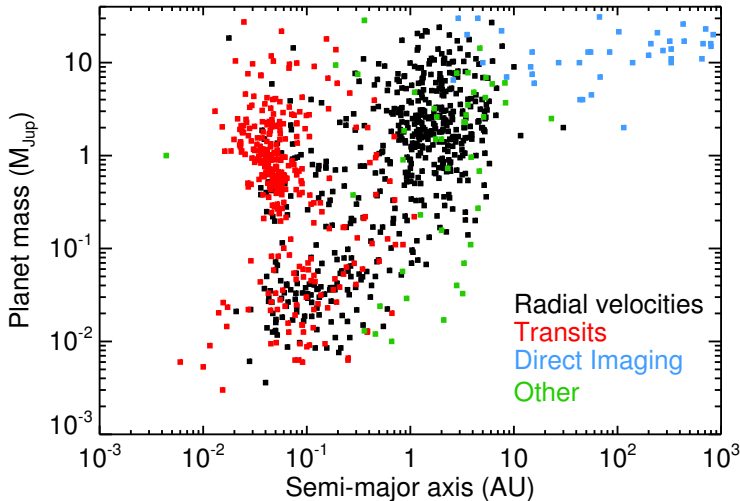


Figure 1.1: The known exoplanets to date in a semimajor axis-mass ( $a$ ,  $M_p$ ) diagram. The main discovery techniques are labeled with different colors. We note how transits and radial velocities are complementary in the mass range of giant planets, and how direct imaging is currently limited to massive planets on large orbits.

(Macintosh et al. 2006) will push the detection threshold towards more evolved systems and/or smaller orbits. For the remainder of this introductory Chapter, we will focus on the indirect methods for discovering and characterizing exoplanets.

## 1.1 Planet properties from transits and radial velocities

Due to the fact that a star and planet both orbit their common center of mass, the presence of the planet can be inferred from the periodic Doppler shift of the stellar spectral lines. By measuring the stellar radial-velocity curve, the orbital semi-major axis, period, and eccentricity can be determined. Due to the unknown orbital inclination  $i$ , only a lower limit on the planet mass ( $m \sin i$ ) can be derived, although this thesis presents a novel observational technique to overcome this limit (see Section 1.2.3).

If the orbit of an exoplanet is seen almost edge-on (i.e., the orbit is almost perpendicular to the plane of the sky), the planet crosses the disk of the parent star, which causes a detectable dimming of the stellar light. The depth and the shape of the transit light curve allows us to determine the orbital inclination, the semi-major axis, the orbital period, and the planet radius, but the planet mass remains generally unknown<sup>2</sup>.

When a planet is detected both in transit and through radial velocities, the planet

<sup>2</sup>It is sometimes possible to put mass constraints in multiple planets systems, by detecting transit-time variations due to the mutual gravitational interactions between the bodies.

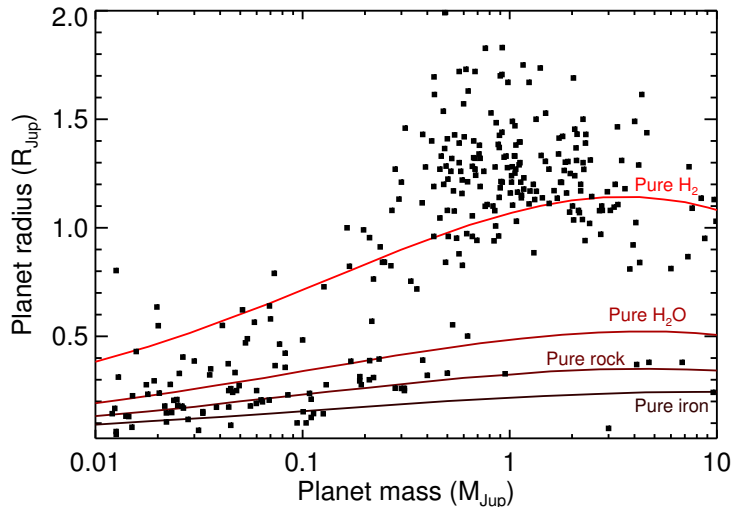


Figure 1.2: The known transiting exoplanets to date in a mass, radius ( $M_p$ ,  $R_p$ ) diagram. Theoretical phase curves for compositions ranging from pure iron to pure hydrogen are indicated. We note the significantly higher measured radii of most of the hot Jupiters, with respect to the theoretical values. For small planets and based on the mean density alone, it is impossible to disentangle the atmospheric composition (in particular the mass fraction of  $H_2$ ) from the planet interior. Finally, the smallest planets below the pure-iron curve have poorly-determined masses and radii, and could therefore move above the pure-iron curve within their  $1\sigma$  uncertainties.

mass and radius can both be measured. Therefore, the mean planet density can be computed, which is a fundamental parameter to constrain the internal composition of an exoplanet. However, the bulk density alone is often not enough. Figure 1.2 shows the confirmed transiting exoplanets in a mass-radius diagram. Their position in this diagram can be compared with theoretical predictions for the bulk composition, which are shown by the solid-line curves for pure hydrogen, pure water, pure silicate, and pure iron. The first anomaly which is seen is that giant planets have generally inflated radii, the main cause of which is still unclear (see, e.g., Spiegel & Burrows 2013), although it must be related to either extra heating of the planet interior (due to tidal dissipation and/or to ohmic heating) or to its slowed-down cooling (due to extra atmospheric opacity or heating), with stellar irradiation playing an important role in shaping the vertical thermal structure of the atmosphere. In addition, based on their radii and masses alone, it is impossible to robustly infer the internal composition of the smallest exoplanets (Adams et al. 2008). For instance, a water-dominated planet would have the same density as a planet with a rocky core and a hydrogen-rich envelope. The above mass-radius degeneracy also affects the transition between rocky and gaseous planets, although recent work sets it in the range  $1.5\text{--}2.0 R_\oplus$  (Marcy et al. 2014; Rogers 2014). These limitations impact our

knowledge of the occurrence of rocky planets, and of their capability to accrete and retain water in close-in orbits. This is tightly connected to exoplanet habitability, and to the search for a true Earth-analog.

In principle, a better understanding of the exoplanet properties can be reached by accessing their atmospheres, which means measuring their composition and vertical structure. For example, it is possible to distinguish between hydrogen-rich and hydrogen-poor planets by measuring their transmission spectrum (Miller-Ricci et al. 2009), a technique presented in more detail in Section 1.2.1. Atmospheres are a key topic of exoplanet science, in particular when searching for habitable planets and the signatures of life (Seager 2013).

## 1.2 Atmospheric characterization of exoplanets

### 1.2.1 Atmospheres of transiting planets

The detection of transiting planets (Charbonneau et al. 2000) opened the way to atmospheric characterization, the basic principles of which are shown in Figure 1.3.

**Transit:** When the planet passes in front of the parent star, part of the stellar disk is masked, causing a decrease  $\Delta F_{\text{tr}}$  in the total light received from the system ( $F_{\text{tot}}$ ). This is proportional to the area of the occulting object:

$$\frac{\Delta F_{\text{tr}}}{F_{\text{tot}}} = \left( \frac{R_{\text{P}}}{R_{\text{S}}} \right)^2, \quad (1.1)$$

where  $R_{\text{P}}$  and  $R_{\text{S}}$  are the planet and stellar radius respectively, in the approximation that star and planet are spherical. During transit, a small fraction of the starlight also filters through the planet atmosphere, and gets imprinted by its atomic or molecular constituents. Since the opacity of the planet atmosphere changes as a function of wavelength, the size of the opaque planet disk is also changing. Therefore, by measuring the depth of the transit as a function of wavelength, it is possible to construct the *transmission spectrum* of a planet and infer the atmospheric composition.

The modulations in the transmission spectrum have an amplitude  $\delta F_{\text{tr}}$  proportional to the area of the optically-thin annulus of the planet atmosphere. The thickness of the annulus is typically  $n = 5-10$  times the atmospheric scale height  $H$ , which is given by

$$H = \frac{kT}{\mu_{\text{atm}}g}, \quad (1.2)$$

where  $k$  is Boltzmann's constant,  $T$  is the planet temperature,  $\mu_{\text{atm}}$  is the atmospheric mean molecular weight, and  $g$  is the surface gravity of the planet. Therefore, the expected signal is

$$\delta F_{\text{tr}} \simeq \frac{(R_{\text{P}} + nH)^2 - R_{\text{P}}^2}{R_{\text{S}}^2}. \quad (1.3)$$

For a typical hot Jupiter,  $H = 100-200$  km, meaning that  $\delta F_{\text{tr}} \approx 0.1\%$  at wavelengths corresponding to the highest atmospheric opacity.

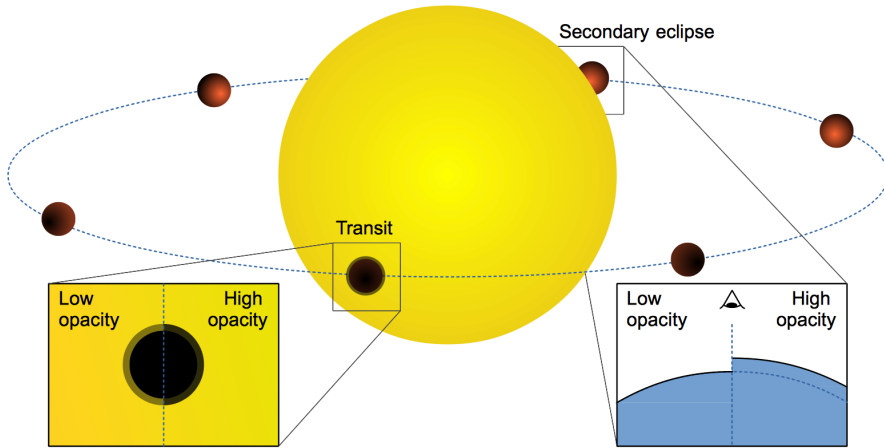


Figure 1.3: Geometry of a transiting planet. A transit occurs when the planet crosses the disk of the parent star, a secondary eclipse when the planet is occulted by the star. The zero planet orbital phase coincides with the mid-transit. The two insets show the effects of changing atmospheric opacity on the measured planet radius in transmission (left inset), and on the atmospheric height probed with secondary-eclipse measurements (right inset). The implications of these variations are further discussed in Section 1.2.1.

Via transmission spectroscopy, atomic sodium (Charbonneau et al. 2002), potassium (Sing et al. 2011a), hydrogen (Vidal-Madjar et al. 2003), carbon and oxygen (Vidal-Madjar et al. 2004) were detected in exoplanet atmospheres. Convincing molecular detections remained elusive until recently, mostly due to the strong debate in the community regarding the analysis of HST/NICMOS and Spitzer/IRAC data (see Section 1.2.2). Thanks to the Hubble/WFC3 (Deming et al. 2013; Mandell et al. 2013) and ground-based, high-resolution spectroscopy (Snellen et al. 2010), we now have a solid evidence of H<sub>2</sub>O and CO in transmission spectroscopy. Surprisingly, a considerable fraction of the observed transmission spectra are flat at both optical and near-infrared wavelengths (Gibson et al. 2013; Kreidberg et al. 2014), which likely requires the presence of clouds masking most of the spectral signatures. In addition, featureless optical transmission spectra and slopes consistent with Rayleigh scattering are strongly suggestive of haze (Sing et al. 2011b, 2013).

**Secondary eclipses:** At superior conjunction, the planet is eclipsed by the star. This also causes a dip in the light curve, because the contribution from the planet reflected light (in the optical) or thermal emission (in the near-infrared) is masked from the observer's view. The depth  $\Delta F_{\text{ecl}}$  of a secondary eclipse is generally much smaller than the transit depth. In the thermal regime, it can be estimated by

$$\frac{\Delta F_{\text{ecl}}(\lambda)}{F_{\text{tot}}(\lambda)} \simeq \frac{\mathcal{B}(\lambda, T_{\text{eq}})}{\mathcal{B}(\lambda, T_{\text{eff}})} \left( \frac{R_{\text{P}}}{R_{\text{S}}} \right)^2, \quad (1.4)$$

where  $\mathcal{B}(\lambda, T)$  is the Planck function at a wavelength  $\lambda$  and for a temperature  $T$ .  $T_{\text{eq}}$



and  $T_{\text{eff}}$  are the planet equilibrium temperature and the stellar effective temperature, respectively. A guess for the planet equilibrium temperature can be obtained by balancing the incoming stellar flux at the planet position with the outgoing planet emission in the hypothesis of black-body radiation:

$$T_{\text{eq}} \simeq T_{\text{eff}} \left[ \frac{(1 - A)R_{\text{S}}^2}{4a^2} \right]^{1/4}, \quad (1.5)$$

where  $A$  is the Bond albedo (the fraction of reflected starlight at all wavelengths), and  $a$  the orbital semi-major axis. For a typical hot Jupiter ( $T_{\text{eq}} = 1500$  K,  $a = 0.05$  AU,  $R_{\text{P}} = 1.2R_{\text{Jup}}$ ) orbiting a solar-type star the relative secondary eclipse depth is few times  $10^{-3}$ .

It is important to realize that, by measuring the secondary eclipse depth in the near-infrared, we are essentially probing the temperature of the layer at which the planet atmosphere becomes optically thin. Therefore, by repeating this exercise at various wavelengths, it is possible to detect the presence of atoms or molecules. At frequencies where the planet atmosphere is relatively transparent, we observe the radiation coming from deep layers, ideally from the level where the planet continuum is formed. In the presence of any source of opacity, the atmosphere will become optically thick at higher altitude for an observer looking from the outside (see right inset in Figure 1.3). If temperature decreases with pressure (non-inverted atmosphere), then the planet flux at wavelengths with increased opacity will be lower than the continuum flux (molecular absorption). If temperature increases with pressure (inverted atmosphere), the planet spectrum will show emission features. By measuring the planet flux (i.e., the secondary-eclipse depth) as a function of wavelength it is therefore possible to reconstruct the *dayside spectrum* of a planet. These observations are however very challenging. It is often necessary to measure a temperature difference of less than 500 K, which corresponds to a signal of  $\sim 10^{-4}$  in relative photometry. The thermal emission from an exoplanet was detected for the first time from space (Deming et al. 2005; Charbonneau et al. 2005), and only recently the first ground-based detections were reported (de Mooij & Snellen 2009; Anderson et al. 2010). Most of the information about exoplanet dayside spectra comes from observations with the *Spitzer Space Telescope* in the 3.6-24  $\mu\text{m}$  range (see Seager & Deming 2010, for a review). Despite the relatively big sample of about 20 exoplanets, these measurements still do not provide any clear evidence for thermal inversion layers, except in the case of HD 209458 b (Knutson et al. 2008). Moreover, the presence of molecular species ( $\text{H}_2\text{O}$ , CO, and possibly  $\text{CO}_2$ ) has been confidently assessed for two planets only, HD 189733 b and HD 209458 b (Madhusudhan & Seager 2009; Lee et al. 2012; Line et al. 2012).

At optical wavelengths, the planet/star contrast ratio is set by the planet radius, its orbital distance  $a$ , and its albedo  $A$ :

$$\frac{\Delta F_{\text{ecl}}}{F_{\text{tot}}} \simeq A \left( \frac{R_{\text{P}}}{2a} \right)^2 \quad (1.6)$$

Optical secondary eclipses have been detected thanks to dedicated transit space missions such as *CoRoT* and *Kepler* (Alonso et al. 2009; Snellen et al. 2009; Borucki et al.

2009; Désert et al. 2011; Demory et al. 2011). For the hottest exoplanets, the Wien tail of the thermal emission partially extends to optical wavelengths, complicating the disentanglement of emitted light from reflected light (Coughlin & López-Morales 2012).

**Phase curves:** Finally, by carefully monitoring the total light from the system as a function of planet orbital phase, it is possible to measure the changing contribution of the night- and the day-side of the planet. This gives insight on the energy balance between the two hemispheres, and it is in general connected to the mechanisms regulating the heat transport in the planet atmosphere (Cowan & Agol 2011). It also allows us to indirectly infer the presence of circulation patterns in the planet atmosphere (Knutson et al. 2012).

## 1.2.2 Challenges of space- and ground-based observations

Observations of exoplanet atmospheres require detecting signals at the very limit of instrumental possibilities, typically at planet/star contrasts ranging from  $10^{-3}$  to  $10^{-5}$ , normally using instruments not specifically designed for high precision measurements. This means that the level of systematic noise, due to imperfections in the instrument or in the observational strategy, is often comparable to or greater than the planet signal. The removal of such non-Gaussian noise is therefore one of the most crucial aspects of exoplanet atmospheric observations. For this reason, it is not surprising that the first successful studies were conducted from space, where the high instrumental stability and the absence of the contamination by the Earth's atmosphere reduce the impact of systematics.

On the other hand, optical and near-infrared space telescopes have smaller collective areas than their ground-based counterparts. Moreover, space instruments have a lower spectral resolution than ground-based facilities. Before my thesis work, for many of the studied exoplanets, the measured spectra were limited to a few broad photometric bands, encompassing a large number of spectral features. This makes it challenging to identify molecular species, or even to distinguish between emission or absorption features. This level of ambiguity, coupled with the low statistical significance of the detected spectral signatures, limits the determination of the atmospheric composition and vertical thermal structure (e.g., the presence or absence of a thermal inversion layer).

Ground-based telescopes benefit from larger apertures and much higher spectral resolution. On the other hand, absorption or scattering by our own atmosphere, as well as instrumental instability (e.g., variation of detector temperature, pointing, gravity vector, etc.) introduce systematic effects which are hard to remove. This means that in practice the photometric accuracy of ground based observations is usually one order of magnitude lower than for space-based measurements, with the exception of the work presented in this thesis. These limitations particularly affect the observations of secondary eclipses, which would otherwise benefit from the larger collective area of ground telescopes.

For both ground and space-based measurements, there is no general agreement regarding the best strategy for detrending systematic noise in the data. This led to

serious debate in the past years (Swain et al. 2008, 2010; Gibson et al. 2011; Mandell et al. 2011), and resulted in a great effort of the exoplanet community in order to design much more robust observational and data-analysis techniques. The next Section describes a novel technique, which forms the heart of my thesis work, based on ground-based, high-resolution spectroscopy. It is capable to robustly identify molecular species in exoplanet atmospheres, and it is almost unaffected by systematic noise at the typical S/N of current observations.

### 1.2.3 Ground-based, high resolution spectroscopy

Observations at very high spectral resolution ( $R \sim 100,000$ ) are only possible from the ground, because such high-resolution spectrographs are either too big to be launched in space, or require too large telescope apertures to reach sufficient S/N and be appealing for the broad astronomical community. This means that observations at very high spectral resolution are affected by the contamination of our own atmosphere (telluric contamination), which can be a factor of  $10^3$ - $10^4$  higher than the signal we are looking for.

On the other hand, high-dispersion observations bring a number of advantages, which are represented in Figure 1.4. It shows a simulated observation of a hot Jupiter around  $2.3 \mu\text{m}$ , targeting a ro-vibrational band of carbon monoxide. The first advantage of high-resolution spectroscopy is that the molecules are resolved into the individual lines, meaning that the identification of molecular features can be achieved robustly by line-matching. In this thesis (Chapters 2, 3, 4, and 6), we make use of cross correlation in order to extract and recognize the signal from a specific molecule. An additional advantage of high-dispersion observations is that the planet orbital motion is detected. In Figure 1.4, the changing Doppler shift of the planet molecular lines, due to the changing orbital radial velocity of the planet, is clearly visible. This allows us to effectively disentangle the telluric contamination (which is not subject to any Doppler-shift) from the planet signal, and to measure the planet radial velocity.

Transiting planets can be observed at high spectral resolution in transmission, or just before and after secondary eclipse, when their dayside hemisphere is facing the observer. More importantly, dayside spectroscopy can be applied to non-transiting planets as well via dayside spectroscopy, the reason being that the planet thermal spectrum is targeted directly. This means that, by coupling the maximum value of the planet and stellar radial velocities ( $K_P$  and  $K_S$  respectively), it is possible to measure the planet/star mass ratio:

$$\frac{M_P}{M_S} = \frac{K_S}{K_P}, \quad (1.7)$$

which allows us to solve for the true planet mass if the stellar mass is known. Furthermore, the orbital velocity of the planet can be computed from the Third Kepler's Law:

$$v_P = \left[ \frac{2\pi GM_S}{P(1 - M_P/M_S)} \right]^{1/3}. \quad (1.8)$$

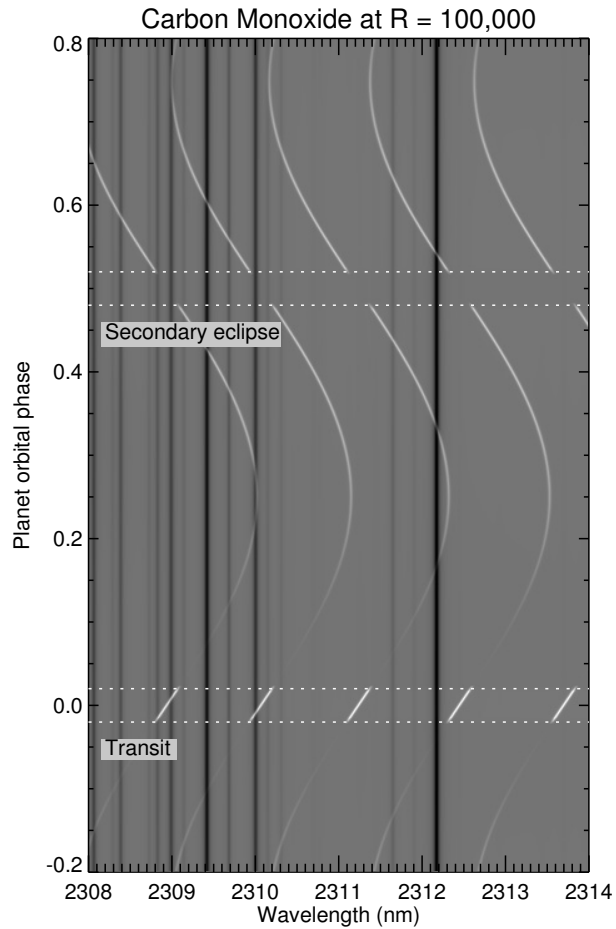


Figure 1.4: Toy model of the spectrum of a close-in, giant exoplanet observed at a spectral resolution of 100,000. Molecular absorption lines from CO in the planet atmosphere (plotted in white) are Doppler-shifted due to the changing component of the planet radial velocity. On the contrary, telluric lines (in black) are stationary in wavelength and can be effectively removed from the data while preserving the planet spectrum, as explained in Section 1.2.4.

This means that the orbital inclination can also be computed as

$$i = \sin^{-1} \left( \frac{K_P}{v_P} \right). \quad (1.9)$$

In this way, atmospheric characterization is also possible for non-transiting planets. This has been pioneered in my thesis work (Chapters 2, 3, and 4).

### 1.2.4 A novel data analysis

One of the most innovative aspects of our high-dispersion observations is the data analysis, which is summarized here, and described in details in Chapters 2 and 4. The spectral separation between the static telluric absorption and the Doppler-shifted planet signal allows us to self-calibrate the data in the following way. Firstly, we shift all the observed spectra to the same reference frame, which is for these near-infrared observations the telluric frame. With this choice, telluric lines always fall on the same position along the spectral direction (i.e., on the same pixel in the spectra), while the planet signal will appear at a certain wavelength only for a small fractions of the observations, due to the changing radial component of its orbital velocity. Therefore, by fitting the flux in each telluric line as a function of time, and dividing by the fit, we only alter the spectral signatures produced in the Earth's atmosphere, leaving the planet spectrum almost unaffected. The most obvious time dependence in our data is with geometric airmass. Second order effects are given by changes in precipitable water vapor, instrument resolution, etc. Although the normalization above removes any broad-band spectral features and any information on absolute fluxes (including the level of the planet continuum), it also effectively removes telluric absorption, with residual noise typically within  $\sim 10\%$  from the photon noise. Furthermore, we preserve the narrow component of the planet spectrum, i.e., the flux ratios between the core of the molecular lines and the planet continuum.

Since the planet signal is typically still buried in the noise at this stage, we utilize cross correlation with model spectra to combine all the molecular lines in the planet's spectrum in one single function (the cross-correlation function, or CCF). We compute the CCF as a function of radial velocity and time. Subsequently, we test all possible radial velocities for the observed planet and we sum the CCF in time, maximizing the total cross-correlation signal. This gives us the best-fitting planet radial velocity, which can be combined with the stellar radial velocity via Equation 1.7, and subsequently utilized to derive the planet mass and orbital inclination.

## 1.3 Close-in planets and their environment

Close-in giant planets (hot Jupiters) are the ideal test bench for observations of exoplanet atmospheres. Due to their high equilibrium temperatures ( $T_{\text{eq}} = 1500\text{-}3000\text{ K}$ ) and large radii, they have a favorable contrast with respect to the parent star. This is true not only for the signal from the dayside hemisphere, but also for the signal in transmission, which is increased by the large atmospheric scale height (see Equa-

tion 1.2). Therefore, it is not surprising that the current observations are mostly focused on hot Jupiters, and my thesis work does not break this trend.

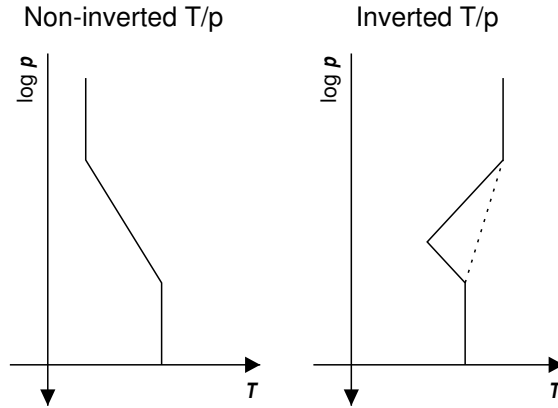


Figure 1.5: Schematic representation of the vertical structure of an exoplanet atmosphere, with (right panel) and without (left panel) a thermal inversion layer. The  $T/p$  profiles drawn with a solid line illustrate how temperature changes with pressure. When a thermal inversion layer forms (inverted  $T/p$ , right panel), temperature increases with altitude in a certain atmospheric region, while pressure always decreases with altitude. The profiles shown here have the same parametrization as the atmospheric models utilized in Chapters 2, 3, 4, and 6. In most cases, a simpler inverted profile can be assumed with no qualitative difference in the high-resolution model spectra (dashed line, right panel).

The high level of stellar irradiation is thought to be tightly connected to the onset of thermal inversion layers in hot-Jupiter atmospheres. These cause the temperature to increase with altitude in a certain pressure range of the planet atmosphere (see Figure 1.5). The most likely mechanism for thermal inversion is the presence of high-altitude, optical absorbers capable to block the incoming starlight and heat-up the surrounding medium. Fortney et al. (2008) proposed that the level of stellar irradiation could play a role, by preventing these compounds from condensing and rain out from the atmosphere. However, as time passed by, the emerging picture was a general lack of thermal inversion layers, with the best exception to date being HD 209458 b (Knutson et al. 2008). Knutson et al. (2010) suggested that stellar activity could also play a role, with the stellar UV flux capable to photo-dissociate high-altitude absorbers. More recently, Madhusudhan (2012) proposed that carbon-rich planets (i.e., planets having a C/O ratio greater than 1) might naturally lack thermal inversion layers, because the equilibrium abundances of oxides would be extremely small, with all the available oxygen fixed in CO.

The importance of determining the C/O ratio in exoplanet atmospheres is twofold, as this parameter could also reflect the natal planet environment in the protoplanetary disk (Öberg et al. 2011). The snow-lines of each of the major carbon- and oxygen-bearing molecules are located at different positions in the disk, mean-

ing that the C/O ratio is also expected to vary in both the gas and the condensed phase. This could produce variations in the C/O ratio of the primary atmospheres of forming giant exoplanets. We attempted to measure the atmospheric C/O ratio using ground-based, high-dispersion observations in Chapters 4 and 6. These results complement observations at low spectral resolution, which have so far been unable to put tight constraints on this quantity (Madhusudhan et al. 2011; Crossfield et al. 2012; Line et al. 2014).

### 1.3.1 From atmospheric escape to catastrophic evaporation

Due to the high level of stellar irradiation, hot Jupiters can also experience atmospheric escape, the detection of which was claimed for neutral atomic hydrogen (Vidal-Madjar et al. 2003; Lecavelier Des Etangs et al. 2010; Linsky et al. 2010) and for neutral or ionized metals (Vidal-Madjar et al. 2004; Astudillo-Defru & Rojo 2013).

Although the timescales of atmospheric loss are still unclear, a planet could in principle lose its entire gas envelope during the main-sequence lifetime of the parent star. A core of a former gaseous planet or a close-in rocky planet could then undergo evaporation, because the equilibrium temperatures of close-in planets are generally higher than the melting point of silicates and possibly of iron. The latest phases of the evaporation occur on a very short timescale, so that it is highly unlikely to observe such a stage (Perez-Becker & Chiang 2013). Nevertheless, a few candidates showing the signatures of evaporation have been found in the *Kepler* database (Rapaport et al. 2012, 2013). One of these peculiar objects is studied in Chapter 5 of this thesis.

## 1.4 This thesis

This thesis presents observations of the atmospheres of close-in, heavily irradiated planets. These range from ground-based, high-resolution spectroscopy of hot-Jupiter atmospheres to space-based, transit measurements of a putative disintegrating planet.

**Chapter 2** presents the first detection of the atmosphere of a non-transiting planet,  $\tau$  Boötis b, obtained by measuring dayside CO absorption at  $2.3 \mu\text{m}$  via high-resolution spectroscopy with CRIRES at the VLT. By tracing the planet radial velocity, we were able to solve for the planet mass and the orbital inclination, which we found to be  $M_{\text{P}} = (5.95 \pm 0.28) M_{\text{Jup}}$  and  $i = (44.5 \pm 1.5)$  degrees, respectively. Furthermore, by observing molecular spectral features in absorption, we were able to determine that temperature decreases with altitude in this planet atmosphere. This result appeared in Brogi et al. (2012b).

**Chapter 3** presents similar observations applied to 51 Pegasi b, the first exoplanet discovered around a main-sequence star. In this case,  $\text{H}_2\text{O}$  is also detected together with CO, and the measured planet mass is  $M_{\text{P}} = (0.46 \pm 0.02) M_{\text{Jup}}$ . Interestingly, the orbital inclination is found to be greater than  $79.6^\circ$ , which means that this planet might transit. However, no transit event is observed in any previous photometric monitoring, which sets an upper limit of  $82.2^\circ$  on the inclination. This work was

published in Brogi et al. (2013), and we recently confirmed the water vapor absorption via dayside spectroscopy at  $3.2 \mu\text{m}$  (Birkby et al. in preparation).

**Chapter 4** presents again  $2.3 \mu\text{m}$  dayside observations with VLT/CRIRES, which led to the detection of CO and H<sub>2</sub>O in the atmosphere of a third non-transiting planet, HD 179949 b. We measured a planet mass of  $(0.98 \pm 0.04) M_{\text{Jup}}$ , and an orbital inclination of  $(67.7 \pm 4.3)$  degrees. Moreover, in this study we show for the first time that it is possible to use high-resolution spectroscopy to measure relative molecular abundances in exoplanet atmospheres and constrain the C/O ratio. In the case of HD 179949 b, our data favors an oxygen-rich atmosphere ( $\text{C/O} < 1$ ) for the planet. These results are currently in press (Brogi et al. 2014).

**Chapter 5** shows the quantitative evidence for a disintegrating transiting planet around a star in the *Kepler* field, named KIC 12557548 b. We independently analyzed the *Kepler* photometry and phase-folded the data according to the transit depth. Furthermore, we modeled a trailing tail of dust grains including extinction and scattering, and we showed that such a model exquisitely fits the data. In particular, we were able to quantitatively explain peculiar features of the light curve, such as a flux excess before ingress (due to forward scattering) and a strong asymmetry in the transit shape (due to the tail of dust). By computing realistic scattering functions for silicate grains, we concluded that the typical size of the dust grains is on the order of  $\sim 0.1 \mu\text{m}$ . This work appeared in Brogi et al. (2012a).

**Chapter 6** pushes high-resolution spectroscopy with CRIRES to the limit, aiming for the detection of the planetary rotation of HD 189733 b, by means of transmission spectroscopy. Not only we detect the combined absorption signal of CO, CO<sub>2</sub>, and H<sub>2</sub>O, but we also show that the S/N is significantly increases when cross-correlating with template models including a line broadening consistent with a planet rotational velocity of  $\sim 2.7 \text{ km s}^{-1}$ , and corresponding to a rotational period of about 2.2 days, equal to the planet orbital period. This is in line with theoretical predictions that hot Jupiters become tidally synchronized on short timescales after their migration to a close-in orbit.

Finally, in **Chapter 7**, a brief overview of the future perspectives of high-resolution spectroscopy is presented. Among these, we highlight the possibility of detecting oxygen in terrestrial planets around M-dwarfs with future Extremely Large Telescopes, and to study most of the planets around bright stars, which will be found by missions like TESS.



## Bibliography

- Adams, E. R., Seager, S., & Elkins-Tanton, L. 2008, *ApJ*, 673, 1160
- Alonso, R., Guillot, T., Mazeh, T., et al. 2009, *A&A*, 501, L23
- Anderson, D. R., Gillon, M., Maxted, P. F. L., et al. 2010, *A&A*, 513, L3
- Astudillo-Defru, N. & Rojo, P. 2013, *A&A*, 557, A56
- Beuzit, J.-L., Feldt, M., Dohlen, K., et al. 2006, *The Messenger*, 125, 29
- Borucki, W. J., Koch, D., Jenkins, J., et al. 2009, *Science*, 325, 709
- Brogi, M., de Kok, R. J., Birkby, J. L., Schwarz, H., & Snellen, I. A. G. 2014, ArXiv e-prints
- Brogi, M., Keller, C. U., de Juan Ovelar, M., et al. 2012a, *A&A*, 545, L5
- Brogi, M., Snellen, I. A. G., de Kok, R. J., et al. 2012b, *Nature*, 486, 502
- Brogi, M., Snellen, I. A. G., de Kok, R. J., et al. 2013, *ApJ*, 767, 27
- Butler, R. P., Marcy, G. W., Williams, E., Hauser, H., & Shirts, P. 1997, *ApJL*, 474, L115
- Charbonneau, D., Allen, L. E., Megeath, S. T., et al. 2005, *ApJ*, 626, 523
- Charbonneau, D., Brown, T. M., Latham, D. W., & Mayor, M. 2000, *ApJL*, 529, L45
- Charbonneau, D., Brown, T. M., Noyes, R. W., & Gilliland, R. L. 2002, *ApJ*, 568, 377
- Chauvin, G., Lagrange, A.-M., Dumas, C., et al. 2005, *A&A*, 438, L25
- Coughlin, J. L. & López-Morales, M. 2012, *AJ*, 143, 39
- Cowan, N. B. & Agol, E. 2011, *ApJ*, 729, 54
- Crossfield, I. J. M., Barman, T., Hansen, B. M. S., Tanaka, I., & Kodama, T. 2012, *ApJ*, 760, 140
- de Mooij, E. J. W. & Snellen, I. A. G. 2009, *A&A*, 493, L35
- Deming, D., Brown, T. M., Charbonneau, D., Harrington, J., & Richardson, L. J. 2005, *ApJ*, 622, 1149
- Deming, D., Wilkins, A., McCullough, P., et al. 2013, *ApJ*, 774, 95
- Demory, B.-O., Seager, S., Madhusudhan, N., et al. 2011, *ApJL*, 735, L12
- Désert, J.-M., Charbonneau, D., Fortney, J. J., et al. 2011, *ApJS*, 197, 11
- Fortney, J. J., Lodders, K., Marley, M. S., & Freedman, R. S. 2008, *ApJ*, 678, 1419
- Fressin, F., Torres, G., Charbonneau, D., et al. 2013, *ApJ*, 766, 81

- Gibson, N. P., Aigrain, S., Barstow, J. K., et al. 2013, *MNRAS*, 428, 3680
- Gibson, N. P., Pont, F., & Aigrain, S. 2011, *MNRAS*, 411, 2199
- Kalas, P., Graham, J. R., Chiang, E., et al. 2008, *Science*, 322, 1345
- Knutson, H. A., Charbonneau, D., Allen, L. E., Burrows, A., & Megeath, S. T. 2008, *ApJ*, 673, 526
- Knutson, H. A., Howard, A. W., & Isaacson, H. 2010, *ApJ*, 720, 1569
- Knutson, H. A., Lewis, N., Fortney, J. J., et al. 2012, *ApJ*, 754, 22
- Kreidberg, L., Bean, J. L., Désert, J.-M., et al. 2014, *Nature*, 505, 69
- Lecavelier Des Etangs, A., Ehrenreich, D., Vidal-Madjar, A., et al. 2010, *A&A*, 514, A72
- Lee, J.-M., Fletcher, L. N., & Irwin, P. G. J. 2012, *MNRAS*, 420, 170
- Lin, D. N. C., Bodenheimer, P., & Richardson, D. C. 1996, *Nature*, 380, 606
- Line, M. R., Knutson, H., Wolf, A. S., & Yung, Y. L. 2014, *ApJ*, 783, 70
- Line, M. R., Zhang, X., Vasisht, G., et al. 2012, *ApJ*, 749, 93
- Linsky, J. L., Yang, H., France, K., et al. 2010, *ApJ*, 717, 1291
- Macintosh, B., Graham, J., Palmer, D., et al. 2006, in Society of Photo-Optical Instrumentation Engineers (SPIE) Conference Series, Vol. 6272
- Madhusudhan, N. 2012, *ApJ*, 758, 36
- Madhusudhan, N., Harrington, J., Stevenson, K. B., et al. 2011, *Nature*, 469, 64
- Madhusudhan, N. & Seager, S. 2009, *ApJ*, 707, 24
- Mandell, A. M., Drake Deming, L., Blake, G. A., et al. 2011, *ApJ*, 728, 18
- Mandell, A. M., Haynes, K., Sinukoff, E., et al. 2013, *ApJ*, 779, 128
- Marcy, G. W. & Butler, R. P. 1996, *ApJL*, 464, L147
- Marcy, G. W., Isaacson, H., Howard, A. W., et al. 2014, *ApJS*, 210, 20
- Marois, C., Macintosh, B., Barman, T., et al. 2008, *Science*, 322, 1348
- Mayor, M. & Queloz, D. 1995, *Nature*, 378, 355
- Miller-Ricci, E., Seager, S., & Sasselov, D. 2009, *ApJ*, 690, 1056
- Öberg, K. I., Murray-Clay, R., & Bergin, E. A. 2011, *ApJL*, 743, L16
- Perez-Becker, D. & Chiang, E. 2013, *MNRAS*, 433, 2294
- Petigura, E. A., Marcy, G. W., & Howard, A. W. 2013, *ApJ*, 770, 69

- Rappaport, S., Barclay, T., DeVore, J., et al. 2013, ArXiv e-prints
- Rappaport, S., Levine, A., Chiang, E., et al. 2012, *ApJ*, 752, 1
- Rasio, F. A., Tout, C. A., Lubow, S. H., & Livio, M. 1996, *ApJ*, 470, 1187
- Rogers, L. A. 2014, in IAU Symposium, Vol. 299, IAU Symposium, 247–251
- Seager, S. 2013, *Science*, 340, 577
- Seager, S. & Deming, D. 2010, *ARA&A*, 48, 631
- Sing, D. K., Désert, J.-M., Fortney, J. J., et al. 2011a, *A&A*, 527, A73
- Sing, D. K., Lecavelier des Etangs, A., Fortney, J. J., et al. 2013, *MNRAS*, 436, 2956
- Sing, D. K., Pont, F., Aigrain, S., et al. 2011b, *MNRAS*, 416, 1443
- Snellen, I. A. G., de Kok, R. J., de Mooij, E. J. W., & Albrecht, S. 2010, *Nature*, 465, 1049
- Snellen, I. A. G., de Mooij, E. J. W., & Albrecht, S. 2009, *Nature*, 459, 543
- Spiegel, D. S. & Burrows, A. 2013, *ApJ*, 772, 76
- Swain, M. R., Deroo, P., Griffith, C. A., et al. 2010, *Nature*, 463, 637
- Swain, M. R., Vasisht, G., & Tinetti, G. 2008, *Nature*, 452, 329
- Vidal-Madjar, A., Désert, J.-M., Lecavelier des Etangs, A., et al. 2004, *ApJL*, 604, L69
- Vidal-Madjar, A., Lecavelier des Etangs, A., Désert, J.-M., et al. 2003, *Nature*, 422, 143

# 2

---

## *The signature of orbital motion from the dayside of the planet $\tau$ Boötis b*

---

The giant planet orbiting  $\tau$  Boötis (named  $\tau$  Boötis b) was among the first extrasolar planets to be discovered (Butler et al. 1997). It is one of the brightest exoplanets and one of the nearest to us, with an orbital period of just a few days. Over the course of more than a decade, measurements of its orbital inclination have been announced (Collier Cameron et al. 1999) and refuted (Collier-Cameron et al. 2004), and have hitherto remained elusive (Leigh et al. 2003; Charbonneau et al. 1999; Wiedemann et al. 2001; Lucas et al. 2009; Rodler et al. 2010). Here we report the detection of carbon monoxide absorption in the thermal dayside spectrum of  $\tau$  Boötis b.

At a spectral resolution of 100,000, we trace the change in the radial velocity of the planet over a large range in phase, determining an orbital inclination of  $44.5^\circ \pm 1.5^\circ$  and a mass  $5.95 \pm 0.28$  times that of Jupiter, demonstrating that atmospheric characterization is possible for non-transiting planets. The strong absorption signal points to an atmosphere with a temperature that is decreasing towards higher altitudes, in contrast to the temperature inversion inferred for other highly irradiated planets (Burrows et al. 2008; Fortney et al. 2008). This supports the hypothesis that the absorbing compounds believed to cause such atmospheric inversions are destroyed in  $\tau$  Boötis b by the ultraviolet emission from the active host star (Knutson et al. 2010).

Brogi, Snellen, de Kok et al.  
*Nature*, **486**, 502-504 (2012)

## 2.1 The CRIRES observations

We observed  $\tau$  Boötis for  $3 \times 6$  hours during the nights of April 1, 8, and 14, 2011, with the CRYogenic InfraRed Echelle Spectrograph (CRIRES Kaeufl et al. 2004) at the Nasmyth A focus of the Very Large Telescope UT1, located at the European Southern Observatory on Cerro Paranal, Chile, in conjunction with the Multi-Application Curvature Adaptive Optic system (MACAO Arsenault et al. 2003). We collected 452 spectra over  $\sim 18$  hours of observations, covering most of the planetary orbit from phase  $\varphi = 0.37$  to  $\varphi = 0.63$  (see Figure 2.1). CRIRES utilizes four  $1024 \times 512$  pixel Aladdin III detectors, with a gap of  $\sim 250$  pixels between each chip. Our observations covered a spectral range of 2287.5 nm to 2345.4 nm, targeting the 2-0 R-branch of carbon monoxide, with a  $0.2''$  slit, resulting in a resolution of  $R \sim 100,000$  per frame. Accurate background subtraction requires nodding of the telescope over  $10''$  between frames along the direction of the slit. Due to the uncorrected distortion of the spectrograph, the combination of the spectra at the two nodding positions reduces the resolution to  $R \sim 87,000$ .

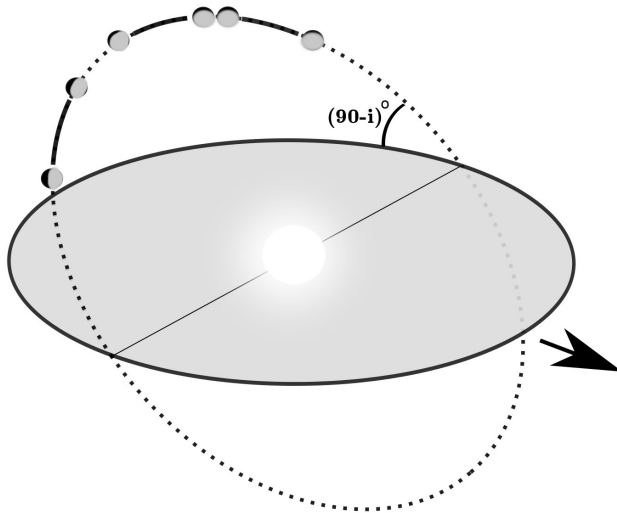


Figure 2.1: Schematic representation of the planetary system  $\tau$  Boötis. We obtained observations of  $\tau$  Boötis during three nights in April 2011, covering a large range in orbital phase, as indicated by those parts of the orbit drawn with a thick line and with planet-images marking the start and end-points. The arrow indicates the direction of the Earth, from which we see the orbit at an inclination  $i$ . The planet orbit and host star are drawn approximately at the correct scale, while the planet-images are enlarged by a factor  $\sim 3$  for clarity.

## 2.2 Data reduction and analysis

### 2.2.1 Initial data reduction

For the data reduction and analysis, we followed a similar procedure as used for the detection of carbon monoxide in the transmission spectrum of HD 209458 b (Snellen et al. 2010). As a first step, we used the ESO CRIRES data pipeline v. 2.1.1 for the dark subtraction, flat-fielding, non-linearity and bad-pixel corrections, and the extraction of the one-dimensional spectra. For the remainder of the analysis, we developed purpose-built algorithms using the Interactive Data Language (IDL). We first corrected for additional hot pixels not picked up by the pipeline, and masked bad regions in the arrays. Next, for each night we chose the spectrum with the highest signal-to-noise ratio as a reference, and aligned all the other spectra to it, by fitting the positions of a set of strong lines in each spectrum and applying a global solution through spline interpolation. In this way, we achieved a typical RMS of  $\sim 0.1$ - $0.2$  pixels per spectrum in the residual line position, with respect to a common wavelength scale. We subsequently determined the wavelength solution by comparing the positions of the telluric lines with those in the HITRAN database (Rothman et al. 2009). The typical uncertainty in the absolute wavelength solution is estimated to be  $0.15$ - $0.20$  km s<sup>-1</sup>. We finally normalized each spectrum to the continuum level of the reference, by fitting a second order polynomial to the flux ratios as function of wavelength, being careful not to sample regions near the telluric absorption features.

### 2.2.2 Removal of telluric line contamination

After the initial data reduction, all the spectra have the same continuum level, while the depths of the telluric lines vary by 15-20%. This is primarily caused by changing airmass, but also due to variations in seeing, instrument resolution, in-slit guiding and adaptive optics corrections, which influence the shape and depth of the absorption lines. For each of the four arrays, the spectral series are handled and visualized as a two-dimensional matrix (Figure 2.2, panel a), in which the horizontal axis is pixel position (representing the wavelength) and the vertical axis is frame number (representing the orbital phase or time). The data are dominated by the absorption lines formed in our own atmosphere, which are fixed in wavelength, and consequently fall on fixed columns in the matrix. Conversely, any signal from the planet will be Doppler-shifted due to the changing radial component of its orbital velocity, and its spectral signature will appear as a tilted trace across the matrix (Snellen et al. 2011). The most critical step in this analysis is the removal of telluric features caused by the Earth's atmosphere, which completely dominate our spectra. This can be achieved without destroying the planetary signature only because the signal from the planet moves significantly in wavelength during our observations, due to its large change in radial velocity along the orbit.

We remove the telluric contamination as follows. The fluxes of each column of the matrix are first fit as a linear function of the geometric airmass at the time of observation, which reduces the variations per column to a few per cent or less (Fig-

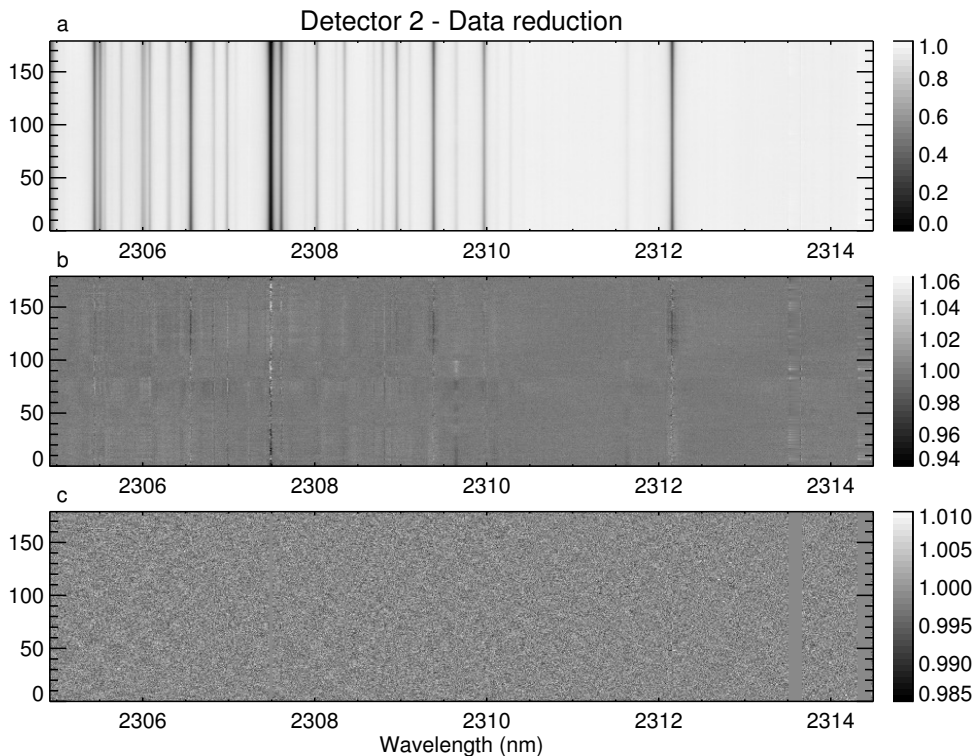


Figure 2.2: An example of our data reduction chain, showing the spectral series from CRIRES detector #2, taken on April 1, 2011. The  $y$ -axis corresponds to time. Data are first aligned and normalized to the same continuum level (a), and subsequently de-trended from the effects of the geometric airmass (b). Finally, correlated and low-order residuals are removed and bad regions in the array are masked (c). See Section 2.2.2 for further details.

ure 2.2, panel b). The remaining time-correlated residuals in the matrix are mostly due to the varying conditions in the Earth's atmosphere throughout the night. We measured the flux of few of the deepest  $\text{H}_2\text{O}$  and  $\text{CH}_4$  lines over time, and used these to correct the rest of the matrix with a column-by-column linear regression. To remove the remaining low-order structure across the matrix, we also applied a high-pass filter to each row. After these steps, each point in the matrix is normalized by its uncertainty (Figure 2.2, panel c) so that noisy parts of the data do not dominate the cross-correlation. By removing the time-dependence of the signal in each column of the matrix, we get rid of the telluric contamination, while the planetary signature is left largely unaffected. Note that, since  $\tau$  Boötis is a F7V star, it does not exhibit significant stellar spectral features in the observed wavelength range.

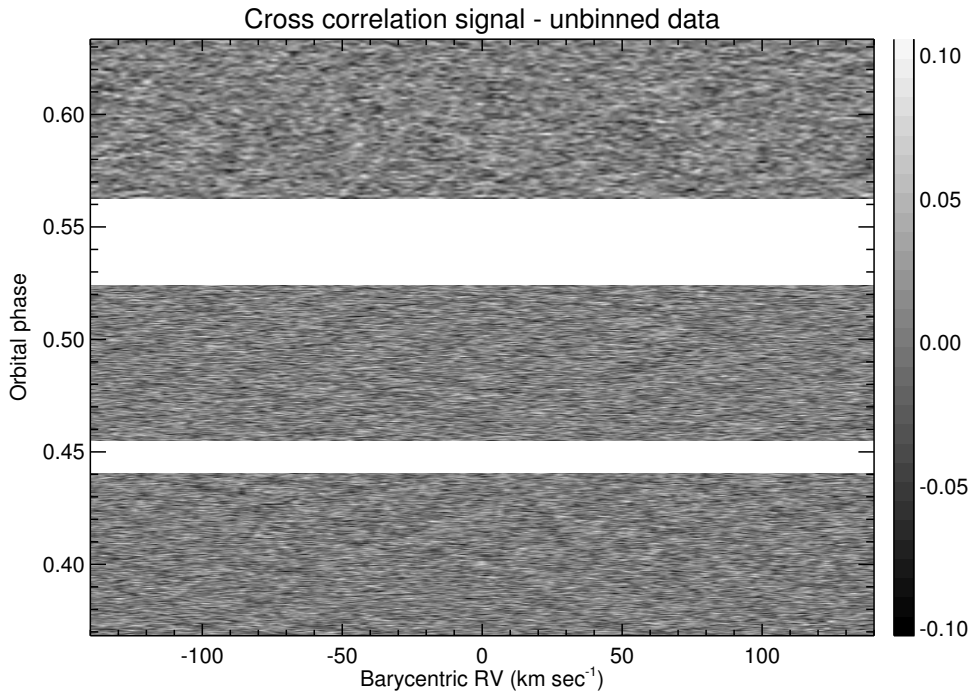


Figure 2.3: Result of the cross-correlation between our data and a template for carbon monoxide, as a function of barycentric radial velocity and planet orbital phase. In this way, the signal from 25-30 molecular lines is combined. The planet signal is not visible, and only becomes evident after binning the data in time (see Figure 2.4). Note that the grey-scale represents the cross-correlation values in arbitrary linear units.

### 2.2.3 Cross correlation and signal extraction

As a result of the data processing described above, the data are no longer sensitive to any broad spectral features. However, they are still sensitive to narrow absorption or emission lines in the planet spectra – in this case tens of CO lines. In order to combine the signal from all the CO lines, we cross-correlate each of the 452 extracted and processed spectra with a CO template, which is shifted in velocity from  $-150 \text{ km s}^{-1}$  to  $+150 \text{ km s}^{-1}$  (in steps of  $1.5 \text{ km s}^{-1}$ ), covering all the possible radial velocities for the planet. The template is obtained from a model spectrum for the atmosphere of  $\tau$  Boötis b (see Section 2.5.1 for details), by fitting the positions and amplitudes of the strongest lines, and redefining them as a series of narrow Gaussian profiles. In this way the broadband component of the model spectrum is discarded, and an optimal sampling for the signal retrieval is achieved. Note that, since the expected carbon monoxide signal in the wavelength regions covered by detectors #1 and #4 is only few per cent of the total, and that in addition these two detectors are significantly affected by an uncorrected odd-even effect<sup>1</sup>, we only include detectors #2 and #3 in

<sup>1</sup><http://www.eso.org/sci/facilities/paranal/instruments/crises/doc/>



our analysis. The result of the cross-correlation across the three nights for detectors #2 and #3 combined is shown by the matrix in Figure 2.3, where the horizontal axis represents radial velocity while the vertical axis is now the orbital phase. When the Doppler-shifted model matches the data, a positive (or negative) value of the cross-correlation will denote emission (or absorption) from the atmosphere of the planet. With about 25-30 CO lines falling in the observed wavelength range, the signal resulting from the cross-correlation is at least a factor of 5 stronger compared to that of a single CO line, but is still buried in the noise at this stage, so that it becomes visible only after binning the data to 0.005 in orbital phase (Figure 2.4).

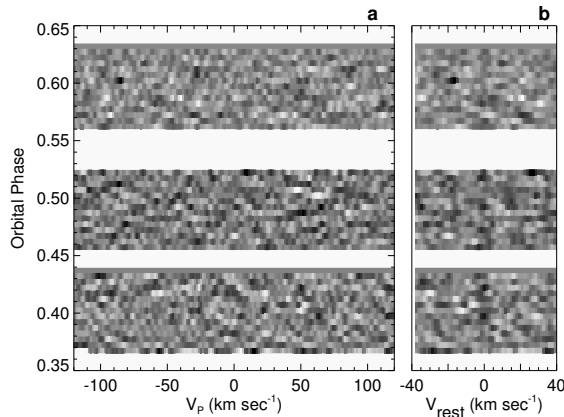


Figure 2.4: The orbital trail of carbon monoxide absorption. On panel *a*, the signature of CO in absorption is visible as a sinusoidal trace around the heliocentric radial velocity of  $\tau$  Boötis from  $+80 \text{ km s}^{-1}$  at phase 0.37 to  $-80 \text{ km s}^{-1}$  at phase 0.63. On panel *b*, the data are shifted to the reference frame of  $\tau$  Boötis b, after subtracting the planet radial velocity computed assuming a circular orbit and a system inclination of  $44.5^\circ$ : here the planet signal is recovered as a vertical trace around  $v_{\text{rest}} = 0 \text{ km s}^{-1}$ . A comparison between the observed trail and artificially-generated data with the same noise properties is shown in Figure 2.5.

From previously measured orbital parameters of  $\tau$  Boötis b (Butler et al. 2006), we determine the phase of the planet at the time of our observation with an uncertainty of  $\pm 0.012$ , while the orbital radial velocity of the planet  $K_p$  is dependent on the unknown system inclination. We therefore assume a large range of values for  $K_p$  and a small global phase shift  $\Delta\varphi$  (see Section 2.3), and determine the expected radial velocity curve for each one of them, incorporating the heliocentric velocity of the observer (due to the orbital and rotational motion of the Earth). Subsequently, we recompute the cross-correlation matrix in the rest frame of the planet by a linear interpolation of each spectrum, and sum along the vertical (time) axis, thus increasing the signal in the cross-correlation function by a factor of  $N^{1/2} \sim 20$ , where  $N$  is the total number of frames. This sum is performed independently for each array of the CRIRES detector, and each observing night. The signals from the individual arrays are then combined with a weighting determined from the CO template,

by summing in quadrature the depths of the model lines falling in the wavelength ranges of the two detectors. Finally, the combined cross-correlation signal of the three nights is summed.

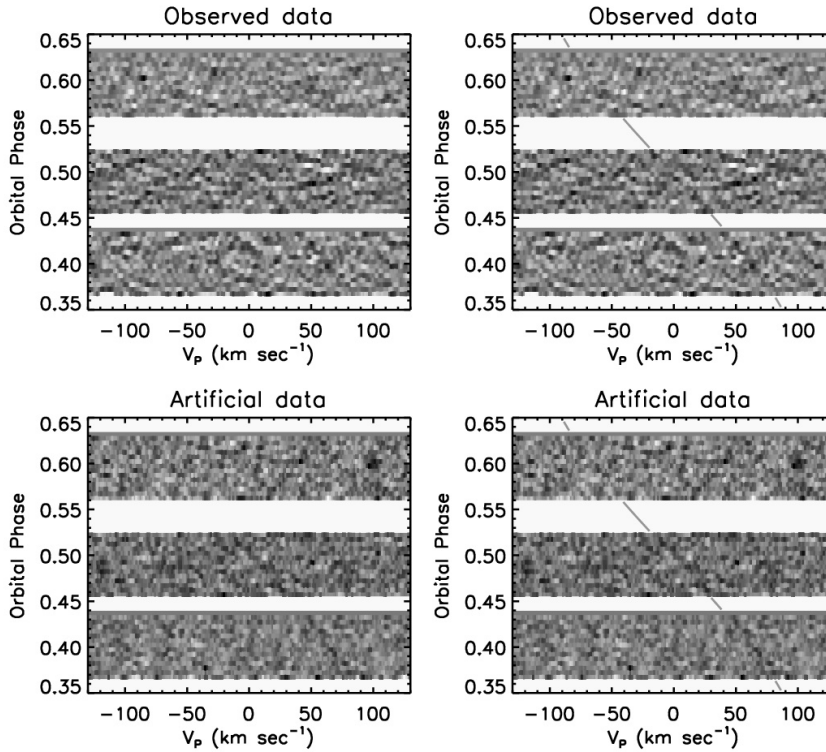


Figure 2.5: Top panels: the observed velocity trail of  $\tau$  Boötis b binned to 0.005 in phase, with and without the guiding lines showing the planet radial velocity (right and left panel respectively). Bottom panels: artificial data consisting of the injected planet velocity trail plus Gaussian noise at the same level as in the observed data. It shows that the planet trail is visible in the observed data at the expected level.

### 2.3 The CO detection and the planet velocity trail

In Figure 2.4 we show the resulting carbon monoxide velocity trail in the cross-correlation data, which is obtained from Figure 2.3 by binning to 0.005 in phase. In Figure 2.5 the same data is shown with and without a grey line guiding the eye (top right and left panels). This is compared with a signal of the same strength, embedded in artificial data with the same noise properties (bottom right and left panels). For a signal at a  $6\sigma$  level, integrated over the entire time series, it is expected that on average at each binned point in phase the velocity trail is visible at a signal-to-noise of  $\sim 1$ . The comparison with the artificial data indicates that the velocity trail is visible at this expected level. Although it is not essential to visually see the

trail at this intermediate stage, it is an extra safety check against a spurious signal originating from strong residuals in one or a few spectra in the dataset.

As explained in Section 2.4, we determine the total signal-to-noise ratio of the CO absorption to be 6.2, by comparing the peak value of the total cross-correlation signal with the standard deviation of the noise (Figure 2.12). Here we explain how we assess the statistical significance of the signal by studying the properties of the cross-correlation noise.

The left panel of Figure 2.6 shows the noise distribution of the cross-correlation time series (i.e., the matrix in Figure 2.3). Overplotted is the best-fit Gaussian distribution with a mean pixel value fixed to zero. The data is well fitted by the Gaussian distribution down to  $\sim 4$  times the standard deviation. There are not enough data points to test Gaussianity beyond this limit. We also compared the cumulative density function of the observed cross-correlation values to that of a normal distribution using a Q-Q probability plot (Wilk & Gnanadesikan 1968), shown in the right panel of Figure 2.6. In such a plot, the quantiles of the observed distribution are plotted against the expected values for a normal distribution, allowing a visual diagnostic of the matching between the two. In our case, the two sets of quantiles are well correlated across the entire range, meaning that the two cumulative density functions agree between  $-4\sigma$  and  $+4\sigma$ . Note that it is not surprising that the distribution of the cross-correlation values is Gaussian, because although the observed spectra may have varying noise patterns as function of wavelength (due to the telluric absorption), each pixel value is first normalized by its uncertainty. In addition, the cross-correlation with a template, consisting of tens of CO lines spanning the entire wavelength range, also strongly scales down any systematic which may deviate from a Gaussian distribution.

After verifying that our data have Gaussian noise properties, we tested the statistical significance of the CO absorption. In Figure 2.7, we show the distribution of pixel values inside and outside the velocity trail of  $\tau$  Boötis b. It suggests that the dispersions in the two distributions are similar, but that the points inside the velocity trail are shifted to lower values. We quantified this using the Welch t-test (Welch 1947), which assumes that both groups of data are sampled from Gaussian populations (like in a standard t-test), but which does not require that they have the same sample variance. The hypothesis that the two distributions are drawn from the same parent distribution is rejected at the  $6\sigma$  confidence level, in line with our earlier estimate.

As an additional test, we removed the planet signal using the best-fitting model and the planet orbital solution (as explained in Section 2.5) and re-injected it at random systemic velocities between  $-45$  and  $+45$  km s $^{-1}$ , and  $K_p$  in the range 100-120 km s $^{-1}$ . In this way we sampled different regions of the spectral series and constructed the distribution of the retrieved signal, shown in Figure 2.8. This results in a mean signal-to-noise of 6.3 with a standard deviation of 1.0, meaning that the measured absorption signal is again consistent with a signal-to-noise of  $\sim 6$ , regardless to where the planet signal is in the data.

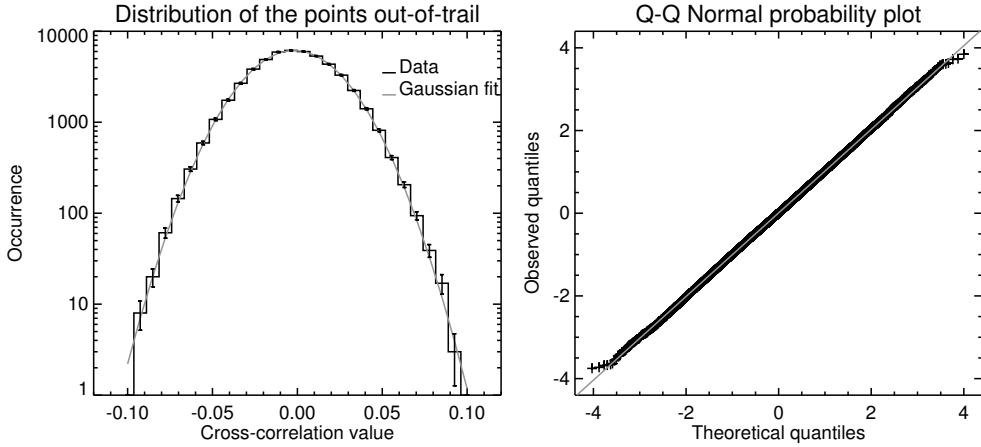


Figure 2.6: Left panel: Distribution of the values of the cross-correlated time series, after excluding the points belonging to the planet trail. A Gaussian curve with zero mean is fitted to the data and overplotted in light grey. The two distributions agree across the entire range that can be tested given the total number of points. The latter corresponds to  $\sim 4$  times the standard deviation of the fitted Gaussian. Right panel: The Q-Q normal probability plot (Wilk & Gnanadesikan 1968), showing the quantiles of the cross-correlation values against the quantiles of a normal distribution. The tight correlation indicates no sign of non-Gaussianity in the data.

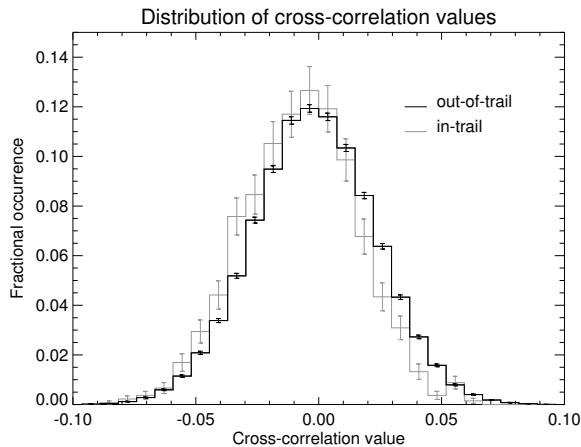


Figure 2.7: Distributions of the values of the cross-correlated time series for points in the planet trail (grey) and out of the trail (black). The error bars denote the square root of the number of data points in each bin ( $1\sigma$ ). The two distributions clearly deviate, with the in-trail distribution shifted to lower pixel values due to the planet signal. A Welch t-test on the data rejects the hypothesis that the two distributions are drawn from the same parent distribution at the  $6\sigma$  level.

Finally, we shifted and co-added the 452 reduced spectra of  $\tau$  Boötis, according to the planet ephemeris and inclination as derived below, to construct a 1D-spectrum. This is the upper spectrum shown in Figure 2.9, for both arrays separately. For comparison, the best-fit model spectrum of the planet atmosphere is shown in the middle, and the same model spectrum with artificial Gaussian noise added at the measured level is provided below. Since the total cross-correlation signal is measured at a  $6\sigma$  level, the strongest lines should be visible at  $\sim 1\sigma$ , but also many features at the same level should not correspond to genuine absorption lines, which is indeed what is seen in both the real and artificial data. Again, this shows that the cross-correlation signal does not originate from one particular part of the spectrum, but from the summed contribution of all absorption lines.

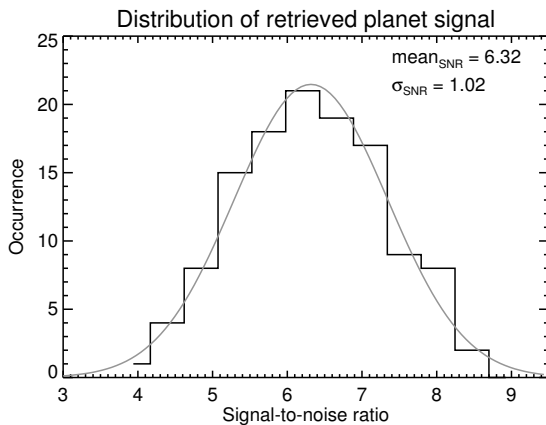


Figure 2.8: Distribution of the retrieved signal-to-noise ratios of artificially injected planet signals with strengths equal to the observed one, but with a range of systemic and planet orbital velocities. The mean (6.3) and the standard deviation (1.0) are those expected for a signal-to-noise ratio of  $\sim 6$ , meaning that  $\sim 66\%$  of the occurrences are between  $5.3\sigma$  and  $7.3\sigma$ , independent from where the planet signal is injected.

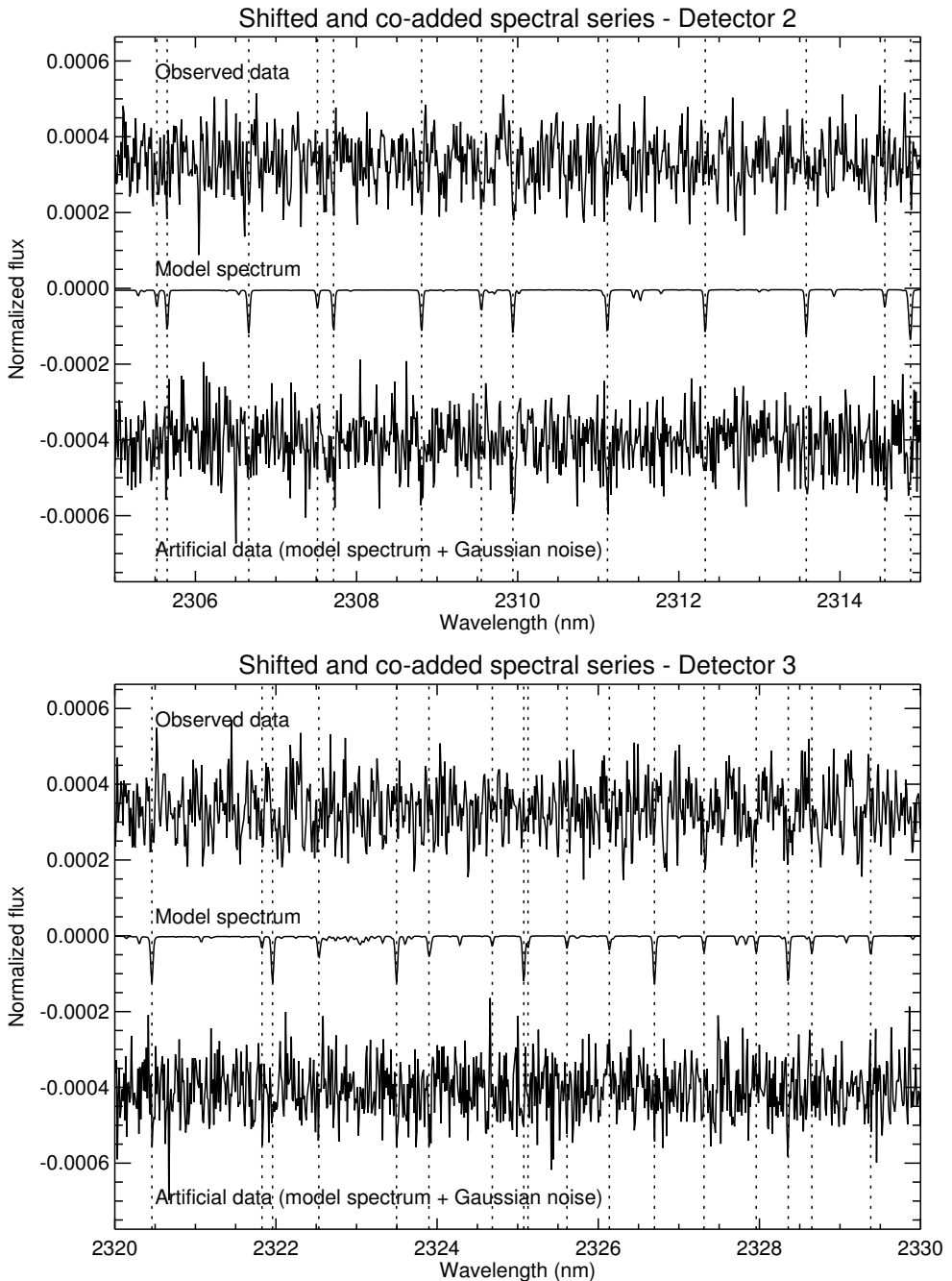


Figure 2.9: One-dimensional spectrum of  $\tau$  Boötis b, constructed by shifting and adding the individual spectra according to the planet orbital solution, with the top and bottom panels showing data from detectors 2 and 3 respectively. In both panels, the model spectrum and model spectrum + Gaussian noise are shown for comparison. The dotted vertical lines indicate the positions of the strongest CO lines.

## 2.4 The planet orbit and mass

The orbital solution for  $\tau$  Boötis b presented in the literature, as derived from the radial velocity variations of the host star (Butler et al. 2006), shows a weak preference for an eccentric solution, with eccentricity  $e = (0.023 \pm 0.015)$  and longitude of periastron  $\omega \approx 188^\circ$ . Adopting this solution, the signature of carbon monoxide from the atmosphere of the planet is retrieved in absorption for a maximum planet radial velocity of  $K_P = (110.2 \pm 3.2) \text{ km s}^{-1}$  and at a  $6.2\sigma$  confidence level. The significance of the planet signal is not affected by the value of  $\Delta\varphi$  across a small range. Therefore, this parameter can be arbitrarily set, as long as it is consistent with the uncertainties in the orbital solution. With a value of  $\Delta\varphi = 0.0068$ , the position of the CO signal matches the systemic velocity of  $\tau$  Boötis,  $V_{\text{sys}} = (-16.4 \pm 0.1) \text{ km s}^{-1}$ , determined by extrapolating a recent literature value (Donati et al. 2008) with our measured linear trend of  $\Delta V_{\text{sys}} = (0.0458 \pm 0.0033) \text{ m s}^{-1} \text{ day}^{-1}$  (see below).

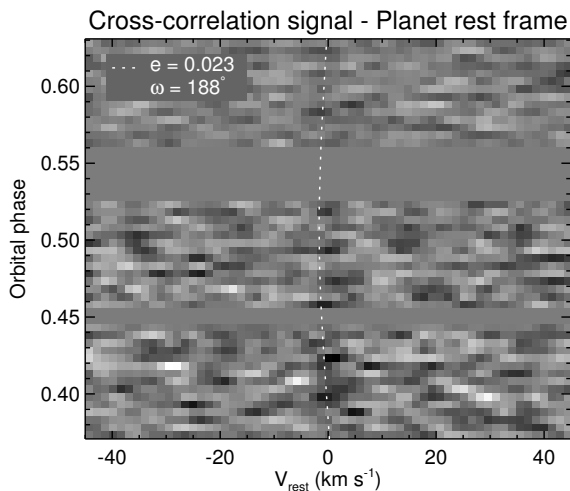


Figure 2.10: Radial velocity trail of  $\tau$  Boötis b, shown in the rest frame of the planet assuming a circular orbit, and binned in phase to increase the signal-to-noise ratio. The eccentric ( $e = 0.023$ ,  $\omega = 188^\circ$ ) solution is shown by the dotted white curve for comparison.

After performing the analysis assuming an elliptical orbit for the planet, we checked whether our data support an eccentric solution. Figure 2.10 shows the observed radial velocity trail of  $\tau$  Boötis b in its rest frame, assuming a circular orbit. The dotted line indicates the expected planet radial velocity for the eccentric solution ( $e = 0.023$ ,  $\omega = 188^\circ$ ). Although not statistically significant, at least by eye it seems that the eccentric solution, which is slightly curved with respect to the circular solution, is a poorer match to the planet radial velocity trail. Therefore, we independently re-analysed all of the available radial velocity data of the host star, obtaining solutions for the time of inferior conjunction ( $T_0$ ), the orbital period ( $P$ ), the stellar radial velocity semi-amplitude ( $K_S$ ) and the residual linear trend on the

data ( $\Delta V_{\text{sys}}$ ), which were found to be all consistent with the literature values (Butler et al. 2006). However, we find that the early data taken between 1987 and 1994, which are significantly noisier than the more recent measurements, are the cause of the slightly eccentric solution.

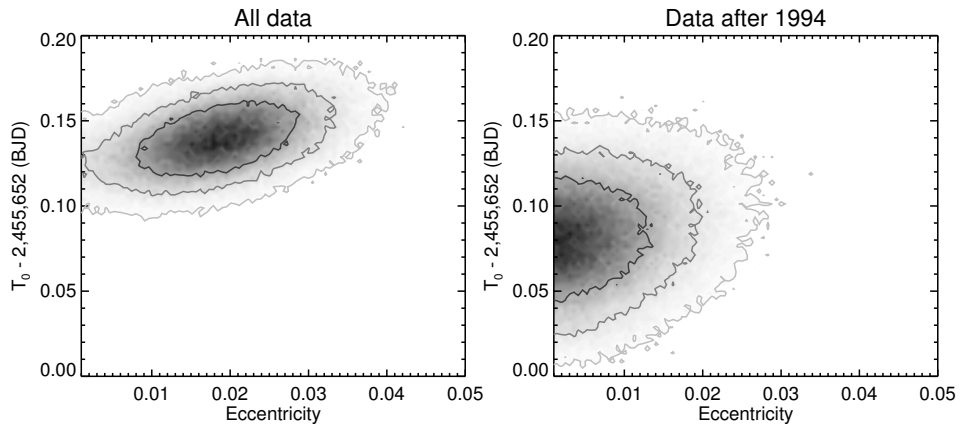


Figure 2.11: The MCMC density distribution of eccentricity ( $e$ ) and time of inferior conjunction ( $T_0$ ), as obtained from our independent fit of the available stellar radial velocity data of  $\tau$  Boötis, with the left panel showing the result when all the measurements are included, and in the right panel only measurements taken after 1994. In the latter case, there is no evidence for a non-circular orbit. The contour levels correspond to the  $1\sigma$ ,  $2\sigma$  and  $3\sigma$  uncertainties in the MCMC distribution.

The left panel of Figure 2.11 shows  $e$  versus  $T_0$  for our MCMC analysis using all the data, showing the weak preference for an eccentric solution and a correlation between  $e$  and  $T_0$ . The right panel shows the same MCMC analysis when excluding the data prior to 1995. No correlation between  $e$  and  $T_0$  is seen and the preference for an eccentric solution is no longer present. Due to the combination of the planet radial velocity data and our re-analysis of the available stellar radial velocity data, we opt to use the circular orbital solution. In this way, a  $6.2\sigma$  absorption signal from carbon monoxide is observed at the maximum planet radial velocity of  $K_P = (110.0 \pm 3.2)$  km s $^{-1}$ , as shown in Figure 2.12, suggesting that the impact of the circular solution on our analysis is negligible. The signal is detected at the systemic velocity of  $\tau$  Boötis for a phase shift of  $\Delta\phi = 0.0091$ , again consistent within the  $1\sigma$  uncertainty. Combining the stellar and planet radial velocity, yields a new set of orbital parameters with  $P = 3.312433(19)$  days,  $T_0 = (2,455,652.108 \pm 0.004)$  HJD,  $K_S = (0.4664 \pm 0.0033)$  km s $^{-1}$ . We determine the star/planet mass ratio to be  $K_P/K_S = (235.8 \pm 7.1)$ , which together with the estimated stellar mass of  $M_S = (1.34 \pm 0.05) M_\odot$  (Takeda et al. 2007) gives a planet mass of  $M_P = (5.95 \pm 0.28) M_{\text{Jup}}$ . Knowing the mass ratio and the orbital period of the planet, we apply Kepler's Third Law to derive a planet orbital velocity of  $V_P = (157.0 \pm 2.6)$  km s $^{-1}$ . The ratio  $K_P/V_P = (0.701 \pm 0.024)$  is the sine of the orbital inclination, which we determine to be  $i = (44.5 \pm 1.5)^\circ$ .



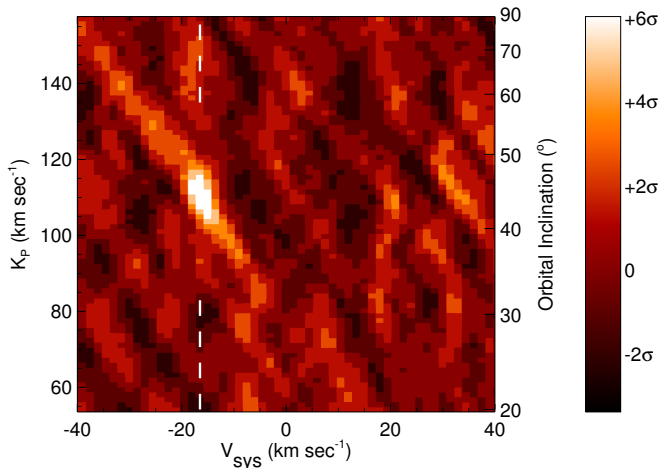


Figure 2.12: color scale plot of the carbon monoxide signal as function of heliocentric velocity on the  $x$ -axis, and the maximum radial velocity of the planet  $K_P$  on the  $y$ -axis. The latter translates to an orbital inclination as indicated by the scale on the right side. Lighter colors indicate CO in absorption. A clear signal at a  $6.2\sigma$  level is visible at the system velocity of  $\tau$  Boötis ( $-16.4 \text{ km s}^{-1}$ ), as indicated by the vertical dashed line, for a maximum planet velocity of  $K_P = (110.0 \pm 3.2) \text{ km s}^{-1}$ . This corresponds to an orbital inclination  $i = (44.5 \pm 1.5)^\circ$  and to a planet mass of  $M_P = (5.95 \pm 0.28) M_{\text{Jup}}$ . The signal is obtained by cross-correlating a template spectrum of CO lines with the CRILES/VLT spectra, which were each shifted in wavelength using the planet’s ephemeris assuming a  $K_P$ . This to compensate for the changing Doppler effect caused by the change in the planet radial velocity over the large range in phase. The significance of the signal and the properties of the cross-correlated noise are discussed in Section 2.3.

## 2.5 The planet atmosphere

### 2.5.1 Atmospheric models

We computed model spectra for the atmosphere of  $\tau$  Boötis b, assuming a mean vertical profile in hydrostatic equilibrium. The profile is defined by two points in the temperature/pressure ( $T/p$ ) space,  $(T_1, p_1)$  and  $(T_2, p_2)$ , for which an isothermal atmosphere is assumed at  $p > p_1$  and  $p < p_2$ , with temperatures  $T_1$  and  $T_2$  respectively. In between these two pressure levels, a constant temperature gradient is assumed as function of the logarithm of the pressure,  $dT/d(\log p)$ , except when an adiabatic lapse rate is assumed. In this last case, the temperature gradient is set to the adiabatic value in each one of the atmospheric layers between  $p_1$  and  $p_2$ . A large range in Volume Mixing Ratios (VMR) for carbon monoxide, water vapor and methane is considered. The observed wavelength region is modeled including 2,225 CO lines, 11,631 H<sub>2</sub>O lines and 15,146 CH<sub>4</sub> lines. Data for CO and H<sub>2</sub>O are obtained from the HITEMP 2010 database (Rothman et al. 2010), while that for CH<sub>4</sub>

come from HITRAN 2008 (Rothman et al. 2009). Although at high temperatures these catalogues could miss some of the weakest lines contributing to the continuum (especially the HITRAN database), all the strong lines which determine the high resolution spectrum are present. Gas opacities are calculated line-by-line using a Voigt profile. In addition, H<sub>2</sub>-H<sub>2</sub> Collision-Induced Absorption (CIA) is also included. Note that the assumed temperature profiles, thought not realistic over the whole extent of a planetary atmosphere, can be effectively used to investigate the parameter space at the pressure levels probed by the molecular absorption lines, and are also easily reproducible by other groups that wish to perform similar analyses.

## 2.5.2 Comparison of model spectra to the data

When we compare the model spectra to the data, two model-dependent observables constrain the CO VMR and the atmospheric  $T/p$  profile: 1) the total strength of the correlated signal, and 2) the relative strength of the signals between arrays #2 and #3. The first observable, the total strength of the correlated signal, is not directly related to the true strength of the molecular lines. This is because the data analysis treats each pixel in the spectrum differently, since each column in the data matrix is normalized by its standard deviation as part of the analysis (see Section 2.2.2). Therefore, for comparing the observed signal strength with that expected for a certain model atmosphere, we inject the reverse model at the observed planet velocity in the data at the beginning of the data-analysis chain, such that the model spectrum is treated in the same way as the data. If the CO lines in the model spectrum are too weak, the observed signal will only be partially removed. If the lines are too strong, they will overcompensate the data, resulting in a positive (emission) cross-correlation signal. In order to scale a particular model to the spectrum, we need to make assumptions about the planet/star radii ratio (which is unknown because  $\tau$  Boötis b is a non-transiting planet), and about the spectrum of the star. We adopt a value of  $R_p = 1.15 R_{\text{Jup}}$  for the planet radius, determined from the mean of the radii of all known transiting planets within the mass range 3-9  $M_{\text{Jup}}$  (Schneider et al. 2011). For the stellar spectrum we use the NextGen model (Hauschildt et al. 1999) with  $T_{\text{eff}} = 6400$  K,  $\log(g) = 4.5$  (CGS units) and  $[\text{Fe}/\text{H}] = 0.5$ , assuming a stellar radius of  $R_S = (1.46 \pm 0.05) R_{\odot}$  (Takeda et al. 2007). Note that uncertainties in the planetary radius, also estimated from the previous sample of transiting exoplanets, affect the absolute level of the signal by  $\sim 35\%$ , and consequently do not change the order of magnitude of our estimates. For the second observable, the relative strengths of the signals in array #2 and #3 are compared to those expected for a model spectrum. This comparison is incorporated in the signal retrieval described in Section 2.2.3, since arrays #2 and #3 are summed with a weight determined from the template model. Therefore, the significance of the detection is already a measure of the second observable.

## 2.6 Discussion

### 2.6.1 Spin-orbit alignment

Spectro-polarimetric observations of  $\tau$  Boötis (Donati et al. 2008; Catala et al. 2007) show that the host star exhibits strong differential rotation, with a period ranging from  $P_{\text{rot}} = 3.0$  to 3.9 days from the equator to the poles. It indicates that the stellar rotation at intermediate latitudes is synchronized with the planet's orbital period ( $P = 3.312$  days). If we assume that the stellar rotation axis is aligned with the normal to the orbital plane of the planet, the projected rotational velocity of the star,  $v \sin(i) \sim 15 \text{ km s}^{-1}$  (Butler et al. 2006), combined with a stellar radius of  $R_S = (1.46 \pm 0.05) R_{\odot}$  (Takeda et al. 2007) and our measurement of  $i$ , indeed corresponds to a stellar rotational period of  $P_{\text{rot}} = 3.3$  days, matching the planet's orbital period. Therefore, in addition to synchronization, it suggests that the orbital plane and the plane of stellar rotation are not significantly misaligned. We would like to point out that a large fraction of the hot Jupiters around hot stars ( $T_{\text{eff}} > 6250 \text{ K}$ ) such as  $\tau$  Boötis, whose orbital alignment can be measured via the Rossiter-McLaughlin effect, exhibit strong misalignments (Winn et al. 2010; Johnson et al. 2011). However, most of the massive planets ( $M_P > 3 M_{\text{Jup}}$ ) are found in more aligned orbits (Hébrard et al. 2010), and  $\tau$  Boötis b does not break this trend.

### 2.6.2 Molecular abundances and lack of an inversion layer

Our observations at high spectral resolution are only sensitive to narrow spectral features, because of the particular data reduction necessary to remove the telluric contamination. Due to the high opacity at the wavelengths of molecular transitions, these narrow features probe the atmosphere at lower pressures than the surrounding continuum. The probed pressures are directly linked to the Volume Mixing Ratio (VMR) of CO, but the depth of the absorption features in the emitted planet spectrum depends on the relative temperatures at the levels of the continuum and CO lines. This means that there is a strong degeneracy between the temperature-pressure profile of the planet atmosphere, and the VMR of CO. We compare our data with a range of models, in order to constrain the CO abundance and the  $T/p$  profile. We obtain a lower limit of the CO VMR by using the adiabatic lapse rate ( $dT/d\log_{10}(p) \sim 1000 \text{ K}$  at these temperatures), which is the maximum temperature gradient of a planet atmosphere before it becomes unstable to convection. An additional uncertainty is that the size of  $\tau$  Boötis b is unknown, because it is a non-transiting planet. Since the average radius of the seventeen transiting hot-Jupiters currently known with  $3 M_{\text{Jup}} < M_P < 9 M_{\text{Jup}}$  is  $1.15 R_{\text{Jup}}$  (Schneider et al. 2011), we assume this value for the planet. When we set the temperature of the atmospheric layer in which the continuum is formed to  $T = 2000 \text{ K}$  (near the expected dayside equilibrium temperature for a planet without energy redistribution to the night-side), and use an adiabatic lapse rate, we require a CO VMR of  $10^{-5}$  to match the observed signal. If we assume a temperature of  $T = 1650 \text{ K}$  for the continuum photospheric layer (near the dayside equilibrium temperature for a planet with perfect redistribution to its night-side), under similar adiabatic conditions, a CO VMR

of  $10^{-4}$  is required. Note that this result is consistent with the metallicity of the host star, corresponding to a CO VMR of  $\sim 10^{-3}$ . We do not detect spectral features from methane or water vapor above a significance of  $2\sigma$ , and we use our atmospheric models to derive upper limits to the relative abundances of these molecules of  $\text{VMR}(\text{CH}_4)/\text{VMR}(\text{CO}) < 1$  and  $\text{VMR}(\text{H}_2\text{O})/\text{VMR}(\text{CO}) < 5$  at a 90% confidence level.

Photometric observations of hot Jupiters with the Spitzer Space Telescope have been interpreted as suggestive of thermal inversions, characterized by molecular features in emission rather than in absorption, of which HD 209458 b is the best-studied example. These inversions are likely fueled by absorption of stellar radiation in a high-altitude absorbing layer. In such a model a thermal inversion is more likely to occur in the most highly irradiated planets, for which indeed some evidence exists (Knutson et al. 2009). The planet  $\tau$  Boötis b is more strongly irradiated than HD 209458 b. However, it is clear that  $\tau$  Boötis b does not exhibit a strong thermal inversion over the pressure range probed by our observations, since we see the CO signal in absorption. Although the exact pressure range probed depends on the CO abundance, the inversion layer invoked to explain the emission spectrum of HD 209458 b encompasses such a wide range in atmospheric pressures that it is evident that  $\tau$  Boötis b does not have a HD 209458 b-type thermal inversion. Interestingly, the host star of  $\tau$  Boötis b exhibits a high level of chromospheric activity, and it has been recently suggested that hot-Jupiters orbiting active stars are less likely to have thermal inversions (Knutson et al. 2010), because the strong UV radiation that accompanies chromospheric activity destroys the absorbing compound at high altitude, which would otherwise be responsible for the thermal inversion.

## 2.7 Conclusions

These observations show that high-resolution spectroscopy from the ground is a valuable tool for a detailed analysis of the temperature structure and molecular content of exoplanet atmospheres. The used technique not only reveals its potential for transmission spectroscopy (Snellen et al. 2010), but also for dayside spectroscopy, meaning that atmospheric characterization is no longer constrained to transiting planets alone. Detection of different molecular bands will further constrain the relative molecular abundances and temperature-pressure profiles. In addition, tracing the signal along the orbit will reveal the planet phase function, which is linked to its global atmospheric circulation. Measuring this for different molecules may reveal changes between a planet's morning and evening spectrum driven by photochemical processes. Furthermore, molecular line profiles, in both dayside and transmission spectra, can potentially show the effects of a planet's rotational velocity, and unveil whether these hot Jupiters are indeed tidally locked.

## Acknowledgments

We thank the ESO support staff of the Paranal Observatory for their help during the observations. Based on observations collected at the European Southern Observatory (186.C-0289). S.A. acknowledges support by a Rubicon fellowship from the Netherlands Organisation for Scientific Research (NWO), and by NSF grant no. 1108595 "Spin-Orbit Alignment in Binary Stars".

## Bibliography

- Arsenault, R., Alonso, J., Bonnet, H., et al. 2003, in Society of Photo-Optical Instrumentation Engineers (SPIE) Conference Series, ed. P. L. Wizinowich & D. Bonaccini, Vol. 4839, 174–185
- Burrows, A., Budaj, J., & Hubeny, I. 2008, *ApJ*, 678, 1436
- Butler, R. P., Marcy, G. W., Williams, E., Hauser, H., & Shirts, P. 1997, *ApJL*, 474, L115
- Butler, R. P., Wright, J. T., Marcy, G. W., et al. 2006, *ApJ*, 646, 505
- Catala, C., Donati, J.-F., Shkolnik, E., Bohlender, D., & Alecian, E. 2007, *MNRAS*, 374, L42
- Charbonneau, D., Noyes, R. W., Korzennik, S. G., et al. 1999, *ApJL*, 522, L145
- Collier-Cameron, A., Horne, K., James, D., Penny, A., & Semel, M. 2004, in IAU Symposium, Vol. 202, Planetary Systems in the Universe, ed. A. Penny, 75
- Collier Cameron, A., Horne, K., Penny, A., & James, D. 1999, *Nature*, 402, 751
- Donati, J.-F., Moutou, C., Farès, R., et al. 2008, *MNRAS*, 385, 1179
- Fortney, J. J., Lodders, K., Marley, M. S., & Freedman, R. S. 2008, *ApJ*, 678, 1419
- Hauschildt, P. H., Allard, F., & Baron, E. 1999, *ApJ*, 512, 377
- Hébrard, G., Désert, J.-M., Díaz, R. F., et al. 2010, *A&A*, 516, A95
- Johnson, J. A., Winn, J. N., Bakos, G. Á., et al. 2011, *ApJ*, 735, 24
- Kaeufl, H.-U., Ballester, P., Biereichel, P., et al. 2004, in Society of Photo-Optical Instrumentation Engineers (SPIE) Conference Series, Vol. 5492, Ground-based Instrumentation for Astronomy, ed. A. F. M. Moorwood & M. Iye, 1218–1227
- Knutson, H. A., Charbonneau, D., Burrows, A., O'Donovan, F. T., & Mandushev, G. 2009, *ApJ*, 691, 866
- Knutson, H. A., Howard, A. W., & Isaacson, H. 2010, *ApJ*, 720, 1569
- Leigh, C., Collier Cameron, A., Horne, K., Penny, A., & James, D. 2003, *MNRAS*, 344, 1271

Lucas, P. W., Hough, J. H., Bailey, J. A., et al. 2009, *MNRAS*, 393, 229

Rodler, F., Kürster, M., & Henning, T. 2010, *A&A*, 514, A23

Rothman, L. S., Gordon, I. E., Barbe, A., et al. 2009, *J. Quant. Spec. Radiat. Transf.*, 110, 533

Rothman, L. S., Gordon, I. E., Barber, R. J., et al. 2010, *J. Quant. Spec. Radiat. Transf.*, 111, 2139

Schneider, J., Dedieu, C., Le Sidaner, P., Savalle, R., & Zolotukhin, I. 2011, *A&A*, 532, A79

Snellen, I., de Kok, R., de Mooij, E., et al. 2011, in *IAU Symposium*, Vol. 276, IAU Symposium, ed. A. Sozzetti, M. G. Lattanzi, & A. P. Boss, 208–211

Snellen, I. A. G., de Kok, R. J., de Mooij, E. J. W., & Albrecht, S. 2010, *Nature*, 465, 1049

Takeda, G., Ford, E. B., Sills, A., et al. 2007, *ApJS*, 168, 297

Welch, B. L. 1947, *Biometrika*, 34, 28

Wiedemann, G., Deming, D., & Bjoraker, G. 2001, *ApJ*, 546, 1068

Wilk, M. B. & Gnanadesikan, R. 1968, *Biometrika*, 55, 1

Winn, J. N., Fabrycky, D., Albrecht, S., & Johnson, J. A. 2010, *ApJL*, 718, L145



# 3

---

## *Detection of molecular absorption in the dayside of exoplanet 51 Pegasi b?*

---

In this paper we present ground-based high-resolution spectroscopy of 51 Pegasi using CRIFRES at the Very Large Telescope. The system was observed for  $3 \times 5$  hours at  $2.3 \mu\text{m}$  at a spectral resolution of  $R = 100,000$ , targeting potential signatures from carbon monoxide, water vapor and methane in the planet's dayside spectrum. In the first  $2 \times 5$  hours of data, we find a combined signal from carbon monoxide and water in absorption at a formal  $5.9\sigma$  confidence level, indicating a non-inverted atmosphere. We derive a planet mass of  $M_{\text{P}} = (0.46 \pm 0.02) M_{\text{Jup}}$  and an orbital inclination  $i$  between  $79.6^\circ$  and  $82.2^\circ$ , with the upper limit set by the non-detection of the planet transit in previous photometric monitoring. However, there is no trace of the signal in the final 5 hours of data. A statistical analysis indicates that the signal from the first two nights is robust, but we find no compelling explanation for its absence in the final night. The latter suffers from stronger noise residuals and greater instrumental instability than the first two nights, but these cannot fully account for the missing signal. It is possible that the integrated dayside emission from 51 Peg b is instead strongly affected by weather. However, more data are required before we can claim any time variability in the planet's atmosphere.

Brogi, Snellen, de Kok et al.  
*ApJ*, 767, 27B (2013)



### 3.1 Introduction

The first discovery of an exoplanet around a main-sequence star, the G-dwarf 51 Pegasi, was announced in 1995 (Mayor & Queloz). The presence of the planet was inferred from the measurement of a periodic Doppler-shift in the stellar lines, which was interpreted as being due to the motion of the star around the center of mass of the star-planet system. Since then, the radial velocity technique has been revolutionary in exoplanet research, resulting in hundreds of discoveries.

51 Pegasi b is unlike any planet in our own Solar System: with a minimum mass of  $\sim 0.5 M_{\text{Jup}}$ , it orbits at only  $\sim 0.05$  AU from the star, well within the orbit of Mercury (0.47 AU). At the time of discovery, the generally accepted theories of planet formation and evolution could not explain the presence and survival of a Jupiter-size planet at such short orbital distance. This resulted in an intense debate on whether the radial velocity signal of 51 Peg really was caused by an unseen planet.

The first concern was that, since the orbital inclination  $i$  was unknown and therefore the measured mass was only a lower limit, 51 Pegasi b could actually be a low-mass star or brown dwarf seen face-on. This hypothesis was rejected because of the low probability of this geometrical configuration ( $2.5 \times 10^{-5}$  for the hydrogen-burning limit of  $0.08 M_{\odot}$ ), the stellar projected rotational velocity (Francois et al. 1996), the absence of an X-ray signal from the system (Pravdo et al. 1996), and eventually the discovery of other 51 Pegasi-like objects (Marcy & Butler 1996; Butler et al. 1997). At the same time, Lin et al. (1996) showed that 51 Pegasi b could have formed much further away from the parent star, and subsequently migrated inward through tidal interaction with the protoplanetary disk. Moreover, Rasio et al. (1996) showed that the timescale for orbital decay via tidal dissipation was possibly longer than the main-sequence lifetime of the star.

Another concern was that stellar radial pulsations or hot spots in the surface could mimic the Doppler signal induced by a short-period giant planet. This hypothesis was also found to be unlikely, because the slow stellar rotation and low chromospheric activity are inconsistent with a high-amplitude signal with a period of a few days. Nevertheless, Gray (1997) performed a bisector analysis on the spectral lines of 51 Peg, concluding that the RV signal was possibly caused by a non-radial, unknown mode of stellar oscillation, rather than by a planet. However, subsequent bisector analyses at higher spectral resolution showed no variations (Hatzes et al. 1997, 1998). In the meantime, adding confidence to the planet hypothesis, the first exoplanets in eccentric orbits were found, making it difficult to explain the RV signals with stellar mechanisms (Marcy & Butler 1996). Eventually, transits of the hot-Jupiter HD 209458 b were observed (Henry et al. 2000; Charbonneau et al. 2000), finally settling the debate on the planetary nature of radial velocity measurements and opening the era of exoplanet characterization.

Although RVs are very successful at detecting planets, they offer little information about the planet itself, whereas transits reveal the planet radius and the system inclination, which, when combined with the radial velocity curve, determine the planet mass, its mean density, and a constraint on the planet's internal struc-

ture. Furthermore, starlight can filter through the planet atmosphere during transit, showing an imprint of its atomic and/or molecular gases. Atmospheric absorption increases the planet effective radius and the transit depth at a given wavelength. Therefore, by measuring the planet radius as a function of wavelength a *transmission spectrum* can be constructed. This technique has led to the identification of atomic sodium (Charbonneau et al. 2002; Snellen et al. 2008; Redfield et al. 2008), potassium (Sing et al. 2011), hydrogen (Vidal-Madjar et al. 2003), carbon and oxygen (Vidal-Madjar et al. 2004), methane and water (Tinetti et al. 2007; Swain et al. 2008; Désert et al. 2009; Sing et al. 2009; Gibson et al. 2011). In addition, the planet is occulted by the star around superior conjunction. Its light is temporarily blocked, allowing its flux to be measured directly by comparison with the out-of-eclipse total system flux. Depending on wavelength, this reveals the planet's thermal emission, possibly modulated by molecular features (Grillmair et al. 2008; Swain et al. 2009), and/or reflected starlight (Mazeh et al. 2012; Mislis & Hodgkin 2012). Finally, continuous flux monitoring of a transiting system can reveal the phase function of the planet (Knutson et al. 2009; Crossfield et al. 2010; Knutson et al. 2012).

Until recently, exoplanet atmospheric characterization was limited to transiting planets, leaving out most of the planets discovered via the RV technique. For the first time, Snellen et al. (2010) demonstrated that ground-based high-resolution spectroscopy and RVs can also be used for exoplanet characterization. They detected the absorption signature of carbon monoxide in the transmission spectrum of HD 209458 b, using the CRIRES spectrograph on the ESO Very Large Telescope. Its spectral resolution of  $R \sim 100,000$  allows the planet signature, which changes in Doppler shift during the observations due to the orbital motion of the planet, to be separated from the stationary telluric and stellar absorption lines. In addition to transmission spectroscopy, this method can be applied to dayside spectroscopy, probing the planet when it is almost fully illuminated, just before and after secondary eclipse. In this case the planet thermal emission, modulated by the atmospheric molecular signature, is directly detected and therefore does not require the planet to transit. This has led to the detection of carbon monoxide absorption in the dayside spectrum of the non-transiting hot Jupiter  $\tau$  Boötis b, also revealing its orbital inclination and planet mass (see Chapter 2, and also Rodler et al. 2012).

In this paper we apply the same method to the non-transiting planet 51 Pegasi b. The remainder of the text is organized as follows: in Section 3.2 we describe our observations and data reduction techniques. The resulting signal is described in Section 3.3, while Section 3.4 extensively discusses the non-detection in one of the three nights of observations. Assuming that the signal in the first two nights is genuine, Section 3.5 presents the derived parameters of 51 Pegasi b and of its atmosphere. Finally, a recap of our main findings and the future perspectives of high-resolution ground-based spectroscopy are presented in Section 3.6.

## 3.2 Observations and Data Reduction

### 3.2.1 Telescope and instruments

High-dispersion infrared spectra of 51 Pegasi ( $K = 3.91$  mag) were taken with the ESO Very Large Telescope (VLT) as part of the Large Program 186.C-0289, aimed at the atmospheric study of the brightest transiting and non-transiting hot Jupiters visible from Cerro Paranal. The system was observed in 2010 on the nights of October 16, 17 and 25 at low airmass, using the CRyogenic Infra-Red Echelle Spectrograph (CRIRES, Kaeufl et al. 2004), mounted at the Nysmith-A focus of the VLT Antu. The spectra are imaged on four  $1024 \times 512$  pixels Aladdin II detectors, separated by small gaps of about 100 pixels. At a resolution of  $R \sim 100,000$ , 904 spectra were collected during a total of  $\sim 16$  hours of observations in the wavelength range  $2.287\text{--}2.345 \mu\text{m}$ , which covers the 2–0 R-branch of carbon monoxide. The Multi-Application Curvature Adaptive Optic system (MACAO, Arsenault et al. 2003) was employed to maximize the throughput of the  $0.2''$  slit. During each night, the target was observed without interruption while nodding along the slit by  $10''$  between consecutive spectra, according to an ABBA pattern, to allow a proper background subtraction. A standard set of calibration frames was taken in the morning after each night of observation.

### 3.2.2 Basic data analysis

The initial data reduction was performed using the CRIRES pipeline 1.11.0<sup>1</sup>. Each set of AB or BA spectra was flat-fielded, corrected for bad-pixels and non-linearity and combined in order to subtract the background. One-dimensional spectra were subsequently extracted with the optimal extraction algorithm (Horne 1986), resulting in 452 spectra. The subsequent data analysis was performed with purpose-built IDL scripts. For each night and each detector, the spectra were handled as a matrix with wavelength (or pixel number) on the  $x$ -axis and time (or phase) on the  $y$ -axis, and treated separately, following the procedure in Snellen et al. (2010) and Chapter 2. This is necessary because each night of observations has different atmospheric and instrumental conditions, and because each detector is read out using a different amplifier, with particular characteristics that need to be modeled independently.

In each spectrum, bad pixels and bad regions were corrected through spline and linear interpolation respectively. The identification of bad pixel/regions was first done by eye on each matrix of data. Residual outliers were removed iteratively during the whole reduction sequence. Subsequently, each spectrum was aligned to a common wavelength scale. The difference between the centroids of the telluric lines and their average value across the entire series was fitted with a linear function in pixel position, and the resulting shift was applied via spline-interpolation. After the alignment the typical scatter in the residual position of the line centroids is on average less than 0.1 pixels. The common wavelength solution was determined by fitting a second-order polynomial to the pixel positions of the lines in the average

---

<sup>1</sup>The pipeline documentation is available at <ftp://ftp.eso.org/pub/dfs/pipelines/crيره/>

spectrum, as function of their corresponding wavelengths listed in the HITRAN database (Rothman et al. 2009). Finally, each spectrum of the series was normalized by its median value.

### 3.2.3 Stellar subtraction

Compared to our previous analysis of HD 209458 and  $\tau$  Boötis, an additional step – the removal of the lines in the stellar spectrum – was required. This is because 51 Peg is a comparatively cooler star with an effective temperature of  $T_{\text{eff}} = (5790 \pm 44)$  K (Fischer & Valenti 2005), and thus several spectral lines, in particular those of CO, are also present in the stellar spectra. Due to the changing barycentric velocity of the observatory during the night ( $\Delta v_{\text{obs}} \sim 0.5\text{-}1.0$  km s<sup>-1</sup>), mainly caused by the rotation of the Earth, the stellar lines shift by 0.3-0.6 pixels in wavelength during our observations. If the stellar spectrum is not subtracted from the data, the procedure used to remove the telluric contamination (see Section 3.2.4) would produce strong residuals at the position of the stellar lines. Since the effective temperature of 51 Pegasi is very similar to that of the Sun, a stellar template was created from a high-resolution solar spectrum (Abrams et al. 1996). The position, amplitude and width of the solar lines were fitted with Gaussian or Lorentzian profiles (where appropriate) and a model spectrum was built from the list of the fitted lines and convolved to the CRIRES resolution. Each frame was then divided through the normalized template spectrum, shifted in wavelength according to the radial velocity of the star 51 Pegasi, and multiplied by a factor of 0.95 in order to match the line depths relative to those of the Sun. The need for a scaling factor is possibly due to differences in spectral type, metallicity and/or rotational velocity between the two stars.

### 3.2.4 Removal of the telluric contamination

The most dominant feature in the spectra is telluric absorption, which has a fixed pattern in wavelength but is variable in depth due to changes in airmass, atmospheric conditions and instrumental response. In order to minimize the telluric signature, the logarithm of the flux in each column of the spectral series was first linearly fitted with geometric airmass and divided out. This greatly reduced the amplitude of the telluric features, although residuals at the 1–5% level were still present at the positions of some of the strongest absorption lines, due to second-order effects. For example, possible changes in the water vapor content during the night will generally not follow airmass. The behavior of the residuals as function of time was therefore measured in a few strong lines and the flux in each column of the matrix was fitted by a linear combination of those measurements, computed via linear regression. In addition, residual large-scale gradients in the matrix were removed by applying a high-pass filter to each spectrum of the series. Finally, each column was divided by the square of its standard deviation, in order to scale down the noisy parts of the spectra according to their signal-to-noise. These would otherwise dominate the cross-correlation analysis performed later.

### 3.2.5 Atmospheric models

In order to be able to combine the spectral lines of 51 Pegasi b via a cross-correlation technique, model spectra of the planet atmosphere were computed assuming an average dayside vertical profile in hydrostatic equilibrium. The atmosphere is assumed to be isothermal for pressures  $p > p_1$  and  $p < p_2$ , at temperatures  $T_1$  and  $T_2$  respectively. In between the two pressure levels, a constant lapse rate  $[d \log(p)]/dT$  is assumed. Inverted and non-inverted temperature-pressure ( $T/p$ ) profiles are modeled by assuming  $T_2 > T_1$  and  $T_2 < T_1$  respectively. Such a vertical structure is the simplest possible for a planet atmosphere, and although it is probably not representative for the entire vertical extent, it is a reasonable assumption in the limited range of temperature and pressure probed by our observations. More importantly, given the degeneracies between vertical profiles and molecular abundances (see Section 3.5.2), a more complex description of the planet atmosphere would be beyond the purposes of this study. Molecular species were assumed to be vertically mixed, with the dominant sources of opacities at 2.3 micron being carbon monoxide, water and possibly methane. Opacities for CO and H<sub>2</sub>O were taken from the HITEMP database (Rothman et al. 2010), while those for CH<sub>4</sub> were taken from HITRAN (Rothman et al. 2009). A grid of models was computed assuming volume mixing ratios (VMRs) between  $-4.5 < \log_{10}(\text{VMR}) < -3.0$  in steps of  $\Delta \log_{10}(\text{VMR}) = 0.5$  for the three molecular species, at pressures of  $p_1 = (1, 0.1, 0.01)$  bar and  $p_2 = (10^{-3}, 10^{-4}, 10^{-5})$  bar, and at three base temperatures of  $T_1 = (1000, 1250, 1500)$  K. These are representative of planet equilibrium temperatures in various cases of energy redistribution.  $T_2$  was fixed to 500 K for non-inverted profiles, and to 1500 K for inverted profiles. All possible combinations of parameters were employed. The radiative transfer in the planet atmosphere was computed in the plane-parallel approximation and typical resulting models are shown in Figure 3.1. As explained in Section 3.5.2, in order to set lower limits on the VMRs of molecules, we also assumed adiabatic lapse rates. In this case,  $p_2$  is set by the altitude at which the atmosphere reaches  $T_2 = 500$  K.

### 3.2.6 Cross correlation

In our observed wavelength range, the expected spectral signature of 51 Pegasi b consists of tens of carbon monoxide lines, plus a possible additional contribution from water vapor and/or methane, with a typical depth per-line of few parts in  $10^5$  with respect to the stellar continuum. Consequently, the individual lines will be in any case deeply buried in the noise, as each spectrum has a signal-to-noise ratio of typically 500. In order to detect the planet signature, the signals from all the lines are combined with a cross-correlation technique (Snellen et al. 2010, and Chapter 2). Instead of directly cross-correlating the atmospheric models with the data, a template spectrum is constructed from the model by subtracting the baseline, clipping out the weakest lines and convolving the result to the CRIRES resolution. This is done because any broad-band signal has been removed by our data reduction technique. In addition, the line profiles in the model should match the instrumental profile in order to maximize the cross-correlation signal. Each spectrum is cross-correlated with the template using a lag-vector corresponding to radial velocities between  $-250$

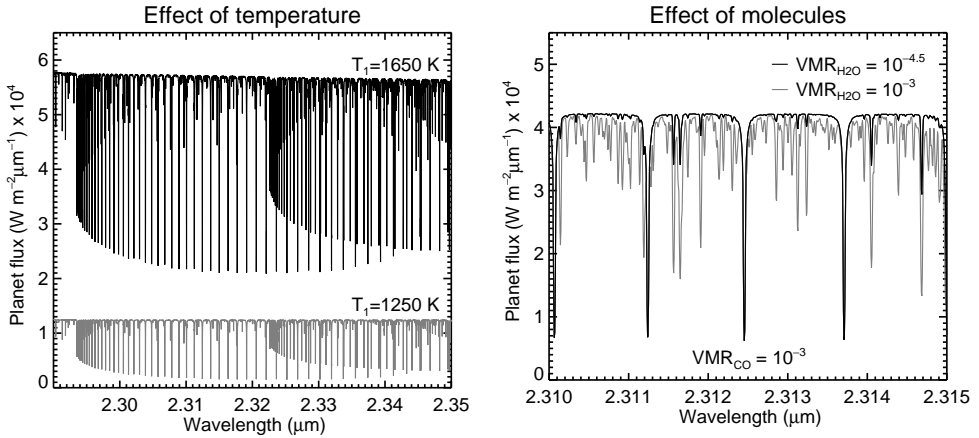


Figure 3.1: Example model spectra for the atmosphere of the planet 51 Pegasi b, showing the effects of different base temperatures  $T_1$  (left panel) and different Volume Mixing Ratios of water and carbon monoxide (right panel). Details about these models are given in Section 3.2.5.

and  $+250 \text{ km s}^{-1}$ , in steps of  $1.5 \text{ km s}^{-1}$ , and the result for each detector and each night is stored in a matrix with  $x$ - and  $y$ -dimension representing radial velocity and frame number (phase) respectively. Subsequently, the matrices of the four detectors are summed with equal weighting, resulting in a single cross-correlation matrix per night of observation. As an exception, detector 4 was discarded from the analysis during the third night (October 25, 2010), as explained in Section 3.4.1. For models with non-inverted (inverted)  $T/p$  profiles, a positive cross-correlation signal indicates absorption (emission) in the planet atmosphere. At this stage the signal-to-noise is insufficient to detect the peak of the cross-correlation function per spectrum so we cannot derive the planet radial velocity curve on a frame-by-frame base. Instead, the cross-correlation signal needs to be combined over time by considering a range of maximum planet radial velocities ( $K_P$ ) corresponding to the possible system inclinations. In all cases we assume a circular orbit. For each value of  $K_P$ , the planet radial velocity curve was computed and utilized to shift each cross-correlation function to the rest frame of the planet, via linear interpolation. Finally, the shifted cross-correlation series was summed over time, resulting in the total cross-correlation signal as function of systemic radial velocity ( $V_{\text{sys}}$ ) and maximum planet radial velocity. If 51 Pegasi b is detected, we should find a peak in the cross-correlation at the known systemic velocity of the system ( $V_{\text{sys}} = -33.25 \text{ km s}^{-1}$ ), for the best matching inclination. Any spectral signature which is not accelerating with respect to the observer will appear at  $K_P = 0$ , including residual telluric and stellar absorption features. More importantly, since the cross-correlation signal is summed in time by assuming a range of inclinations, strong telluric and stellar signals will also show residuals at  $K_P \neq 0$ . These will be shifted in systemic velocity in a non-trivial way, depending on the phase range of the observations (see, e.g., the left column of Figure 3.2). This is why telluric removal and stellar subtraction are

crucial steps of our data analysis.

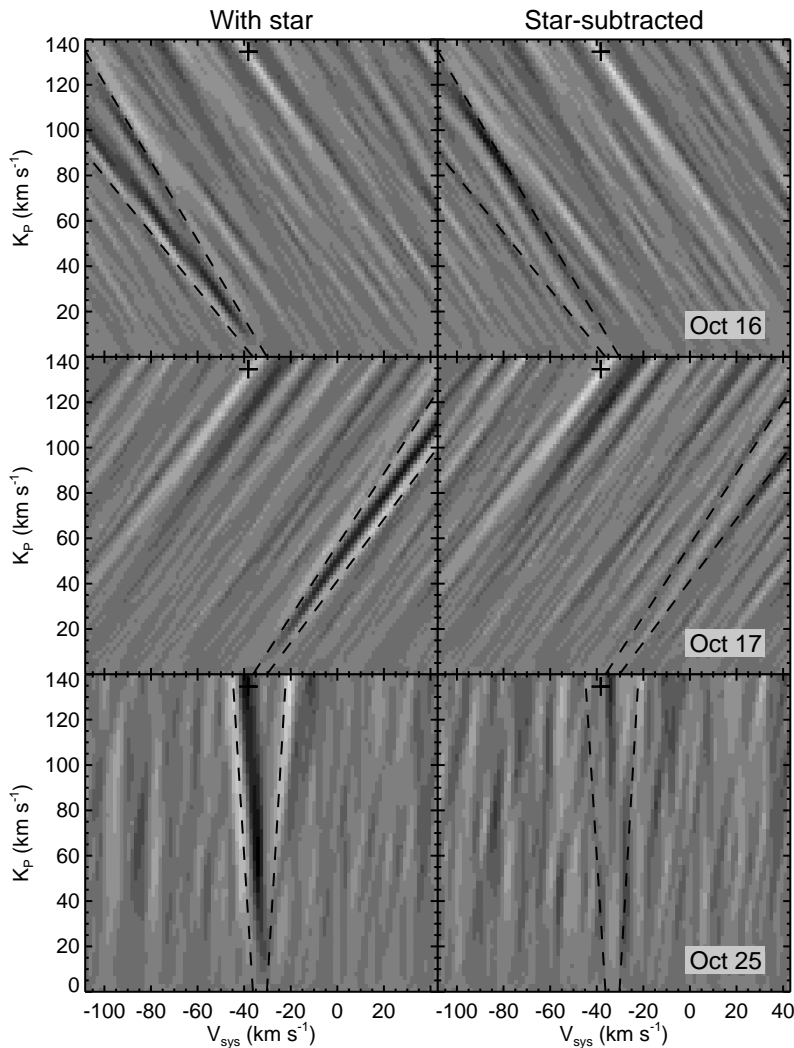


Figure 3.2: *Left column*: Total cross-cross correlation signal for each night of observations, without removing the stellar absorption lines. *Right column*: Same as the left column, but after removing the stellar spectral features. In all panels a linear color scheme running from  $-7\sigma$  (black) to  $+7\sigma$  (white) is adopted. Crosses indicate the planet position measured by combining the nights of October 16 and 17. Black-dashed lines encompass regions of the parameter space significantly affected by stellar residuals. These result in extra cross-correlation noise potentially masking the planet signal in the third night, as discussed in Section 3.4.1.

### 3.3 The cross-correlation signal

The total cross-correlation signal, computed as explained in Section 3.2.6, is shown in Figure 3.2 for each of the three nights of observations, using the planet model spectrum that best matches the data. This is selected from our large grid of models as explained in Section 3.5.2 and corresponds to atmospheric absorption (non-inverted  $T/p$  profile) of carbon monoxide and water, with VMRs of  $10^{-4}$  and  $3 \times 10^{-4}$  respectively. On the nights of October 16 and 17, 2010, candidate signals from 51 Pegasi b are detected at the orbital velocities and systemic velocities listed in Table 3.1. Residuals from stellar lines appear as extra cross-correlation noise in a region of the parameter space approximately enclosed within the black dashed lines in Figure 3.2. The night of October 25 does not show any significant planet signal, and we discuss possible reasons for this in Section 3.4.

Night	$K_P$ ( $\text{km s}^{-1}$ )	$V_{\text{sys}}$ ( $\text{km s}^{-1}$ )	Phase range	Significance
2010-10-16	$122.3^{+15.9}_{-24.8}$	$-25.7^{+15.0}_{-10.3}$	0.36–0.42	$4.5\sigma$
2010-10-17	$134.7^{+13.7}_{-21.3}$	$-33.2^{+9.8}_{-10.3}$	0.60–0.66	$4.7\sigma$
2010-10-25	...	...	0.49–0.54	$<2.5\sigma$
16 + 17	$134.1 \pm 1.8$	$-33.2 \pm 1.5$	n.a.	$5.9\sigma$

Table 3.1: Details of the single-night detections of 51 Pegasi b. The planet orbital velocity, the systemic velocity, the observed range in planet orbital phase and the significance of the detection are given. The last row shows the nights of October 16 and 17 combined. A global phase shift of  $\Delta\varphi = 0.0095$  is applied to the data in order to make the systemic velocity of the night of October 16 and 17 combined to coincide with the systemic velocity of 51 Pegasi.

Figure 3.3 shows the cross-correlation signal of the nights of October 16 and 17 combined. A peak in the total cross-correlation signal is detected at the orbital radial velocity of  $K_P = (134.1 \pm 1.8) \text{ km s}^{-1}$ . Its significance of  $5.9\sigma$  is computed by dividing the peak cross-correlation value by the standard deviation of the noise. This points to a high orbital inclination, as discussed in Section 3.5.1. We discuss how this signal compares to that obtained using models with pure water and pure carbon monoxide in Section 3.5.2. A phase shift of  $\Delta\varphi = 0.0095$  needs to be applied to the orbital parameters of the system given by Butler et al. (2006) in order to match the signal to the known systemic velocity of 51 Pegasi ( $K_{\text{sys}} = -33.25 \text{ km s}^{-1}$ ). This shift is well within the  $1\sigma$  uncertainty range of  $\Delta\varphi = \pm 0.012$  derived from the same orbital solution.



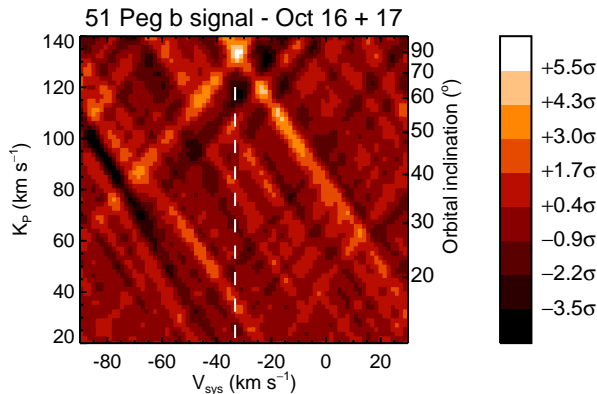


Figure 3.3: Total cross-correlation signal obtained by combining the nights of October 16 and 17 and by applying a global phase shift of  $\Delta\varphi = 0.0095$ . The planet signal is recovered at the systemic velocity of 51 Pegasi ( $V_{\text{sys}} = -33.25 \text{ km s}^{-1}$ , white dashed line) and at a maximum planet radial velocity of  $K_P = (134.1 \pm 1.8) \text{ km s}^{-1}$ . Note that there is an uncertainty in linking the measured  $K_P$  (left vertical axis) to the orbital inclination  $i$  (right vertical axis). This is due to the uncertainties in the stellar mass (see Section 3.5.1).

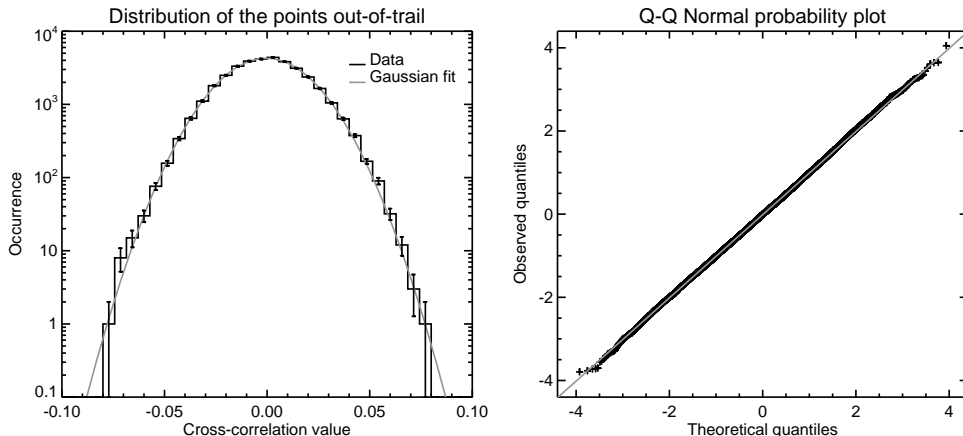


Figure 3.4: *Left panel*: the distribution of the cross-correlation values for the nights of October 16 and 17, 2010 is shown in logarithmic scale, with  $1\sigma$  error bars corresponding to the square root of the bin occurrences. Overplotted in grey is the expected distribution for Gaussian noise. *Right panel*: the quantiles of a Normal distribution are plotted against the quantiles of our measured cross-correlation values (Q-Q plot). In both panels, the observed and theoretical distributions agree across the entire range which can be probed ( $\pm 4\sigma$ ), which is set by the number of cross-correlation points available.

Since one third of the data do not show the planet signal, it is particularly important to robustly assess the statistical significance of the signal in the first two thirds of the data. For this purpose, the properties of the cross-correlation noise were studied by comparing the distribution of the cross-correlation values with that of a Gaussian distribution. This is shown by the left panel of Figure 3.4. In addition, in the right panel the quantiles of the observed distribution are plotted against the quantiles of a Normal distribution (Q-Q plot, Wilk & Gnanadesikan 1968). In both cases, the two distributions agree within  $\sim 4\sigma$ , a limit set by the finite number of points available. It is not surprising that the cross correlation has Gaussian noise properties, as non-Gaussian noise originating from a variable signal-to-noise is avoided by normalizing the data by the square of their standard deviation (see Section 3.2.4). Moreover, systematic noise is also strongly scaled down by the fact that the template spectrum contains tens of well-spaced molecular lines, and therefore the cross-correlation spans large portions of the data.

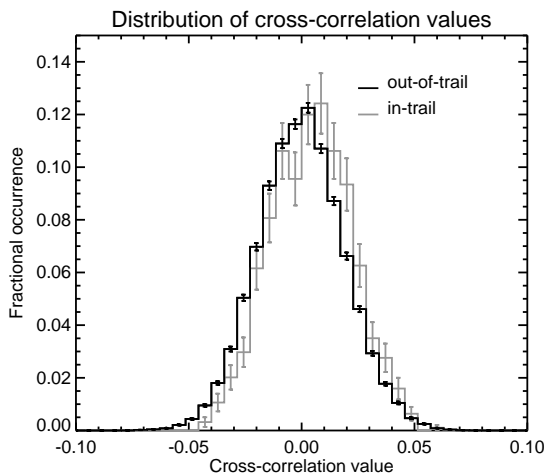


Figure 3.5: Normalized distribution of the cross-correlation values out of the planet trail (black line) compared to the same distribution for the in-trail cross-correlation values. The in-trail distribution is centered to higher values than the out-of-trail distribution at a  $5.4\sigma$  confidence level (see Figure 3.6). The error bars corresponds to the square-root of the bin occurrences.

In Figure 3.5 we compare the distribution of the cross-correlation values inside the planet trail (i.e., those around the planet radial velocity for the derived  $K_P$ ) with that of the points outside the planet trail. The in-trail distribution is shifted towards higher values than the out-of-trail distribution. In order to quantify this, a Welch t-test on the two samples was performed (Welch 1947), with the null hypothesis that they are drawn from the same parent distribution. Based on the results of the test, the null hypothesis is rejected at the  $5.4\sigma$  confidence level, in line with our initial estimate based on pure signal-to-noise calculation. Moreover, Figure 3.6 shows the Welch t-test performed for the full range of  $V_{\text{sys}}$  and  $K_P$  of Figure 3.3. Remarkably, no other region of the parameter space shows significant cross-correlation signal, except

for two slanted lines converging towards the planet signal. This is expected from a real planet signal, because the method used for summing the cross-correlation functions in time naturally produces signals fading away from the planet position. For this reason two or more observations taken at different phases are much more effective in constraining the planet parameters than a single observation.

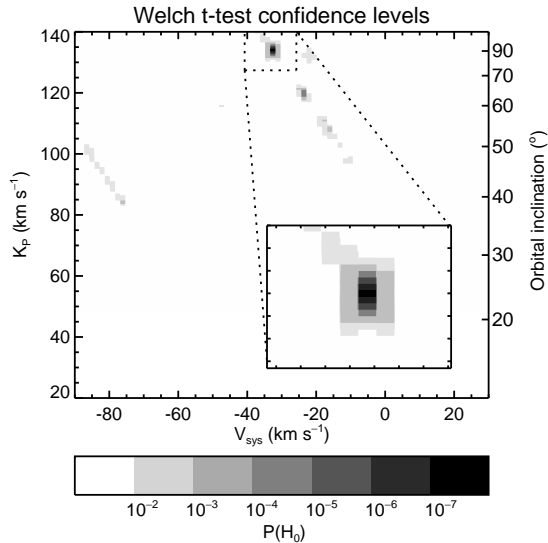


Figure 3.6: Results of a generalized t-test on the null hypothesis that the in- and out-of-trail cross-correlation values are drawn from the same parent distribution. This test is performed for the same combination of systemic velocities and planet orbital velocities as in Figure 3.3. It indicates that the null hypothesis  $H_0$  can be rejected at the  $5.4\sigma$  confidence level for the planet signal. Note that there is an uncertainty in linking the measured  $K_p$  (left vertical axis) to the orbital inclination  $i$  (right vertical axis). This is due to the uncertainties in the stellar mass (see Section 3.5.1).

### 3.4 The non-detection on the third night

As explained in Section 3.3, the third night of observations does not show any sign of an absorption signal from the dayside of 51 Pegasi b. This is a concern because of the statistical robustness of the detection during the first two nights (see Section 3.3), which makes it unlikely that time-correlated noise could mimic the planet signal. Therefore, it is important to investigate the possible causes of this discrepancy. We discuss below i) possible issues with the instrument, data and/or data analysis for the third night, and ii) possible astrophysical causes.

#### 3.4.1 Issues with instrument, data and data analysis

The night of October 25 experienced a relatively good seeing and a longer coherence time than the other two nights of observations, resulting in better performances

of the MACAO system and therefore in a higher signal to noise compared to the first two nights (by 5-15% per spectrum). However, the stability of the CRIFES spectrograph was significantly worse, causing the spectra to drift by  $\sim 1.5$  pixels in the dispersion direction, whereas during the other two nights these shifts were only 0.2-0.5 pixels. The cause of this drift is likely associated with thermal instabilities of the cryogenic system. The temperature of the pre-optics system, grating stabilizer and grating itself changed by about 1.5 K during the 5 hours of observation on October 25, whereas during the other two nights it was stable at the  $< 0.05$  K level. This drift in temperature is indeed correlated with the drift in spectral position on the detector. Since the spectra need to be aligned to a common reference frame (see Section 3.2.2), the wavelength drift has a negative impact on the quality of the data. We were forced to discard detector 4 from the analysis of the third night, because it suffers from gain variations between neighboring columns (the so-called odd-even effect). While with sub-pixel shifts this is not a significant problem (spectral features roughly fall on the same pixel), for shifts of one pixel or more the odd-even effect introduces strong time-correlated noise in the data of up to several percent. In addition, general flat-field inaccuracies are affecting the data more significantly.

Despite the instrumental issues during the third night, the expected significance of the detection in the third night is  $\sim 3.8\sigma$ , based on the measured signal-to-noise, the total number of spectra, and the fraction of data lost because of the exclusion of detector 4. This means that, taking into account statistical fluctuations, there is a probability of 20%, 10% and 5% to measure a signal less than  $2.5\sigma$ ,  $2.2\sigma$  and  $1.8\sigma$  respectively during the third night.

Another potential issue concerns residual stellar spectral features. As explained in Section 3.2.6 and shown in Figure 3.2, even after subtracting a model stellar spectrum from the data, residual cross-correlation noise is seen. This is likely due to changes in the spectral response profile during the night and to inaccuracies in the alignment. This is particularly an issue during the third night, because the system was observed at phase  $\varphi \sim 0.5$ , when the planet spectral lines overlap with those of the star (i.e., planet and star have almost the same radial velocity). In contrast, during the nights of October 16 and 17 the planet and the star have a different radial velocity, causing this residual cross-correlation noise to be located in regions of the parameter space far away from the planet position, and therefore not significantly influencing the measured signal. The effects of the stellar residuals are shown in Figure 3.2, before and after the subtraction of the stellar spectrum (left and right columns respectively). During the third night of observations the expected planet signal falls clearly on top of the residual stellar cross-correlation (bottom-left panel). After the subtraction of the stellar spectrum residual signal is still visible (bottom-right panel). It is possible to filter out these stellar residuals by masking 5-7 pixels in the cross-correlation matrix, around the stellar radial velocity. In this way another  $\sim 40\%$  of the planet signal is removed, as estimated by injecting a model spectrum in the data at  $3\times$  the nominal level and at the previously determined  $K_p$  and re-running the data analysis. Even after masking, no significant planet signal is detected. Although stellar residuals cannot explain the complete absence of a planet signal, they certainly damp part of it. This is another important factor that

differentiates the third night from the other two.

### 3.4.2 Astrophysical causes

We also explored which possible astrophysical effects may cause the non-detection during the third night. First of all, the planet is observed around phase  $\varphi = 0.5$ , meaning that if it was a transiting system the planet would be eclipsed by the star, potentially explaining why no signal was detected. However, photometric monitoring of the 51 Peg system shows that the planet does not transit (Henry et al. 1997; Walker et al. 2006). For a system to exhibit secondary eclipses without transits, we calculated that the orbital eccentricity needs to be at least 0.13 for a stellar radius of  $R_S = (1.237 \pm 0.047)R_\odot$  (van Belle & von Braun 2009) and a planet radius of  $1 R_{\text{Jup}}$ . This is clearly excluded by the radial velocity data of the star (Butler et al. 2006).

Small deviations from the best-fit orbital solution to these radial velocity data can influence the radial velocity and timing of the expected planet signal, which could cause the non-detection during the third night. All the orbital solutions available in the literature agree over the fact that the radial velocity data of 51 Pegasi are equally well fit by a circular orbit as by a slightly eccentric orbit (e.g., Mayor & Queloz 1995; Butler et al. 2006). Butler et al. (2006) obtained a best solution with  $e = (0.013 \pm 0.012)$  and  $\omega \approx 58^\circ$ . We tested various eccentric solutions in order to retrieve the total cross-correlation signal and at the same time the  $\chi^2$  of the orbital solution to the stellar radial velocity data (Butler et al. 2006). Assuming an eccentricity of  $e = 0.025$  and  $\omega \sim 180^\circ$ , which is more than  $2\sigma$  away from the best-fit solution of Butler et al. (2006), it was only possible to shift the signals of the third night by  $\sim 4 \text{ km s}^{-1}$ , whereas the closest cross-correlation peak in the third night can be aligned to the other two only if shifted by about  $10 \text{ km s}^{-1}$ . This means it is not possible to explain the non-detection by assuming an eccentric solution.

When discussing astrophysical causes, there is also the possibility that the signal from the atmosphere itself is changing, either due to an orientation effect or due to temporal changes. At orbital phase  $\varphi = 0.5$ , the orientation of the planet is almost precisely on the sub-stellar point, meaning that a relatively hotter atmosphere is observed. Although the presence of an inversion layer in hot-Jupiter atmospheres is still not well understood, stellar irradiation is thought to play a role (Fortney et al. 2008). However stellar activity (Knutson et al. 2010) and different elemental abundances (Madhusudhan 2012) have also been suggested as possible causes. Higher temperatures mean that some molecular species remain in the gas phase, and are capable of absorbing radiation high up in the atmosphere, causing a thermal inversion and spectral features in emission. If the atmosphere of 51 Pegasi b would be partially inverted around the sub-stellar point, this may cancel out part of the signal. In the limit of a nearly isothermal dayside atmosphere, as it seems to be the case for some hot Jupiters (see, e.g., Crossfield et al. 2012), no signal would be detected. However, the illumination of the visible planet disk changes only by  $\sim 20\%$  during these observations, requiring a large temperature gradient as function of longitude and a significant contribution in absorption from the night-side, which is in contrast with an inefficient heat transport required by the presence of a much hotter sub-stellar

spot. Moreover, such a large gradient would also show up in our data as a phase-dependent cross-correlation signal, something that we do not detect. This leaves only the possibility of temporal variations, the details and timescale of which are largely unknown even for hot Jupiters. Although theoretical studies predict weather to be important in hot Jupiters and brown-dwarfs (Showman & Kaspi 2013), with only three nights of observations we are reluctant to attribute the absence of the planet signal to exoplanetary weather.

### 3.5 Characterization of exoplanet 51 Peg b

In the previous sections we showed that our observations resulted in an apparent planet signal in the first two nights, but no detection in the third night. We have discussed several potential causes of the non-detection, including genuine astrophysical causes, none of which was robustly proven to be associated to the lack of signal. Even though we cannot confidentially exclude the possibility that the signal observed in the first two nights is due to a yet unknown and unfortunate instrumental effect, in this Section we assume that the signal is genuine and proceed with the characterization of 51 Pegasi b.

#### 3.5.1 Planet mass and system inclination

The known radial velocity amplitude of the host star,  $K_S = (55.94 \pm 0.69) \text{ m s}^{-1}$  (Butler et al. 2006), combined with our measured planet radial velocity amplitude of  $K_P = (134.1 \pm 1.8) \text{ km s}^{-1}$ , gives a star/planet mass ratio of

$$\frac{M_S}{M_P} \equiv \frac{K_P}{K_S} = (2397 \pm 44). \quad (3.1)$$

With a stellar mass of  $M_S = (1.05 \pm 0.04) M_\odot$ , as determined by Takeda et al. (2007), it translates into a planet mass of  $M_P = (0.46 \pm 0.02) M_{\text{Jup}}$ . The orbital velocity of the planet can be computed through Kepler's Third Law, and it is equal to  $V_P = (133.7 \pm 1.8) \text{ km s}^{-1}$ . The sine of the inclination is

$$\sin i = \frac{K_P}{V_P} = (1.003 \pm 0.019), \quad (3.2)$$

and implies  $1\sigma$ ,  $2\sigma$  and  $3\sigma$  lower limits on the orbital inclination of  $79.6^\circ$ ,  $74.7^\circ$  and  $71.0^\circ$  respectively. Observations conducted with the MOST satellite show that the planet is not transiting (Walker et al. 2006). Using the planet and stellar radii given in Section 3.4.2, this sets an upper limit on the system inclination of  $i_{\text{max}} = (82.2 \pm 0.3)^\circ$ .

#### 3.5.2 The atmosphere of 51 Pegasi b

The first information which is derived from the cross-correlation signal is that the atmosphere of 51 Pegasi b is not thermally inverted in the pressure range probed by these observations. This is because significant planet signal is only observed when

Molecule	$K_P$ (km s <sup>-1</sup> )	$V_{\text{sys}}$ (km s <sup>-1</sup> )	Significance
H <sub>2</sub> O	136.9±2.8	-34.9 <sup>+1.4</sup> <sub>-2.0</sub>	4.1σ
CO	134.2±1.8	-33.2±1.5	5.7σ

Table 3.2: Details of the cross-correlation signals obtained by employing models with pure water or pure carbon monoxide, for the nights of October 16 and 17 combined. The planet orbital velocity, the systemic velocity and the significance of the detection are given.

using models with non-inverted  $T/p$  profiles (atmospheric absorption). In addition, significant cross-correlation signals are obtained not only from models with pure carbon monoxide, but also from models with pure water, at a  $\leq 5.7\sigma$  and  $\leq 4.1\sigma$  level respectively. Details of these single-molecule detections are given in Table 3.2. No significant signal from a pure methane model is observed. This suggests that, while in our previous study of  $\tau$  Boötis b the cross-correlation signal was entirely due to CO, here there is a significant contribution from H<sub>2</sub>O lines. In order to take this into account, another set of atmospheric models was computed by including both molecules, for the same range of pressure and temperature as in Section 3.2.5. Further information about the structure of the planet atmosphere can be derived by comparing the cross-correlation signal retrieved by using this additional grid of atmospheric templates. Note that, since the data analysis removes broad-band spectral features such as the slope of the planet continuum and the wings of broad lines, the cross correlation is only sensitive to narrow spectral features, such as the flux ratio between the planet continuum and the core of the molecular lines. The comparison between models and data can be done in the following two ways. Firstly, different model spectra, exhibiting varying line ratios, can be cross-correlated with the data. The model spectrum that matches the data the best will show the the strongest signal. Secondly, the amplitude of the model spectrum can be compared with the dayside spectrum of 51 Pegasi b by subtracting the model spectrum from the data early on in the analysis chain, before telluric removal. This comparison must account for the dilution by the starlight, which results in the following normalized planet spectrum:

$$F_{\text{norm}}(\lambda) = \frac{F_{\text{model}}(\lambda)}{F_{\text{star}}(\lambda)} \left( \frac{R_P}{R_S} \right)^2, \quad (3.3)$$

where  $F_{\text{model}}$  is the model spectrum,  $F_{\text{star}}$  the stellar spectrum (for which we use the NextGen low-resolution model for a 51 Peg-like star with  $T_{\text{eff}} = 5800$  K,  $\log g = 4.5$ , and solar metallicity) and  $R_P$  and  $R_S$  the planet and stellar radii respectively. This scaled model is reversed and injected in the data at the measured planet position, before telluric removal. As a result, the cross-correlation signal will be cancelled out when the model matches the data. However, the fact that the planet is not transiting the host star adds significant uncertainty to this second test, because  $R_P$  is unknown. Where not specified, 51 Pegasi b is assumed to have the size of Jupiter.

It is important to realize a degeneracy exists between molecular abundances and atmospheric lapse rate. The higher the VMR, the higher the altitude at which a molecule absorbs. This generally translates to a larger temperature difference between the layer in which the planet continuum is formed and the altitude at which a molecule absorbs in the core of a line. However, this difference is also related to the atmospheric lapse rate, i.e., the rate at which the temperature changes with pressure. Since the temperature difference determines the contrast between the continuum and the core of the lines, the observed strength of the high-resolution planet signal is affected by this degeneracy, which cannot be solved with a single observation in a limited wavelength range. In this work, the lapse rate was fixed to the adiabatic value (i.e., the maximum allowed in a planet atmosphere, corresponding to the onset of convection), and the base temperature  $T_1$  was chosen to be roughly the planet equilibrium temperature (see Section 3.2.5 for details). This results in a maximum planet signal for a given molecular abundance and therefore sets lower limits in the molecular VMRs.

Among the large set of models generated as explained in Section 3.2.5, we selected the best-matching dayside model spectrum of 51 Pegasi b by requiring, at the same time, the highest signal-to-noise of the total cross-correlation signal and zero residual cross-correlation signal after subtracting the model spectrum from the data. A range of  $\pm 1\sigma$  around these two values is explored in order to allow noise fluctuations. This criterium resulted in a model with  $T_1 = 1250$  K,  $p_2 = 10^{-4}$ ,  $\text{VMR}(\text{CO}) = 10^{-4}$ ,  $\text{VMR}(\text{H}_2\text{O}) = 3 \times 10^{-4}$ , meaning that approximately 40% of the signal is due to  $\text{H}_2\text{O}$  molecular lines. This is not surprising, given the relatively lower equilibrium temperature of 51 Pegasi b as compared to  $\tau$  Boötis. Below 1500 K carbon monoxide starts to be significantly less abundant than water for solar C/O ratios (Madhusudhan 2012). Our detection of water together with carbon monoxide, assuming the signal is genuine, is therefore in line with a relatively cooler hot Jupiter. Note however that the relative abundance of water with respect to carbon monoxide is only weakly constrained by these observations, with the  $1\sigma$  range being  $0.05 < \text{VMR}(\text{H}_2\text{O})/\text{VMR}(\text{CO}) < 140$ .

Note that, intuitively, atmospheric models containing both water and carbon monoxide would produce a cross-correlation signal which is roughly the quadrature sum of that obtained from models with pure  $\text{H}_2\text{O}$  or pure CO, combining in this case to  $\sim 7\sigma$  of significance. However, in practice, this does not happen, because the two cross-correlation signals cannot be considered to be independent. Superposition of CO and water lines (see, e.g., Figure 3.1, right panel), and a mismatch between the real planet spectrum and the model templates used, can cause the total signal to deviate from a simple quadrature sum of that of the individual gases. Also, the combined model redistributes the noise content of the data. This means that the combined signal may deviate from the value expected from the individual gases with a probability distribution having a standard deviation of  $1\sigma$ .



### 3.6 Conclusions and future prospects

By observing the orbital motion of 51 Pegasi b directly using high-resolution spectra, we have likely been able to disentangle the spectral fingerprints of the planet's atmosphere from telluric and stellar contamination, and reveal significant absorption from carbon monoxide and water vapor in its dayside hemisphere using the first two nights of observations. This was achieved by studying the cross-correlation of the data with a model planet atmosphere. In this way the radial velocity of the planet is measured directly, allowing us to determine the planet/star mass ratio and the system inclination. This analysis suggests that 51 Pegasi b has a mass of  $M_p = (0.46 \pm 0.02) M_{\text{Jup}}$  and an orbital inclination between  $79.6^\circ$  and  $82.2^\circ$ , with the upper limit set by the non-detection of transits in photometric monitoring of the host star. By comparing the cross-correlation signal obtained with a range of atmospheric models, we estimate minimum molecular abundances of  $\text{VMR}(\text{CO}) = 10^{-4}$  and  $\text{VMR}(\text{H}_2\text{O}) = 3 \times 10^{-4}$ .

However, the absence of the signal in the third night of observations is puzzling. Based on a conservative signal-to-noise estimate, there is a 20% probability of observing a signal less than  $2.5\sigma$  in the third night purely due to noise fluctuations. Moreover, the stability of the CRIFES spectrograph was much worse during the third night of observations, so that possible flat-field inaccuracies affect a larger portion of the data. Furthermore, residual cross-correlation signals from stellar features are present at the expected planet position in the night of October 25. We also investigated possible astrophysical causes of the lack of signal, i.e., the presence of a mild temperature inversion at the sub-stellar point or atmospheric variability due to weather. However, none of the possible instrumental and astrophysical causes can be confidentially linked to the non-detection, meaning that future observations of 51 Pegasi will be essential in confirming the signal presented in this work.

Ground-based high-resolution spectroscopy in the near-infrared is a powerful tool for investigating hot Jupiter atmospheres. While the interpretation of low-resolution studies during transits or secondary eclipses is often controversial, due to the fact that molecular features superimpose across the same wavelength range, this technique unambiguously identifies molecular signatures thanks to the use of a cross-correlation technique with template models. Moreover, it delivers the planet radial velocities directly and does not require – when applied to dayside spectroscopy – a planet to transit. The only requirement is that the planet must move significantly in radial velocity (by  $10\text{--}20 \text{ km s}^{-1}$ ) during the observations.

The main limitations of this technique are currently the degeneracy between atmospheric structure and molecular abundances, and the need for very bright targets. The former can in principle be solved by observing at multiple wavelengths and by detecting the signatures of different molecular species, a goal that is within the reach of our current methods and of the available instrumentation. The latter will certainly benefit from the next-generation of telescopes with mirrors of 30 m or more, and possibly from spectrographs capable of observing larger wavelength ranges at once, as the total cross-correlation signal is approximately proportional to the square root of the number of strong molecular lines observed.

Future developments of high-resolution spectroscopy may involve the study of the shape of the cross-correlation peak during transit, capable of revealing atmospheric rotation and global circulation patterns. Furthermore, by accumulating enough signal-to-noise, it will be possible to study the phase curve of these hot Jupiter and trace changes in the molecular abundances and in the atmospheric chemical processes between their morning and evening sides. Eventually, by employing a 39-m class telescope such as the E-ELT, it may be possible to detect oxygen in the atmosphere of an Earth-like planet orbiting in the habitable zone of an M-dwarf star (Snellen et al. 2013). This would be a considerable jump forward towards the detection of biosignatures in Earth analogs.

## Acknowledgments

We are thankful to the ESO staff of Paranal Observatory for their support during the observations. This work is based on data collected at the European Southern Observatory (186.C-0289). I. S. acknowledges support by VICI grant no. 639.043.107 from the Netherlands Organisation for Scientific Research (NWO). S.A. acknowledges support by a Rubicon fellowship from the NWO, and by NSF grant no. 1108595.

## Bibliography

- Abrams, M. C., Goldman, A., Gunson, M. R., Rinsland, C. P., & Zander, R. 1996, *Appl. Opt.*, 35, 2747
- Arsenault, R., Alonso, J., Bonnet, H., et al. 2003, in Society of Photo-Optical Instrumentation Engineers (SPIE) Conference Series, Vol. 4839, Adaptive Optical System Technologies II, ed. P. L. Wizinowich & D. Bonaccini, 174–185
- Brogi, M., Snellen, I. A. G., de Kok, R. J., et al. 2012, *Nature*, 486, 502
- Butler, R. P., Marcy, G. W., Williams, E., Hauser, H., & Shirts, P. 1997, *ApJL*, 474, L115
- Butler, R. P., Wright, J. T., Marcy, G. W., et al. 2006, *ApJ*, 646, 505
- Charbonneau, D., Brown, T. M., Latham, D. W., & Mayor, M. 2000, *ApJL*, 529, L45
- Charbonneau, D., Brown, T. M., Noyes, R. W., & Gilliland, R. L. 2002, *ApJ*, 568, 377
- Crossfield, I. J. M., Barman, T., Hansen, B. M. S., Tanaka, I., & Kodama, T. 2012, *ApJ*, 760, 140
- Crossfield, I. J. M., Hansen, B. M. S., Harrington, J., et al. 2010, *ApJ*, 723, 1436
- Désert, J.-M., Lecavelier des Etangs, A., Hébrard, G., et al. 2009, *ApJ*, 699, 478
- Fischer, D. A. & Valenti, J. 2005, *ApJ*, 622, 1102
- Fortney, J. J., Lodders, K., Marley, M. S., & Freedman, R. S. 2008, *ApJ*, 678, 1419

- Francois, P., Spite, M., Gillet, D., Gonzalez, J.-F., & Spite, F. 1996, *A&A*, 310, L13
- Gibson, N. P., Pont, F., & Aigrain, S. 2011, *MNRAS*, 411, 2199
- Gray, D. F. 1997, *Nature*, 385, 795
- Grillmair, C. J., Burrows, A., Charbonneau, D., et al. 2008, *Nature*, 456, 767
- Hatzes, A. P., Cochran, W. D., & Bakker, E. J. 1998, *ApJ*, 508, 380
- Hatzes, A. P., Cochran, W. D., & Johns-Krull, C. M. 1997, *ApJ*, 478, 374
- Henry, G. W., Baliunas, S. L., Donahue, R. A., Soon, W. H., & Saar, S. H. 1997, *ApJ*, 474, 503
- Henry, G. W., Marcy, G. W., Butler, R. P., & Vogt, S. S. 2000, *ApJL*, 529, L41
- Horne, K. 1986, *PASP*, 98, 609
- Kaeufl, H.-U., Ballester, P., Biereichel, P., et al. 2004, in Society of Photo-Optical Instrumentation Engineers (SPIE) Conference Series, Vol. 5492, Ground-based Instrumentation for Astronomy, ed. A. F. M. Moorwood & M. Iye, 1218–1227
- Knutson, H. A., Charbonneau, D., Cowan, N. B., et al. 2009, *ApJ*, 703, 769
- Knutson, H. A., Howard, A. W., & Isaacson, H. 2010, *ApJ*, 720, 1569
- Knutson, H. A., Lewis, N., Fortney, J. J., et al. 2012, *ApJ*, 754, 22
- Lin, D. N. C., Bodenheimer, P., & Richardson, D. C. 1996, *Nature*, 380, 606
- Madhusudhan, N. 2012, *ApJ*, 758, 36
- Marcy, G. W. & Butler, R. P. 1996, *ApJL*, 464, L147
- Mayor, M. & Queloz, D. 1995, *Nature*, 378, 355
- Mazeh, T., Nachmani, G., Sokol, G., Faigler, S., & Zucker, S. 2012, *A&A*, 541, A56
- Mislis, D. & Hodgkin, S. 2012, *MNRAS*, 422, 1512
- Pravdo, S. H., Angelini, L., Drake, S. A., Stern, R. A., & White, N. E. 1996, *New Astronomy*, 1, 171
- Rasio, F. A., Tout, C. A., Lubow, S. H., & Livio, M. 1996, *ApJ*, 470, 1187
- Redfield, S., Endl, M., Cochran, W. D., & Koesterke, L. 2008, *ApJL*, 673, L87
- Rodler, F., Lopez-Morales, M., & Ribas, I. 2012, *ApJL*, 753, L25
- Rothman, L. S., Gordon, I. E., Barbe, A., et al. 2009, *J. Quant. Spec. Radiat. Transf.*, 110, 533
- Rothman, L. S., Gordon, I. E., Barber, R. J., et al. 2010, *J. Quant. Spec. Radiat. Transf.*, 111, 2139

- Showman, A. P. & Kaspi, Y. 2013, *ApJ*, 776, 85
- Sing, D. K., Désert, J.-M., Fortney, J. J., et al. 2011, *A&A*, 527, A73
- Sing, D. K., Désert, J.-M., Lecavelier Des Etangs, A., et al. 2009, *A&A*, 505, 891
- Snellen, I. A. G., Albrecht, S., de Mooij, E. J. W., & Le Poole, R. S. 2008, *A&A*, 487, 357
- Snellen, I. A. G., de Kok, R. J., de Mooij, E. J. W., & Albrecht, S. 2010, *Nature*, 465, 1049
- Snellen, I. A. G., de Kok, R. J., le Poole, R., Brogi, M., & Birkby, J. 2013, *ApJ*, 764, 182
- Swain, M. R., Tinetti, G., Vasisht, G., et al. 2009, *ApJ*, 704, 1616
- Swain, M. R., Vasisht, G., & Tinetti, G. 2008, *Nature*, 452, 329
- Takeda, G., Ford, E. B., Sills, A., et al. 2007, *ApJS*, 168, 297
- Tinetti, G., Vidal-Madjar, A., Liang, M.-C., et al. 2007, *Nature*, 448, 169
- van Belle, G. T. & von Braun, K. 2009, *ApJ*, 694, 1085
- Vidal-Madjar, A., Désert, J.-M., Lecavelier des Etangs, A., et al. 2004, *ApJL*, 604, L69
- Vidal-Madjar, A., Lecavelier des Etangs, A., Désert, J.-M., et al. 2003, *Nature*, 422, 143
- Walker, G. A. H., Matthews, J. M., Kuschnig, R., et al. 2006, in Tenth Anniversary of 51 Peg-b: Status of and prospects for hot Jupiter studies, ed. L. Arnold, F. Bouchy, & C. Moutou, 267–273
- Welch, B. L. 1947, *Biometrika*, 34, 28
- Wilk, M. B. & Gnanadesikan, R. 1968, *Biometrika*, 55, 1



# 4

---

## *Carbon monoxide and water vapor in the atmosphere of the non-transiting planet HD 179949 b*

---

In recent years, ground-based high-resolution spectroscopy has become a powerful tool for investigating exoplanet atmospheres. It allows the robust identification of molecular species, and it can be applied to both transiting and non-transiting planets. Radial-velocity measurements of the star HD 179949 indicate the presence of a giant planet companion in a close-in orbit. The system is bright enough to be an ideal target for near-infrared, high-resolution spectroscopy.

Here we present the analysis of spectra of the system at  $2.3 \mu\text{m}$ , obtained at a resolving power of  $R \sim 100,000$ , during three nights of observations with CRIRES at the VLT. We targeted the system while the exoplanet was near superior conjunction, aiming to detect the planet's thermal spectrum and the radial component of its orbital velocity. Unlike the telluric signal, the planet signal is subject to a changing Doppler shift during the observations. This is due to the changing radial component of the planet orbital velocity, which is on the order of  $100\text{-}150 \text{ km s}^{-1}$  for these hot Jupiters. We can therefore effectively remove the telluric absorption while preserving the planet signal, which is then extracted from the data by cross correlation with a range of model spectra for the planet atmosphere.

We detect molecular absorption from carbon monoxide and water vapor with a combined signal-to-noise ratio (S/N) of 6.3, at a projected planet orbital velocity of  $K_P = (142.8 \pm 3.4) \text{ km s}^{-1}$ , which translates into a planet mass of  $M_P = (0.98 \pm 0.04)$  Jupiter masses, and an orbital inclination of  $i = (67.7 \pm 4.3)$  degrees, using the known stellar radial velocity and stellar mass. The detection of absorption features rather than emission means that, despite being highly irradiated, HD 179949 b does not have an atmospheric temperature inversion in the probed range of pressures and temperatures. Since the host star is active ( $R'_{HK} > -4.9$ ), this is in line with the hypothesis that stellar activity damps the onset of thermal inversion layers owing to UV flux photo-dissociating high-altitude, optical absorbers. Finally, our analysis favors an oxygen-rich atmosphere for HD 179949 b, although a carbon-rich planet cannot be statistically ruled out based on these data alone.

Brogi, de Kok, Birkby et al.  
*A&A*, in press (arXiv:1404.3769)

## 4.1 Introduction

Since the mid-1990s, the exoplanet community started to use ground-based high-resolution spectroscopy as a tool for measuring signals from exoplanet atmospheres (Collier Cameron et al. 1999; Charbonneau et al. 1999). It allows molecular bands to be resolved into the individual lines, offering a robust way of identifying molecular species by line matching. It is also able to detect the planet orbital motion in the form of a Doppler-shifted spectrum. This means that the radial velocity of the planet can be directly measured, and the star + planet system can be treated in the same way as a spectroscopic binary. While the first observations of exoplanets at high spectral resolution were focused on detecting reflected starlight from hot Jupiters, it soon became clear that most of these planets might have a very low albedo (Marley et al. 1999; Sudarsky et al. 2000). Similar searches for thermal emission (e.g., Wiedemann et al. 2001) were conducted at a lower resolving power ( $R < 50,000$ ) and were limited by the narrow spectral range of near-infrared instruments. Therefore, these early studies were only able to put upper limits on the detected planet signal, and ground-based high-resolution spectroscopy remained unsuccessful at detecting signatures from an exoplanet atmosphere for more than a decade.

Transiting planets can be observed at high spectral resolution while crossing the stellar disk (transmission spectroscopy), when a small fraction of the stellar light filters through their atmospheres, but also just before and after secondary eclipse, when the illuminated planet hemisphere is facing the observer (dayside spectroscopy). In the latter case, the thermal emission from the planet is targeted directly, meaning that dayside spectroscopy can be applied to non-transiting planets as well. Direct imaging and direct spectroscopy, which have recently achieved great successes in characterizing non-transiting planets (Konopacky et al. 2013), can so far be applied only to young, self-luminous planets on large orbits. High-resolution spectroscopy offers a complementary method capable of studying the atmospheres of close-in, evolved non-transiting planets, and of determining their orbital inclination and true mass.

By using the CRYogenic Infra-Red Echelle Spectrograph (CRIRES, Kaeufl et al. 2004) at the ESO Very Large Telescope (VLT) facility, the first molecular detections at high spectral resolution were obtained in recent years. By observing a transit of HD 209458 b at  $2.3 \mu\text{m}$ , the radial velocity of the exoplanet was measured (Snellen et al. 2010) by tracing the Doppler-shifted carbon monoxide absorption while the planet was transiting the host star. Dayside spectroscopy in the same wavelength range revealed molecular absorption in the atmosphere of the non-transiting exoplanet  $\tau$  Boötis b (Chapter 2), whose mass and orbital inclination were also determined by means of the measured planet radial velocity. Molecular absorption from CO and possibly water was also observed in the dayside spectrum of 51 Peg b (Chapter 3), although one of the three nights of observations does not show a signal and therefore more data are required in order to confirm the detection. Finally, the dayside spectrum of the transiting planet HD 189733 b was also investigated at high-resolution around  $2.3 \mu\text{m}$  and  $3.2 \mu\text{m}$ . The *K*-band data revealed CO absorption (de Kok et al. 2013b), and the *L*-band data resulted in the detection of water vapor ab-

sorption (Birkby et al. 2013), which demonstrates the robustness of high-resolution spectroscopy even when searching for more complicated molecules such as H<sub>2</sub>O and in spectral regions heavily contaminated by telluric absorption.

Here we present high-resolution dayside spectroscopy of the non-transiting planet HD 179949 b. We detect carbon monoxide and water vapor in the planet atmosphere, and solve for the planet mass and system inclination. The system HD 179949 is introduced in Section 4.2, while Section 4.3 presents our observations and data analysis. Section 4.4 explains how we cross correlate the data with model spectra in order to extract the planet signal, and the results of our analysis are presented in Section 4.5. The interpretation of our measurements and future prospects of high-resolution spectroscopy for exoplanet studies are presented in Section 4.6.

## 4.2 The system HD 179949

The F8 main-sequence star HD 179949 has a mass of  $M_S = (1.181^{+0.039}_{-0.026}) M_\odot$  and a radius of  $R_S = (1.23 \pm 0.04) R_\odot$  (Takeda et al. 2007). Interestingly for these observations, the relatively high stellar effective temperature ( $T_{\text{eff}} = 6168 \pm 44$  K) and projected rotational velocity ( $7.0 \pm 0.5$  km s<sup>-1</sup>) ensure that no significant stellar absorption is present in the wavelength range covered by our data, especially CO absorption which would cause a spurious cross-correlation signal when the planet and the star have a similar radial velocity (i.e., around superior conjunction, see Chapter 3). This star is known to host a planet from radial velocity (RV) measurements (Tinney et al. 2001). Since no transit of HD 179949 b is detected, only a lower limit of  $m \sin(i) = (0.902 \pm 0.033)$  Jupiter masses ( $M_{\text{Jup}}$ ) can be put on its mass, with the orbital inclination  $i$  being unknown.

Cowan et al. (2007) observed the phase curve of HD 179949 with Spitzer/IRAC at 3.6  $\mu\text{m}$  and 8.0  $\mu\text{m}$ . At the longer wavelength, they detected peak-to-peak flux variations of  $(1.41 \pm 0.33) \times 10^{-3}$  relative to the average flux from the system, in phase with the orbit of the planet. By assuming a planet radius ( $1 < R_P < 1.2$ )  $R_{\text{Jup}}$  and a Bond albedo close to zero, they were able to constrain the recirculation efficiency as a function of system inclination, and concluded that less than 21% of the incident energy must recirculate to the night side.

Barnes et al. (2008) used CRIRES at a resolution of  $R \sim 50,000$  to observe HD 179949 during two nights in the wavelength range 2.1215-2.1740  $\mu\text{m}$ . After testing for molecular absorption and emission, they were able to rule out absorption features at a 99 per cent confidence level, for a planet-to-star contrast ratio of  $\sim 3 \times 10^{-4}$ . As shown in Section 4.5, our observations detect molecular absorption from HD 179949 b, at a contrast ratio of roughly  $\sim 10^{-4}$ , which is consistent with the above upper limit.

Finally, the star HD 179949 is an active star, with an activity index of  $\log(R'_{HK}) = -4.720 \pm 0.031$  (Watson et al. 2010, supplementary information). By analyzing the variability of the Ca II K and H emission, Shkolnik et al. (2003) reported evidence for the activity of HD 179949 being in phase with the planet orbit. Fares et al. (2012) studied the large-scale magnetic field of the star, and concluded that the chromospheric activity of HD 179949 is mainly modulated by the stellar rotation,



although there is some evidence of an additional modulation with the period of the planet companion. A similar conclusion was obtained by Gurdemir et al. (2012). These results support the hypothesis that HD 179949 experiences planet-induced emission enhancement, as a result of the strong planet-star interaction.

## 4.3 Observations and data analysis

### 4.3.1 Telescope, instrument and observations

As part of the Large Program 186.C-0289, 1000 spectra of the system HD 179979 ( $K = 4.94$  mag) were obtained during the nights of July 17, 2011 (398 spectra, 5.5 hours of observations excluding overheads), July 19, 2011 (388 spectra, 5.4 hours of observations), and August 22, 2011 (214 spectra, 3 hours of observations) with CRIRES, mounted at the Nasmyth-A focus of the VLT UT1 (Antu).

The spectrograph was set to cover the wavelength range 2287.5-2345.4 nm, roughly centered on the 2-0 R-branch of carbon monoxide. Possible additional molecular absorption from water vapor and methane is also present at these wavelengths. We employed CRIRES at the maximum resolution ( $R = 100,000$ ) by using the  $0.2''$  slit. In order to maximize the instrument throughput, the Multi Application Curvature Adaptive Optic system (MACAO, Arsenault et al. 2003) was used. The observations were conducted by nodding the spectrograph  $10''$  along the slit, in a standard ABBA pattern, for accurate background subtraction.

Unlike our previous observations of  $\tau$  Boötis and 51 Pegasi (Chapters 2, and 3), the observing conditions differed considerably between the three nights for this target. Firstly, HD 179949 reaches almost the zenith from Paranal, and therefore the airmass varies considerably during a full night of observations, which causes spectra taken at airmass  $\sim 2$  to have approximately half the signal-to-noise ratio (S/N) of those taken around culmination. Moreover, during the night of August 22, 2011, HD 179979 was observed as a backup target because of pointing restrictions, resulting in non-optimal performances of the MACAO AO system, and a poorer S/N. Finally, during the first two nights, the spectra were taken in groups of 100. At the end of each group, the target was reacquired by the telescope and the AO loop temporarily opened, resulting in small temporal gaps, reducing the S/N of the first spectra of each series, and impacting the overall instrument stability. These factors are taken into account during the data analysis, as explained in Section 4.3.3.

### 4.3.2 Extraction of the one-dimensional spectra

The basic calibration and extraction of the spectra was performed with the CRIRES pipeline version 2.1.3, in combination with both the GUI Gasgano (version 2.4.0) and the command-line interface esorex (version 3.9.0).

Standard calibration frames taken in the morning after each night of observations were used for flat-fielding and dark correction. The non-linearity measurements available in the CRIRES archive were also used. Each frame was dark-subtracted, non-linearity corrected and flat-fielded. Then each couple of nodded observations

(AB or BA) was combined into a single spectrum for accurate background subtraction. The one-dimensional spectra were finally obtained by optimal extraction (Horne 1986), resulting in 199, 194, and 107 spectra respectively for the three nights of observations. These were subsequently analyzed independently in order to account for different atmospheric and instrumental conditions.

### 4.3.3 Bad-pixel correction and wavelength calibration

Subsequently, the data analysis was performed by employing our own dedicated set of routines written in IDL. As for all our previous high-resolution data, the spectra of each night of observation and each of the CRIRES detectors were organized in matrices with pixel number (wavelength) on the horizontal axis and frame number (time) on the vertical axis, of which an example is shown in Figure 4.1 (panel *a*).

The first step in the data analysis is to correct for detector cosmetics and cosmic rays. Isolated bad-pixels were replaced by their spline-interpolated value across the neighboring pixels in the spectral direction. Small groups of adjacent bad-pixels (typically 2 or 3 pixels along the spectral axis) were corrected by linear interpolation. Finally, there was not enough information to correct for large groups (> 5) of adjacent bad pixels. These were therefore masked in all the subsequent steps of the data analysis.

The spectra were then aligned to a common wavelength scale, which is in this case that of the spectrum with the highest S/N in the series. We fit the centroid position of the deepest lines in each spectrum, and computed the difference with those of the reference spectrum. This difference was then fit with a linear function of pixel number and the fit was utilized to shift each spectrum via spline interpolation. Under standard observing conditions, the wavelength solution of CRIRES spectra varies smoothly as a function of time, and the resulting shifts are generally at the sub-pixel level. For these observations, because of the re-acquisition of the telescope (see Section 4.3.1 above), the wavelength solution shifted by 1-2 pixels each time a series of 100 spectra was taken. We therefore discarded 2 pixels at the edges of the spectra, in order to prevent artifacts from the interpolation to the new pixel scale. Finally, with the spectra all aligned to the same reference, we determined the common wavelength solution by comparing the pixel position of the telluric lines in the spectra with their vacuum wavelengths listed in the HITRAN database. We find that a quadratic fit (pixel, wavelength) is sufficient for this purpose, with typical residuals having r.m.s. of 0.15-0.30 km s<sup>-1</sup> (or 0.1-0.2 pixels). The wavelength solution was determined for each of the CRIRES detectors separately. We note that detectors 1 and 4 suffer from the so-called “odd-even effect”, which is a non-linear change in gain between odd and even columns along the spectral direction<sup>1</sup>. Although for most of the science uses of CRIRES this effect can be corrected by using non-linearity measurements, in our case detector 4 still showed residual odd-even signatures after being calibrated. These residuals would significantly affect the data when the spectra are aligned to the same reference frame, especially for these observations

<sup>1</sup>[http://www.eso.org/sci/facilities/paranal/instruments/crises/doc/VLT-MAN-ESO-14500-3486\\_v93.pdf](http://www.eso.org/sci/facilities/paranal/instruments/crises/doc/VLT-MAN-ESO-14500-3486_v93.pdf)

in which the target is reacquired multiple times. We therefore discarded the fourth detector for the remainder of the analysis.

#### 4.3.4 Removal of telluric lines

In these ground-based, high-resolution observations, telluric lines dominate over the planet signal in the data by several orders of magnitude. Unlike the planet signal, telluric lines are stationary in wavelength and can therefore be removed (i.e., normalized) by modeling the flux of each resolution element (i.e., each column of the matrix) in time. In previous work (de Kok et al. 2013b; Birkby et al. 2013), we have tested several ways of performing this task, including Singular-Value Decomposition and the SYSREM algorithm (Tamuz et al. 2005). Here we followed the approach of Chapter 2 and detrended the data for airmass. This approach works well when the contribution from stellar lines is negligible and the dominant factor driving the instrument performances (resolution, stability, and throughput) is the airmass.

The various stages of the telluric removal are shown in Figure 4.1. We first normalized each spectrum in the series by its median value, in order to correct for varying throughput (panel *b*). We then fit the logarithm of the flux in each of the detector pixels (i.e., each column in the matrix) with a linear function of airmass. This step removed the main airmass dependence, but left strong residuals in the data, at the level of 1-2 percent, at the position of some of the telluric lines (panel *c*). These second order effects are due to differential airmass effects (e.g., changes in the atmospheric water vapor content) and/or changes in the instrument profile during the night. In order to remove these effects, we sampled the strongest residuals at the position of 2-3 telluric lines per detector, and we modeled every other pixel as a linear combination of these, determined through linear regression. This very effectively detrended most of the telluric contamination in the data (panel *d*). Away from the cores of deep absorption lines, we achieve an r.m.s. which is at most  $\sim 15\%$  higher than the photon noise. At the core of strong absorption lines, the r.m.s. is a factor of 2-4 $\times$  higher than the photon noise, but these columns account for a small portion of the data, so that on average we obtain noise levels within 20% from the photon noise. In order to account for the different signal-to-noise as a function of wavelength, we normalized each column in the data matrix by its standard deviation squared (panel *e*).

## 4.4 Extraction of the planet signal

Even after applying the telluric removal explained in Section 4.3.4, the planet signal is still buried in the noise, as shown in the lowest panel of Figure 4.1. Depending on the molecular species contributing to the opacity at 2.3  $\mu\text{m}$  and their relative abundances, the planet spectrum consists of tens to hundreds of molecular lines Doppler-shifted with respect to their rest-frame frequencies according to the radial component of the planet orbital velocity. In order to enhance the planet signal, we funneled the information of these many molecular lines toward a single function, which was achieved by cross-correlating the data with model spectra for the planet

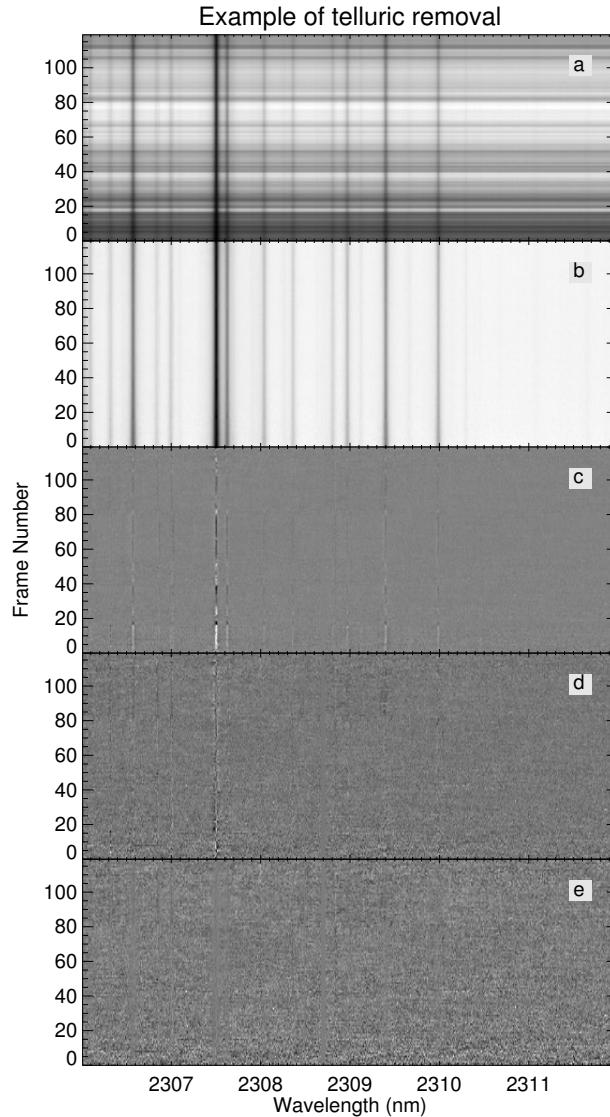


Figure 4.1: Example of telluric lines removal. Panel (a) shows a sequence of 120 spectra of HD 179949 observed during the night of July 19, 2011. A small portion of detector 2 of CRILES is shown, corresponding to the wavelength range 2306-2312 nm. The spectra are first normalized by their median value (b). Subsequently, the flux in each column is divided through its linear fit with airmass (c). A linear combination of the strongest residuals is utilized to detrend second-order effects (d) and finally each column is normalized by its standard deviation squared (e).

atmosphere. The rest of this Section explains how these models and the cross correlation were computed.

#### 4.4.1 Model spectra

Model spectra of HD 179949 b were constructed using an average temperature-pressure ( $T/p$ ) profile describing the vertical structure of the visible hemisphere of the planet atmosphere. This profile was parametrized by two points in the ( $T, p$ ) space, namely  $(T_1, p_1)$  and  $(T_2, p_2)$ . The atmosphere was assumed to be isothermal for pressures  $p > p_1$  and  $p < p_2$ , at temperatures  $T_1$  and  $T_2$  respectively. For  $p_1 > p > p_2$ , a constant lapse rate was adopted, given by

$$\frac{dT}{d \log_{10}(p)} = \frac{T_1 - T_2}{\log_{10}(p_1) - \log_{10}(p_2)}. \quad (4.1)$$

Inverted and non-inverted  $T/p$  profiles were therefore obtained by choosing  $T_2 > T_1$  and  $T_2 < T_1$ , respectively. The model spectra are the result of line-by-line calculations including H<sub>2</sub>-H<sub>2</sub> collision-induced absorption (Borysow & Fu 2001; Borysow 2002) and absorption from three trace gases, CO, H<sub>2</sub>O, and CH<sub>4</sub>, which are the dominant sources of opacities at these wavelengths (Madhusudhan 2012; Moses et al. 2013). Line data for the trace gases were taken from HITEMP 2010 for H<sub>2</sub>O and CO (Rothman et al. 2010), and HITRAN 2008 for CH<sub>4</sub> (Rothman et al. 2009). A Voigt line profile was used for the calculations, with broadening coefficients obtained from the HITEMP/HITRAN databases and accounting for pressure broadening only. As a result of the high temperatures involved, this carries the dominant contribution to the line profiles. The methane line list is known to contain two strong but apparently spurious absorption lines in this wavelength range (S. Yurchenko and J. Tennyson, private communication), at 2326.90 nm and 2335.14 nm. These lines were therefore removed from the input of our models. We also compared the strengths of the molecular lines in the HITRAN and EXOMOL databases, finding a good agreement between them. Because of computational reasons and to the degeneracies affecting these high-dispersion observations (see Section 4.4.3 below), we did not explore a full grid of parameters by varying temperatures, pressures, and molecular abundances at the same time. We instead tested pressures in the range  $(-4.5 < \log_{10}(p_2) < -1.5)$  in steps of 1.0 dex, while  $p_1$  was fixed to 1 bar, which is approximately the expected continuum level for these gaseous planets (de Kok et al. 2013a).

We first computed planet spectra by including a single trace gas. We utilized the upper limit of  $\sim 20\%$  on the recirculation efficiency set by Cowan et al. (2007) in combination with Eq. 4 of Cowan & Agol (2011) in order to get an estimate of the dayside temperature of HD 179949 b, which was found to be  $T_{\text{eq}} \simeq 1950$  K. Different assumptions for the recirculation efficiency would lead to dayside temperatures between 1570 K (full recirculation) and 2000 K (no recirculation). We set  $T_1 = T_{\text{eq}}$ , and explored  $T_2 = [1450, 1800, 2150]$  K. The chosen Volume Mixing Ratios (VMRs) of the three molecules were  $\text{VMR} = [10^{-6}, 10^{-5}, 10^{-4}]$ . This first set of models allowed us to determine which species are significantly detected, and to

determine the presence or the absence of an inversion layer, as discussed in Section 4.5.1. We then computed an additional grid of models with the same choice of  $p_1$ ,  $p_2$ , and  $T_1$ , but with only non-inverted profiles ( $T_2 = 1450$  K), since we did not detect any significant cross-correlation from models with  $T_2 > T_1$ . In this case, the VMR of CO was set to  $10^{-4.5}$ , which roughly matches the measured line contrast ratio of the planet spectrum (see Sects. 4.4.3 and 4.5.1). The abundances of H<sub>2</sub>O were varied in the range ( $-8.5 < \log_{10}(\text{VMR}) < -2.5$ ) and those for CH<sub>4</sub> in the range ( $-9.5 < \log_{10}(\text{VMR}) < -4.5$ ), with steps of 1 dex. This choice covers the whole range of relative abundances for a hot Jupiter with the above  $T_{\text{eq}}$ , as a function of its C/O ratio (Madhusudhan 2012). As explained in Section 4.5.2, we determined the best-fitting model for the planet atmosphere, the planet mass, the orbital inclination, and the atmospheric C/O ratio by using this second grid of models.

#### 4.4.2 Cross correlation and signal retrieval

We cross correlated each of the model spectra with the telluric-removed data by utilizing a lag vector corresponding to radial velocities (RVs) in the range  $-250 < V < 250$  km s<sup>-1</sup>, in steps of 1.5 km s<sup>-1</sup>. This range was chosen in order to cover all the possible RVs for the planet, with the step size approximately matching the pixel scale of the instrument detectors at this wavelength.

For each RV value, we Doppler-shifted the model spectrum and computed its cross correlation with the time series of the observed spectra. In this way we obtained the strength of the cross-correlation signal as a function of radial velocity and time, that is  $\text{CCF}(V, t)$ . This computation was first performed for each night and each detector separately. Subsequently, the CCF matrices of the three CRILES detectors were summed after weighting each CCF by the S/N of the corresponding spectrum. As explained above, the fourth CRILES detector was excluded from the analysis. Finally, the CCFs of the three nights were summed in time. This last step was performed by first shifting each CCF to the rest frame of the planet, which implies the knowledge of the planet radial velocity curve, the velocity of the observer with respect to the barycenter of the solar system ( $V_{\text{obs}}(t)$ ) and the systemic velocity of HD 179949, that is  $V_{\text{sys}} = (-24.35 \pm 0.18)$  km s<sup>-1</sup> (Butler et al. 2006):

$$V_{\text{P}}(t) = K_{\text{P}} \sin[2\pi\varphi(t)] + V_{\text{obs}}(t) + V_{\text{sys}}. \quad (4.2)$$

In the above Equation  $\varphi$  is the planet orbital phase, and  $K_{\text{P}}$  is the amplitude of the planet orbital radial velocity. Since  $K_{\text{P}}$  is unknown for a non-transiting planet, we assumed a range of ( $0 \leq K_{\text{P}} \leq 170$ ) km s<sup>-1</sup>, which corresponds to all the possible orbital inclinations of the system, plus some unphysical values ( $\sin i > 1$ ) as a sanity check. In the case of our best-fitting model (see Section 4.5.2), we extended the range to negative  $K_{\text{P}}$ . This is done to further assess the robustness of the total cross-correlation signal, as discussed in Sect 4.5.3. For each value of  $K_{\text{P}}$ , the planet radial velocity curve was computed, each CCF was shifted to the planet rest frame, and the signal was summed in phase. In this way we obtained the total strength of the cross correlation signal as a function of the planet rest-frame velocity ( $V_{\text{rest}}$ ) and projected orbital velocity ( $K_{\text{P}}$ ), which is shown in Figures 4.2 and 4.4. We note

that, in the case of HD 179949 b, the exact orbital phase is an additional source of uncertainty in computing Eq. 4.2. The orbital phase is obtained by taking the fractional part of

$$\varphi(t) = \frac{t - T_0}{P}, \quad (4.3)$$

where  $P$  is the orbital period and  $T_0$  the time of inferior conjunction. From the most accurate orbital solution for the planet (Butler et al. 2006) we have  $P = 3.092514(32)$  days and  $T_0 = (2,451,001.516 \pm 0.020)$  HJD, which translates into a  $1\text{-}\sigma$  uncertainty of  $\Delta\varphi = 0.012$  in the orbital phase at the time of observation. Since the systemic and barycentric velocities are known with a much better precision, we iteratively solved for  $\varphi(t)$  by first computing the total cross-correlation signal as a function of  $K_P$ , and then by applying a shift  $\Delta\varphi$  until the planet signal peaked at zero planet rest-frame velocity. This also allowed us to refine the value of  $T_0$ . In all these computations, we made the assumption that the orbit of HD 179949 b is circular. Butler et al. (2006) present weak evidence for a low eccentricity of  $e = (0.022 \pm 0.015)$ , but we did not measure any significant change in the strength of the planet signal by assuming this solution. Therefore, we adopted  $e = 0$  through the remainder of the analysis.

#### 4.4.3 Degeneracies in the atmospheric models

In these high-dispersion observations, each spectrum is renormalized for accurate telluric removal, as described in Section 4.3.4. This means that information on absolute fluxes, as well as on broad-band flux variations, is lost. On the other hand, information on the narrow component of the planet spectrum, e.g., the flux ratio between the planet continuum and the core of the lines, is preserved.

By utilizing the cross correlation to extract information from the data, we were able to investigate two main properties of the planet spectrum. Firstly, we measured the relative strength of the molecular lines with respect to each other, which we henceforth refer to as *relative line ratios*. This property was estimated directly by cross-correlating the model spectra with the data, and by selecting the model giving the highest total cross-correlation signal. Secondly, we measured the average depth of the planet spectral lines with respect to the stellar continuum flux, which we call *average line depth*, in the following way. We scaled the planet model spectrum to units of stellar continuum flux, via

$$F_{\text{scaled}}(\lambda) = \frac{\pi F_P(\lambda)}{F_{\text{star}}(\lambda)} \left( \frac{R_P}{R_S} \right)^2, \quad (4.4)$$

where  $F_{\text{star}}(\lambda)$  is the NextGen low-resolution model spectrum for a HD 179949-like star ( $T_{\text{eff}} = 6200$  K,  $\log g = 4.5$ , solar metallicity),  $R_P$  and  $R_S$  are the planet and stellar radii respectively, and  $F_P(\lambda)$  is the output of our models. The factor of  $\pi$  accounts for the integration over the solid angle. The scaled model ( $F_{\text{scaled}}$ ) was convolved to the CRIRES resolution and subtracted from the data ( $F_{\text{meas}}$ ) before the removal of telluric lines, via

$$F_{\text{sub}}(\lambda) = F_{\text{meas}}(\lambda) [1 - F_{\text{scaled}}(\lambda)]. \quad (4.5)$$

After performing the full analysis, we then cross-correlated the telluric- and model-subtracted data with the same model. When the average line depth of the model matches the average line depth in the observed spectra, the subtraction is perfect and we obtain zero residual cross-correlation signal. This means that the best-fitting model for the planet atmosphere must give at the same time the highest cross-correlation signal, and zero cross-correlation signal when subtracted from the data.

Even by pairing the study of the relative line ratios and the average line depth as outlined above, these high-resolution observations are affected by degeneracies. The contrast between the planet continuum (deeper in the atmosphere) and the line core (much higher in the atmosphere) reflects a *temperature* difference between the two atmospheric layers. This depends on three quantities: the continuum temperature, the atmospheric lapse rate, and the molecular abundances. Therefore, large degeneracies exist when comparing models to the data. For transiting planets, the degeneracies can be lifted since the continuum temperature can be derived from low-resolution measurements of secondary-eclipse depth. However, this is not possible for non-transiting planets and therefore weaker constraints can be placed through phase curves, as in the case of this planet.

In addition,  $R_P$  is also unknown for non-transiting planets. Here we assume  $R_P \simeq 1.35 R_{\text{Jup}}$ , which is the mean radius of the known transiting planets with masses in the range 0.9-1.1  $M_{\text{Jup}}$ , and orbital periods less than 10 days.

## 4.5 Results

### 4.5.1 Single-molecule detections

Figure 4.2 shows the total strength of the cross-correlation signal as a function of the planet rest-frame velocity  $V_{\text{rest}}$  and projected orbital velocity  $K_P$ , as obtained from models containing carbon monoxide only, water vapor only, and methane only. CO and H<sub>2</sub>O are detected, when cross correlating with non-inverted atmospheric models, at a S/N of 5.8 and 3.9 respectively. The level of detection is estimated by dividing the peak value of the cross-correlation by the standard deviation of the noise. No significant cross-correlation is obtained when testing models with thermal inversion. It means that we measure only molecular features in absorption in the atmosphere of HD 179949 b. Finally, models with CH<sub>4</sub> do not result in any cross-correlation signal above the threshold of S/N = 3. The consequences of the measured lack of thermal inversion, and the validity of our models based on a single  $T/p$  profile extending to pressures well above typical levels for inversion layers are discussed in Section 4.6.

We note that the models that contain CO show a different behavior than those based on H<sub>2</sub>O and CH<sub>4</sub> for varying atmospheric vertical structure and molecular abundances. The core of carbon monoxide lines is formed at very high altitudes in the planet atmosphere even for relatively low molecular abundances, resulting in partially-saturated lines due to our assumption of an isothermal planet atmosphere above a certain pressure level. This means that the relative line ratio (defined in



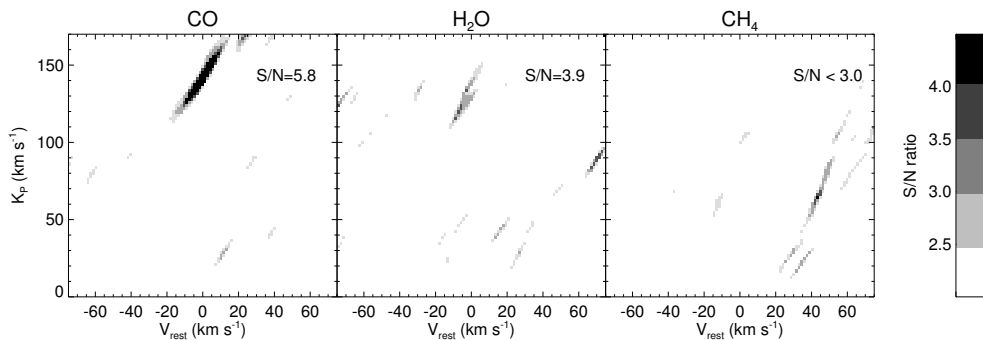


Figure 4.2: Total strength of the cross-correlation signal, as function of rest-frame velocity  $V_{\text{rest}}$  and planet projected orbital velocity  $K_P$ , for atmospheric models containing CO only (left panel), H<sub>2</sub>O only (mid panel), and CH<sub>4</sub> only (right panel). It shows that carbon monoxide and water vapor are detected in the atmosphere of HD 179949 b around  $2.3 \mu\text{m}$ , while methane is not. The signal-to-noise is computed by dividing the value of the cross correlation at each of the positions in the diagram by the standard deviation of the cross-correlation noise. Positive and negative cross-correlation signals are both plotted.

Section 4.4.3) of the CO molecule does not change much with the atmospheric thermal structure or molecular abundances (Figure 4.3, left panel). Conversely, in the case of H<sub>2</sub>O and CH<sub>4</sub>, when the temperature decreases steeply with pressure, or for high molecular abundances, the strongest planet spectral lines tend to saturate, therefore altering the relative line ratios (Figure 4.3, right panel). Because CO dominates the cross-correlation signal at  $2.3 \mu\text{m}$ , the sensitivity of these data to various atmospheric structure is therefore decreased, adding to the degeneracies discussed in Section 4.4.3. From the analysis of relative line ratios of models containing single molecules, we only observe a marginal preference for models with *saturated* line profiles, for both CO and H<sub>2</sub>O.

When investigating the average line depth as explained in Section 4.4.3, we find that models with a steep lapse rate ( $dT/d\log_{10}(p) \geq 300 \text{ K/dex}$ ) and  $\text{VMR}(\text{CO})$  between  $10^{-5}$  and  $10^{-4}$  give zero cross correlation when subtracted from the data. The corresponding line contrast with respect to the stellar continuum is  $(1.74 \pm 0.27) \times 10^{-4}$  and  $(0.86 \pm 0.24) \times 10^{-4}$ , for CO and H<sub>2</sub>O respectively. For the analysis described in Section 4.5.2, we fix  $\text{VMR}(\text{CO})$  to the intermediate value of  $10^{-4.5}$ .

## 4.5.2 Planet mass and orbital inclination

From the previous single-molecule detections, we deduce that the majority of the deepest lines in the dayside spectrum of HD 179949 b comes from CO absorption, which also gives the dominant cross-correlation signal. Additional signal comes from shallower (but more numerous) H<sub>2</sub>O molecular lines. The contribution from methane appears to be negligible, or below the threshold of detectability, at these wavelengths. As explained in Section 4.4.1, we repeated the cross-correlation analy-

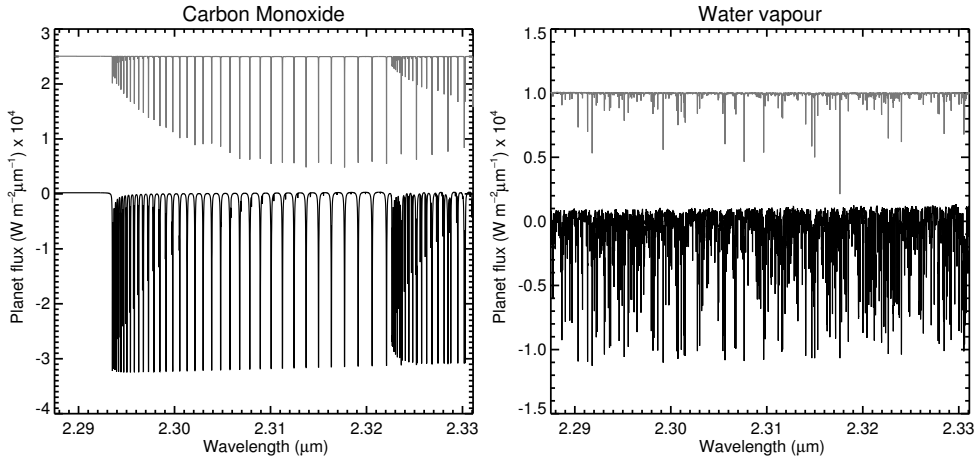


Figure 4.3: Effects of line saturation for models containing pure CO (left panel) and pure H<sub>2</sub>O (right panel). The models are continuum-subtracted and arbitrarily shifted in flux for visualization purposes. The atmospheric  $T/p$  profile is kept constant between the top and bottom models, but the molecular VMR is increased by two orders of magnitude from top to bottom, leading to saturation of the strongest lines. The same effects could be obtained by keeping the abundances constant, and increasing the lapse rate  $dT/d\log(p)$ .

sis by utilizing a grid of models containing the three gases in a wide range of relative molecular abundances.

Our analysis shows that a model with  $\text{VMR}(\text{CO}) = 10^{-4.5}$ ,  $\text{VMR}(\text{H}_2\text{O}) = 10^{-4.5}$ ,  $\text{VMR}(\text{CH}_4) = 10^{-9.5}$ , and a steep lapse rate of  $dT/d\log(p) \sim 330$  K per pressure decade is the best fit to the atmosphere of HD 179949 b, meaning that it gives the strongest cross-correlation signal, corresponding to an  $S/N = 6.3$ . Statistical tests on the measured signal and on the properties of the cross-correlation noise are presented in Section 4.5.3, and lead to a significance of  $5.8\sigma$ , in line with the above estimate. The  $S/N$  of the detection is only weakly dependent on the atmospheric lapse rate, meaning that it decreases by only  $\sim 0.5$  when reducing the lapse rate by a factor of 3.

In Figure 4.4 we present the total cross correlation signal from the best fitting model indicated above, which peaks at a planet projected orbital velocity of  $K_P = (142.8 \pm 3.4) \text{ km s}^{-1}$ . The planet signal is retrieved at zero rest-frame velocity when applying a phase shift of  $\Delta\varphi = -0.00477 \pm 0.00069$ , which translates into a refined time of inferior conjunction of  $T_0 = (2,455,757.8190 \pm 0.0022) \text{ HJD}$ . Since the stellar RV semi-amplitude is known from previous measurements to be  $K_S = (0.1126 \pm 0.0018) \text{ km s}^{-1}$  (Butler et al. 2006), we can now treat the system HD 179949 as a spectroscopic binary. The mass ratio between the star and the planet is  $M_S/M_P = K_P/K_S = (1268 \pm 36)$ , which translates into a planet mass of  $M_P = (0.98 \pm 0.04) M_{\text{Jup}}$  by using the known stellar mass (see Section 4.2). Through Kepler’s Third Law, we can compute a planet orbital velocity of  $V_{\text{orb}} = (154.4 \pm 1.7) \text{ km s}^{-1}$ . The orbital

inclination of the system is therefore  $i = \sin^{-1}(K_P/V_{\text{orb}}) = (67.7 \pm 4.3)$  degrees.

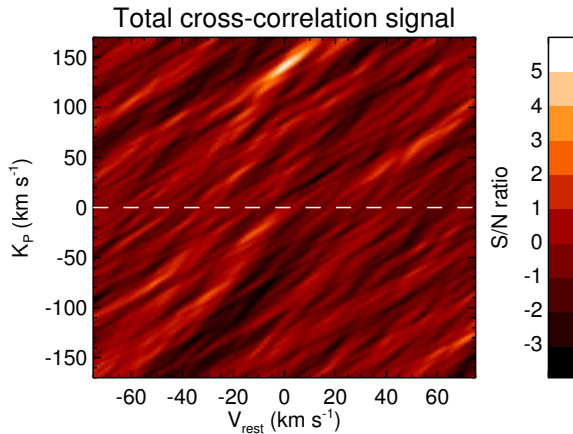


Figure 4.4: Total cross correlation signal from our best-fitting model (see Section 4.5.2) for the atmosphere of HD 179949 b, shown as a function of rest-frame velocity and planet projected orbital velocity. The model contains CO and H<sub>2</sub>O with equal molecular abundance. The planet is detected with a S/N ratio of 6.3, at a planet projected orbital velocity of  $K_P = (142.8 \pm 3.4)$  km s<sup>-1</sup>, which translates into a planet mass of  $M_P = (0.98 \pm 0.04) M_{\text{Jup}}$  and an orbital inclination of  $(67.7 \pm 4.3)$  degrees.

### 4.5.3 Statistical tests on the measured signal

The computation of the total cross-correlation signal in Figure 4.4 is extended to negative planet orbital velocities ( $K_P < 0$  km s<sup>-1</sup>) to test the robustness of the detection. For negative velocities, which imply an unrealistic retrograde planet orbit, the interaction between the model spectrum and any possible red noise in the data would be similar to the corresponding positive  $K_P$ , so false-positive signal would show up as a mirrored image of the  $K_P > 0$  plane, while real planet signals would not. In our case, there is no significant signal in the bottom half of the diagram, reinforcing the robustness of the detection.

Furthermore, we determined the statistical significance of the signal as in previous work (Chapters 2 and 3; de Kok et al. 2013b; Birkby et al. 2013). Firstly, we studied the properties of the cross-correlation noise. From the matrix containing the cross correlation signal as function of planet radial velocity and time,  $\text{CCF}(V, t)$ , we selected those values not belonging to the planet RV curve. In Figure 4.5 (top panel) we show their histogram with a black solid line, and a Gaussian fit with a gray line. It shows that the distribution of the cross-correlation noise is in excellent agreement with a Gaussian distribution. Subsequently, we compared the distributions of the cross-correlation values inside and outside the planet RV curve, shown by the black and gray histograms in the bottom panel of Figure 4.5. Even at a visual inspection, it is possible to assess that the distribution containing the planet signal is

systematically shifted toward higher values than the distribution of the noise. This can be tested statistically by using a Welch  $t$ -test (Welch 1947). For the signal from HD 179949 b, we were able to reject the hypothesis that the two distributions are drawn from the same parent distribution at the  $5.8\sigma$ , in line with the measured S/N.

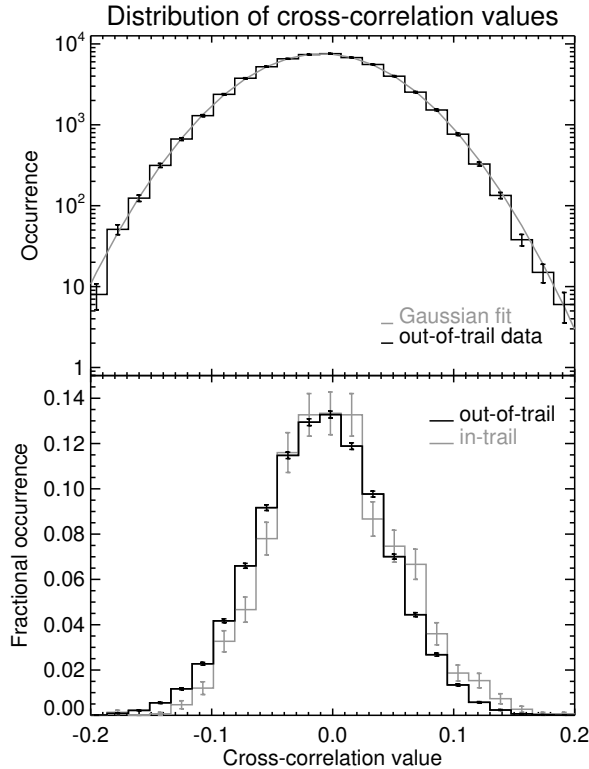


Figure 4.5: *Top panel*: distribution of the cross-correlation values not belonging to the planet RV curve (black histogram) compared to a Gaussian fit (gray line). The two curves are in excellent agreement across the entire range. *Bottom panel*: comparison between the distribution of the cross-correlation values outside and inside the planet RV trail (black and gray histograms, respectively). The latter are systematically shifted toward higher values. A Welch  $t$ -test on the data rejects the hypothesis that the two distributions are drawn from the same parent distribution at the  $5.8\sigma$  of confidence level.

#### 4.5.4 Constraints on the C/O ratio

In Figure 4.6 we plot the measured S/N of the cross-correlation signal as a function of the relative molecular abundances of CO and H<sub>2</sub>O on the horizontal axis, and CO and CH<sub>4</sub> on the vertical axis. The top and bottom panels correspond to a steep and shallow atmospheric lapse rate, respectively. As already noticed in Section 4.5.1, the strength of the total cross correlation signal is only weakly dependent on the

atmospheric lapse rate, so that the top and the bottom plots are qualitatively very similar. Moreover, when CO is highly overabundant compared to H<sub>2</sub>O and CH<sub>4</sub>, the measured signal to noise approaches that of models with CO alone, i.e., S/N = 5.9 (upper right quadrants of the two panels in Figure 4.6).

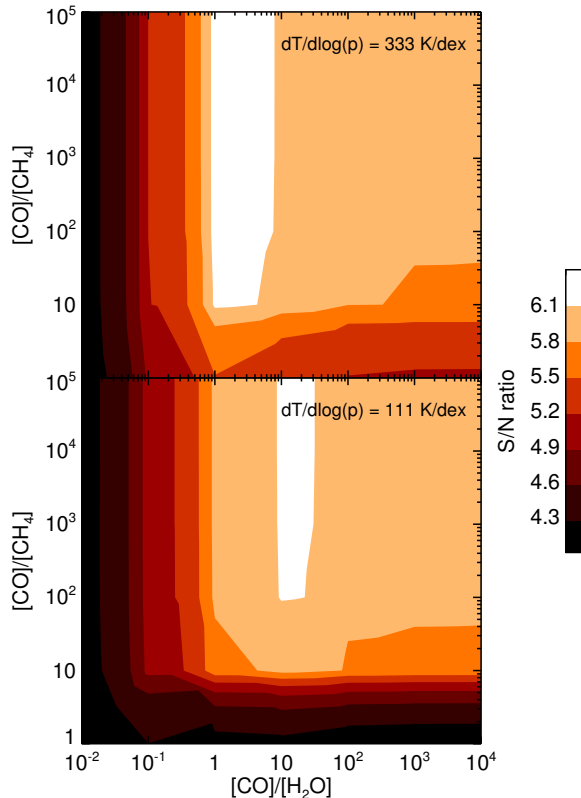


Figure 4.6: S/N of the cross-correlation signal as function of  $\text{VMR}(\text{CO})/\text{VMR}(\text{H}_2\text{O})$  on the horizontal axis, and  $\text{VMR}(\text{CO})/\text{VMR}(\text{CH}_4)$  on the vertical axis. The results are shown for a lapse rate of 111 K per decade in pressure (lower panel) and 333 K per decade in pressure (upper panel). These are the minimum and maximum values investigated with the atmospheric models containing CO, H<sub>2</sub>O, and CH<sub>4</sub>.

By assuming that CO, H<sub>2</sub>O, and CH<sub>4</sub> are the dominant carbon- and oxygen-bearing molecules at our observed wavelengths, we computed the C/O ratio corresponding to each of our planet spectra as

$$\text{C/O} = \frac{\text{VMR}(\text{CO}) + \text{VMR}(\text{CH}_4)}{\text{VMR}(\text{CO}) + \text{VMR}(\text{H}_2\text{O})}. \quad (4.6)$$

We note that the above assumption neglects any possible contribution from CO<sub>2</sub>, C<sub>2</sub>H<sub>2</sub>, and HCN. Firstly, these molecules cannot be detected with these data, because they are not significant sources of opacity at 2.3  $\mu\text{m}$ . Moreover, their equilibrium abundances are at least one order of magnitude lower than CH<sub>4</sub> (Madhusudhan

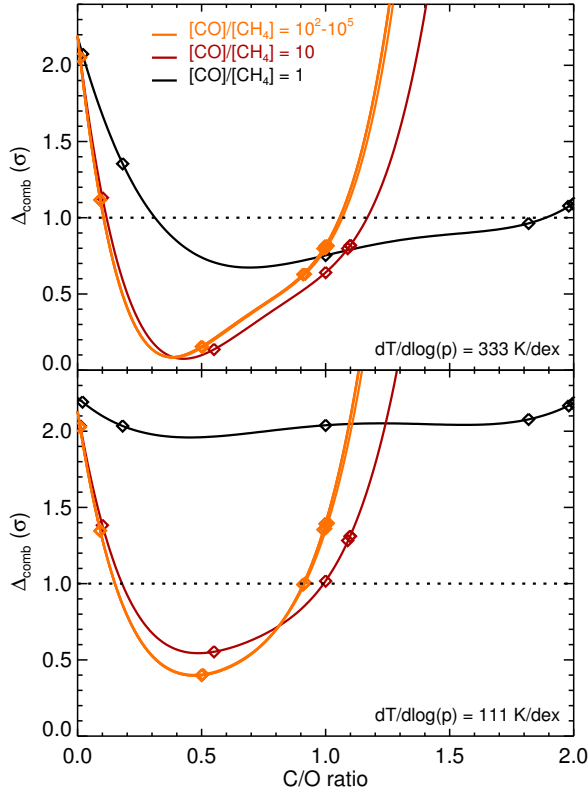


Figure 4.7: Deviation from the best-fitting model ( $\Delta_{\text{comb}}$ ) as a function of C/O ratio, for atmospheric lapse rates of 333 K/dex (top panel) and 111 K/dex (bottom panel). The C/O ratio is derived from the molecular abundances according to Eq. 4.6. Since multiple combinations of molecular abundances give approximately the same C/O ratio, here we plot curves ranging from a high methane abundance ( $[\text{CO}]/[\text{CH}_4] = 1$ , black curve) to low methane abundance ( $[\text{CO}]/[\text{CH}_4] \geq 10^2$ , orange curve). The points are fit with fourth-order polynomials. Except for steep lapse rates with highly-abundant methane, our analysis suggests an oxygen-rich atmosphere for HD 179949 b.

2012), except for high C/O ratio. This would also imply a high methane abundance, which is inconsistent with our non detection of CH<sub>4</sub> in this data.

In Section 4.5.2, we verified that the measured S/N closely matches the significance of the detection as measured by using a statistical approach. Therefore, we can determine 1- $\sigma$  limits on the relative molecular abundances by using the values of S/N, and we can constrain from those the C/O ratio.

We computed the difference between the S/N of each model and that of the model giving the highest cross-correlation, which we denote here with  $\Delta_{\text{meas}}$ . In addition, we also computed the expected cross-correlation signal if the planet spectrum would be identical to each of our model spectra. In order to do this, we subtracted

the best-fitting model after scaling it in the same way as for measuring the average line depth (see Section 4.4.3). We then scaled each of the planet spectra to the measured average line depth, and summed it to the data. After running the data analysis for telluric removal, we cross-correlated with the same model, which gave us the expected planet signal. Finally, we computed the difference between the expected signal and the signal measured by cross-correlating with real data, denoted with  $\Delta_{\text{exp}}$ .

By assuming that  $\Delta_{\text{meas}}$  and  $\Delta_{\text{exp}}$  are independent quantities and that they are good proxies for the statistical significance of the signal, we described their combination as a bivariate normal distribution, and we computed the deviation of each model from the best-fitting model according to

$$\Delta_{\text{comb}} = \sqrt{\Delta_{\text{meas}}^2 + \Delta_{\text{exp}}^2}. \quad (4.7)$$

In Figure 4.7 we plot  $\Delta_{\text{comb}}$  as a function of the planet C/O ratio, for atmospheric lapse rates of 333 K/dex (top panel) and 111 K/dex (bottom panel). The region above  $\Delta_{\text{comb}} = 1$  denotes the models which deviate from the best-fitting model by more than  $1\text{-}\sigma$ . Except for the case of highly-abundant methane ( $[\text{CO}]/[\text{CH}_4] = 1$ , black line in Figure 4.7) and a steep lapse rate, our analysis favors a  $\text{C/O} < 1$ , with a best fitting value of  $\text{C/O} = (0.5^{+0.6}_{-0.4})$ . Our analysis therefore suggests an oxygen-rich atmosphere for HD 179949 b.

We note that the non-detection of CH<sub>4</sub> loosens any constraint on the C/O ratio based on the above analysis. This is because the cross-correlation is almost insensitive to progressively increasing abundances of methane, unless its volume mixing ratio equals that of CO. This also means that our estimate of the C/O ratio could potentially be biased due to inaccuracies in the high-temperature methane line list. These could wash out the cross-correlation signal from CH<sub>4</sub>, and/or increase its detection threshold.

## 4.6 Discussion and future prospects

Thanks to high-resolution spectroscopic observations in the near-infrared, we were able to detect molecular absorption from carbon monoxide and water vapor in the atmosphere of the non-transiting exoplanet HD 179949 b. By tracing the planet radial velocity directly, we also solved for the planet mass and the system inclination.

We do not observe a significant signal when cross-correlating with models containing a thermal inversion. This suggests that overall the temperature decreases with altitude in the observed range of the dayside planet atmosphere. Although weak thermal inversion at high altitude is still possible, these observations exclude the presence of a strong thermal inversion, which would produce molecular lines observed in emission. We note that our assumption of an inversion layer extending down to pressures of 1 bar might be too simplistic and not representative of realistic temperature inversions. In particular, the ability of observing emission lines in the spectrum is dependent on the typical atmospheric pressures probed by the CO template as a whole. In order to exclude that our measured lack of thermal inversion

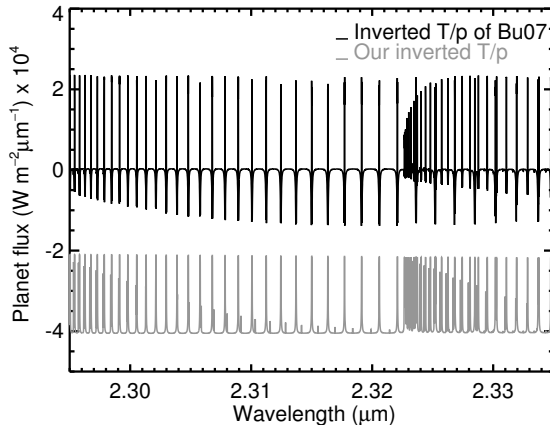


Figure 4.8: Comparison between the best fitting  $T/p$  profile of Burrows et al. (2007) for the atmosphere of HD 209458 b (top curve) and our models with temperature inversion, for a  $\text{VMR}(\text{CO}) = 10^{-4}$ . In both cases, emission lines due to the thermal inversion layer are clearly visible and dominate the narrow component of the planet spectrum.

is a product of the particular parametrization chosen for the planet atmosphere, we computed a set of models based on the best-fitting inverted  $T/p$  profile presented in Burrows et al. (2007) for the exoplanet HD 209458 b (see their Figure 2, green line), which is often considered the prototype of planets with atmospheric inversion layers. For these calculations we assumed  $\text{VMR}(\text{CO}) = (10^{-5}, 10^{-4}, 10^{-3})$ . In line with the previous analysis, we do not detect any planet signal by cross-correlating with these models.

Figure 4.8 shows one of these models (for a VMR of CO of  $10^{-4}$ ) compared to the corresponding model spectrum utilized in this paper. The only qualitative difference produced by a more realistic  $T/p$  profile is that the line wings are seen in absorption, while the line core shows emission. Overall the template still shows strong emission lines, and this happens because at very high resolution the narrow component of the planet spectrum (which is the component detected through cross-correlation) probes pressures several order of magnitude lower than those of the continuum part, including the typical altitudes at which thermal inversion layers are thought to form. This is illustrated by Figure 4.9, showing the CO contribution function for the model based on the Burrows et al. (2007) profile. Although the line wings probe deep in the atmosphere, where realistic thermal inversions might not persist, the sensitivity to this part of the spectrum is very low due to our data analysis (see Section 4.4.3). We instead remain sensitive to the contrast between the broad and the narrow component of the spectrum, which probes 4-5 orders of magnitude in pressures as a whole and encompasses the thermal inversion layers as well, corresponding to molecular lines observed in emission. We can therefore conclude that, based on our analysis, HD 179949 b does not show a HD208458b-like inversion.



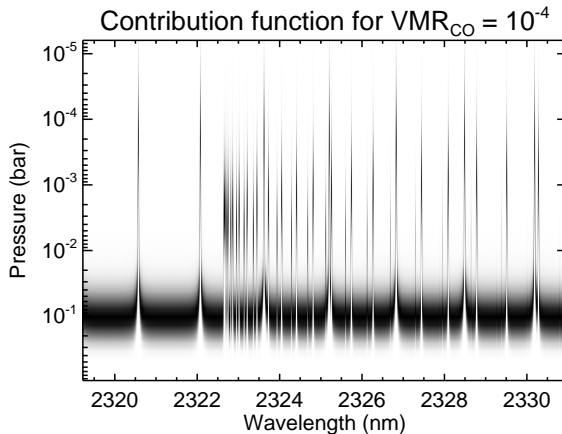


Figure 4.9: Contribution function for the model spectrum of HD 179949 b computed with the Burrows et al. (2007)  $T/p$  profile (Figure 4.8, top curve). The color scheme runs from zero contribution (white) to maximum contribution (black). The broad component of the spectrum is formed at relatively high pressures (deeper in the atmosphere) and typically probes a non-inverted portion of the  $T/p$  profile. On the other hand, the narrow component of the spectrum, to which we are sensitive at high resolution, probes several orders of magnitude in pressure and encompasses thermal inversion layers as well, producing molecular lines in emission.

Thermal inversion layers might be influenced by the incident stellar flux (Fortney et al. 2008), with the most irradiated planets being capable of retaining in the gas phase high-altitude optical absorbers, such as TiO or VO, whereas these compounds would condense and rain out at lower irradiation levels. The planet HD 179949 b receives a stellar flux of  $\sim 1.4 \times 10^9 \text{ erg cm}^{-2} \text{ s}^{-1}$ , which according to the Fortney et al. (2008) classification should be enough to keep optical absorbers in the gas phase. However, stellar activity could also influence the onset of thermal inversion layers, because of the UV stellar flux potentially destroying the above-mentioned absorbers (Knutson et al. 2010). With an activity index of  $R'_{HK} = -4.72$ , HD 179949 can be considered an active star, so that the observed lack of a thermal inversion could fit in this scenario. However, it has recently been pointed out that a potential key factor in determining the equilibrium chemical composition of a hot Jupiter is the C/O ratio (Madhusudhan 2012). For carbon-rich planets, there is little oxygen left for the formation of oxides, meaning that molecules like TiO and VO would be under-abundant in these atmospheres, and could not cause a thermal inversion layer.

The observational evidence for a carbon-rich planet has been presented for the hot-Jupiter WASP-12 b, based on photometric measurements of its secondary-eclipse depth (Madhusudhan et al. 2011). Subsequently, the discovery of a faint nearby star diluting the light of the system revised the slope and the shape of the dayside spectrum, so that the assumption of a high C/O ratio, although not inconsistent with the data, is not the only possible explanation for the planet atmosphere (Crossfield

et al. 2012).

In this work we derive limits on the relative molecular abundances of CO, H<sub>2</sub>O, and CH<sub>4</sub>, and we translate them into a measurement of the atmospheric C/O ratio. However, due to the fact that around 2.3  $\mu\text{m}$  CO dominates the cross-correlation signal and that CH<sub>4</sub> is not detected, only loose limits on relative abundances could be derived. These are insufficient to robustly constrain the C/O ratio, so that the hypothesis of a carbon-rich planet as explanation for the lack of a thermal inversion layer cannot be tested yet, although our analysis tends toward a low C/O ratio.

In order to improve these measurement, one would need to detect multiple molecules at multiple wavelengths. For example, as shown in (de Kok et al. 2013a), the region around 3.5  $\mu\text{m}$  is expected to contain the detectable signatures of H<sub>2</sub>O, CO<sub>2</sub>, and CH<sub>4</sub>. By linking observations at 2.3  $\mu\text{m}$  and 3.5  $\mu\text{m}$ , it is in principle possible to measure the relative abundances of the four major C- and O-bearing molecular species in hot-Jupiter atmospheres, which would definitely improve constraints on the planet C/O ratio.

Moreover, for molecular species such as water vapor and methane, which absorb across a wide spectral range, high-resolution spectrographs capable of covering one or multiple NIR bands in a single setting would be beneficial to these observations, since the cross-correlation signal scales roughly as the square root of the number of strong molecular lines. The upgrade of CRIRES to a cross-dispersed spectrograph will increase the spectral range of the instrument by a factor of  $\sim 6$ . Moreover, although mounted on smaller telescopes, more NIR spectrographs with an even wider spectral range, such as CARMENES (Quirrenbach et al. 2012) and SPIRou (Thibault et al. 2012), will come on-line in the northern hemisphere.

## Acknowledgements

We thank Simon Albrecht and Ernst de Mooij for their contribution to the design of high-resolution observations in the near-infrared, and for the constructive discussion about the results from our large program. We thank Sergey Yurchenko and Jonathan Tennyson for their useful insights on the comparison between the EXOMOL and HITRAN spectroscopic line list of methane. R. d. K acknowledges support from the Netherlands Organisation for Scientific Research (NWO).

## Bibliography

- Arsenault, R., Alonso, J., Bonnet, H., et al. 2003, in Society of Photo-Optical Instrumentation Engineers (SPIE) Conference Series, ed. P. L. Wizinowich & D. Bonaccini, Vol. 4839, 174–185
- Barnes, J. R., Barman, T. S., Jones, H. R. A., et al. 2008, *MNRAS*, 390, 1258
- Birkby, J. L., de Kok, R. J., Brogi, M., et al. 2013, *MNRAS*, 436, L35
- Borysow, A. 2002, *A&A*, 390, 779
- Borysow, A. & Fu, Y. 2001, *J. Quant. Spec. Radiat. Transf.*, 68, 235
- Burrows, A., Hubeny, I., Budaj, J., Knutson, H. A., & Charbonneau, D. 2007, *ApJL*, 668, L171
- Butler, R. P., Wright, J. T., Marcy, G. W., et al. 2006, *ApJ*, 646, 505
- Charbonneau, D., Noyes, R. W., Korzennik, S. G., et al. 1999, *ApJL*, 522, L145
- Collier Cameron, A., Horne, K., Penny, A., & James, D. 1999, *Nature*, 402, 751
- Cowan, N. B. & Agol, E. 2011, *ApJ*, 729, 54
- Cowan, N. B., Agol, E., & Charbonneau, D. 2007, *MNRAS*, 379, 641
- Crossfield, I. J. M., Barman, T., Hansen, B. M. S., Tanaka, I., & Kodama, T. 2012, *ApJ*, 760, 140
- de Kok, R. J., Birkby, J., Brogi, M., et al. 2013a, ArXiv e-prints
- de Kok, R. J., Brogi, M., Snellen, I. A. G., et al. 2013b, *A&A*, 554, A82
- Fares, R., Donati, J.-F., Moutou, C., et al. 2012, *MNRAS*, 423, 1006
- Fortney, J. J., Lodders, K., Marley, M. S., & Freedman, R. S. 2008, *ApJ*, 678, 1419
- Gurdemir, L., Redfield, S., & Cuntz, M. 2012, *PASA*, 29, 141
- Horne, K. 1986, *PASP*, 98, 609
- Kaeufl, H.-U., Ballester, P., Biereichel, P., et al. 2004, in Society of Photo-Optical Instrumentation Engineers (SPIE) Conference Series, ed. A. F. M. Moorwood & M. Iye, Vol. 5492, 1218–1227
- Knutson, H. A., Howard, A. W., & Isaacson, H. 2010, *ApJ*, 720, 1569
- Konopacky, Q. M., Barman, T. S., Macintosh, B. A., & Marois, C. 2013, *Science*, 339, 1398
- Madhusudhan, N. 2012, *ApJ*, 758, 36
- Madhusudhan, N., Harrington, J., Stevenson, K. B., et al. 2011, *Nature*, 469, 64

- Marley, M. S., Gelino, C., Stephens, D., Lunine, J. I., & Freedman, R. 1999, *ApJ*, 513, 879
- Moses, J. I., Madhusudhan, N., Visscher, C., & Freedman, R. S. 2013, *ApJ*, 763, 25
- Quirrenbach, A., Amado, P. J., Seifert, W., et al. 2012, in Society of Photo-Optical Instrumentation Engineers (SPIE) Conference Series, Vol. 8446
- Rothman, L. S., Gordon, I. E., Barbe, A., et al. 2009, *J. Quant. Spec. Radiat. Transf.*, 110, 533
- Rothman, L. S., Gordon, I. E., Barber, R. J., et al. 2010, *J. Quant. Spec. Radiat. Transf.*, 111, 2139
- Shkolnik, E., Walker, G. A. H., & Bohlender, D. A. 2003, *ApJ*, 597, 1092
- Snellen, I. A. G., de Kok, R. J., de Mooij, E. J. W., & Albrecht, S. 2010, *Nature*, 465, 1049
- Sudarsky, D., Burrows, A., & Pinto, P. 2000, *ApJ*, 538, 885
- Tamuz, O., Mazeh, T., & Zucker, S. 2005, *MNRAS*, 356, 1466
- Thibault, S., Rabou, P., Donati, J.-F., et al. 2012, in Society of Photo-Optical Instrumentation Engineers (SPIE) Conference Series, Vol. 8446
- Watson, C. A., Littlefair, S. P., Collier Cameron, A., Dhillon, V. S., & Simpson, E. K. 2010, *MNRAS*, 408, 1606
- Welch, B. L. 1947, *Biometrika*, 34, 28
- Wiedemann, G., Deming, D., & Bjoraker, G. 2001, *ApJ*, 546, 1068



# 5

---

## *Evidence for the disintegration of KIC 12557548 b*

---

The *Kepler* object KIC 12557548 b is peculiar. It exhibits transit-like features every 15.7 hours that vary in depth between 0.2% and 1.2%. Rappaport et al. (2012) explain the observations in terms of a disintegrating, rocky planet that has a trailing cloud of dust created and constantly replenished by thermal surface erosion. The variability of the transit depth is then a consequence of changes in the cloud optical depth. We aim to validate the disintegrating-planet scenario by modeling the detailed shape of the observed light curve, and thereby constrain the cloud particle properties to better understand the nature of this intriguing object. We analysed the six publicly-available quarters of raw *Kepler* data, phase-folded the light curve and fitted it to a model for the trailing dust cloud. Constraints on the particle properties were investigated with a light-scattering code. The light curve exhibits clear signatures of light scattering and absorption by dust, including a brightening in flux just before ingress correlated with the transit depth and explained by forward scattering, and an asymmetry in the transit light curve shape, which is easily reproduced by an exponentially decaying distribution of optically thin dust, with a typical grain size of 0.1  $\mu\text{m}$ . Our quantitative analysis supports the hypothesis that the transit signal of KIC 12557548 b is due to a variable cloud of dust, most likely originating from a disintegrating object.

Brogi, Keller, de Juan Ovelar et al.  
*A&A*, **545**, L5 (2012)

## 5.1 Introduction

Rappaport et al. (2012) recently reported the discovery of a peculiar signal in the light curve of KIC 12557548<sup>1</sup>. A transit-like signal is seen every 15.7 hours, with a depth greatly varying from event to event, ranging from less than 0.2% to more than 1.2%. The transit timing is consistent with a single period and shows no variations down to the  $10^{-5}$  level. This suggests that the changes in transit depth cannot be produced by a fast precession of the orbit, which would in turn require the gravitational perturbation of a second companion in the system. In addition, the phase-folded light curve shows no evidence for ellipsoidal light variations down to 5 parts in  $10^5$ . This sets an upper limit of about  $3 M_{\text{Jup}}$  on the mass of the orbiting object. The explanation proposed by Rappaport et al. (2012) entails the disintegration of a super-Mercury, caused by the high surface temperatures. Material stripped away from the planet surface forms and stochastically replenishes a cloud of dust that obscures part of the stellar disk, causing the dimming of the stellar light to randomly vary from orbit to orbit. Only a planet with mass on the order of Mercury would allow dust particles to accelerate to the escape velocity and form a trailing cloud of sufficient size.

To test the interpretation of Rappaport et al. (2012), a quantitative understanding of the observed transit light curve is required, in particular the asymmetry of the in-transit portion of the light curve and the excess of flux before ingress. We reduced the complete set of publicly available *Kepler* observations, phase-folded the light curve and grouped the transits based on their depth, as explained in Section 5.2. A model for the trailing dust, described in Section 5.3, is then fitted to the data to estimate the transit parameters, the basic shape of the cloud and the average size of the dust particles. The results of our analysis and their interpretation are discussed in Section 5.4.

## 5.2 Analysis of *Kepler* data

The star KIC 12557548 was observed by *Kepler* in *long-cadence* mode, delivering one frame every 29.4 minutes. This results in only 3-4 in-transit points per orbit, and therefore only an averaged and smoothed version of the light-curve can be recovered by phase-folding the photometric time series. The public release of January 2012 extended the available data span to  $\sim 1.4$  years of observations (six quarters) and includes more than 22,000 photometric points. To combine and normalize the entire series, we designed a dedicated data reduction approach that starts with the raw *Kepler* photometry, which is obtained with simple aperture photometry. The *Kepler* pipeline also produces decorrelated photometry, using an automated decorrelation procedure. This, however, often delivers over-corrected light curves, in which the astrophysical signal is reduced or even cancelled together with the instrumental effects<sup>2</sup>. Therefore the decorrelated photometry data are not suitable for our purposes.

---

<sup>1</sup>Henceforth denoted with KIC1255 b

<sup>2</sup><http://keplergo.arc.nasa.gov/ContributedSoftwareKepcotrend.shtml>

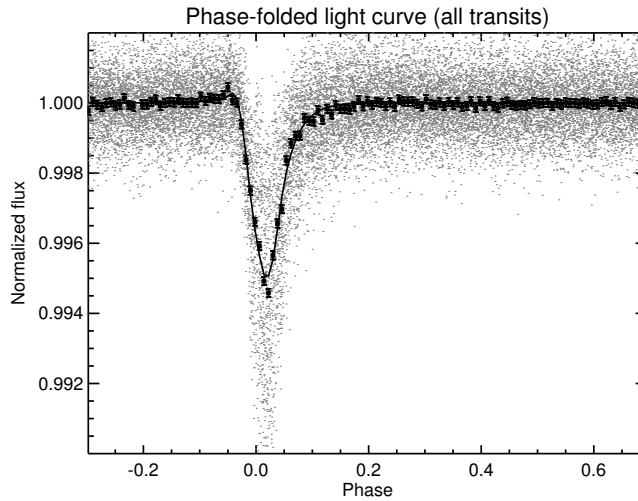


Figure 5.1: The normalized light curve of KIC 1255b, phase-folded using a period of  $P = 15.6854$  hours. A binned light curve (solid squares, with error bars) and the best-fit model (solid line) are overplotted.

A visual inspection of the raw light curve identifies the following features:

1. Jumps in flux from quarter to quarter, at the level of several percent;
2. Jumps or fast variations in flux within a quarter, at the percent level or less;
3. A periodic modulation of the stellar flux, probably due to spots on the rotating surface or other intrinsic stellar variability;
4. Transits-like features with a well-defined cadence but variable depth.

The instrumental systematics can be efficiently modelled with a linear combination of the *Cotrending Basis Vectors* (CBVs), which track the state parameters of the spacecraft and the instrumentation in time<sup>3</sup>. We determined the optimum number of CBVs for each quarter by minimizing the variance of the out-of-transit data, while visually checking that the periodic modulation attributed to stellar activity is preserved as much as possible. For each set of state vectors, we determined their coefficients via linear regression and divided the data by the linear model. In this way different quarters of data were combined and instrumental systematics were minimized while preserving the astrophysical signal. To remove the low-order stellar modulation, we discarded the data points belonging to the transits and averaged the remaining points in each 15.7-hour orbit. This operation was performed separately for each section of contiguous data (i.e., data without temporal gaps) to avoid flux discontinuities. We then spline-interpolated the averaged points in time and divided the light curve by this baseline stellar signal.

<sup>3</sup>see [http://archive.stsci.edu/kepler/release\\_notes/release\\_notes12/DataRelease\\_12\\_2011113017.pdf](http://archive.stsci.edu/kepler/release_notes/release_notes12/DataRelease_12_2011113017.pdf)



### 5.2.1 Transit light curve

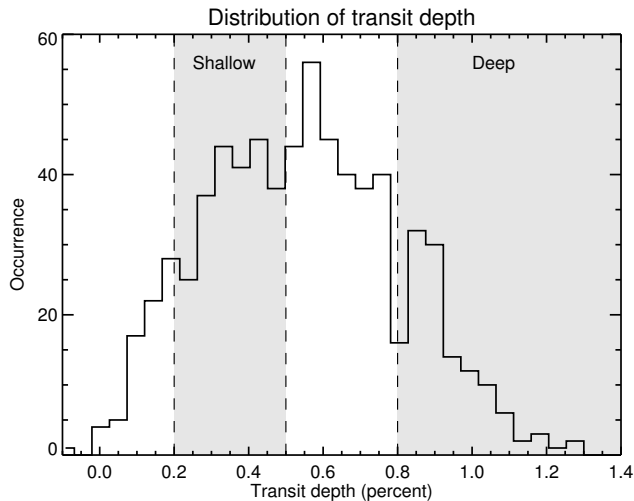


Figure 5.2: Distribution of the transit depths, as measured by fitting the *Kepler* photometry with our model light curve with all parameters but the transit depth fixed to the best-fit values. Orbits that don't sample the in-transit portion of the curve are discarded.

We phase-folded the normalized light curve using a period of  $P = 15.6854$  hours, as determined by Rappaport et al. (2012). The resulting transit light curve is shown in Figure 5.1 with the individual data points in light grey. A relative photometric precision of  $8.2 \times 10^{-4}$  per-point is achieved, which is  $\sim 30\%$  higher than expected from pure photon noise. When binned by 0.008 in phase (black squares in Figure 5.1), the scatter in the data is reduced by a factor of  $\sim 13$ , i.e., the square root of the number of points per bin, suggesting that systematic noise is not significantly present in the data at this level of photometric accuracy. The binned light curve exhibits the following characteristics:

1. An asymmetry between ingress and egress, with the latter being significantly longer than the former;
2. Absence of a secondary eclipse within the photometric precision;
3. A small increase in flux just before ingress.

To assess the dependence of the shape of the transit light curve on transit depth, we divided the events into two extreme classes: *shallow* (depth between 0.2% and 0.5%) and *deep* (depth  $> 0.8\%$ ). These ranges were chosen to maximize the difference in depth while maintaining adequate photometric precision.

We determined the transit depths by first fitting the binned light curve, as explained in Section 5.3, to determine the overall parameters of the transits. Subsequently, each separate orbit was fitted with the same curve, keeping all parameters

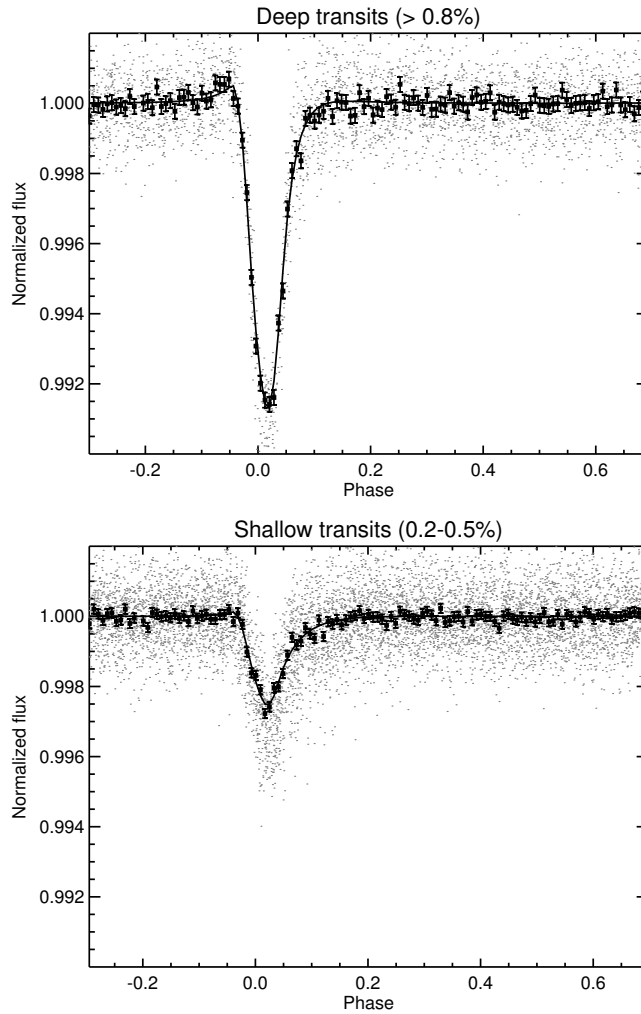


Figure 5.3: Light curves of KIC 1255b, obtained by dividing the events into two groups based on their transit depths and binning the photometry by 0.008 in phase. The top panel shows the average light curve of the deep events (deeper than 0.8%), and the bottom panel shows the average light curve of the shallow events (depths between 0.2% and 0.5%). The best-fit models for the two light curves are shown as a solid line.

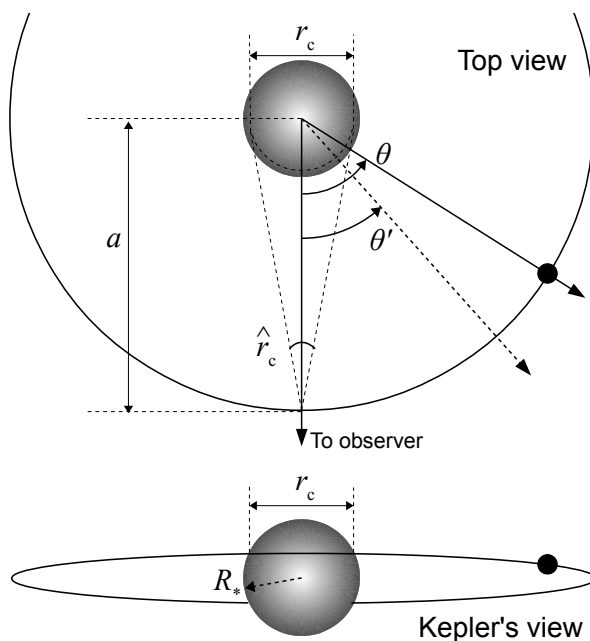


Figure 5.4: Graphical representation of some of the quantities used in our model. The stellar and orbital radius are to scale, while the position of the orbiting body is shown with a black dot.

fixed except for the depth, which we determined by estimating a scaling factor via a  $\chi^2$  minimization. The resulting distribution of transit depths is shown in Figure 5.2. It peaks around 0.6% and extends from zero depth to about 1.3%. The negative transit depths in the histogram are due to noise in the photometry. The absence of a clustering around zero depth suggests that almost every orbit observed by *Kepler* shows a transit-like feature, except for  $\sim 8$  days during quarter 2, in which the signature seems to be absent. This results in an upper limit of the planet radius, as determined in Section 5.4.

The light curves for the deep and shallow transits, shown in Figure 5.3, share the same features of the global light curve except for the flux excess before ingress, which is not evident in the curve for the shallow events. The deep and shallow light curves, binned by 0.008 in phase, have a relative photometric precision per-point of  $1.7 \times 10^{-4}$  and  $1.2 \times 10^{-4}$  respectively. The solid lines in Figure 5.3 show the best-fit model light curves, which were obtained by separately fitting the free model parameters.

### 5.3 The dust model

We created a simple dust model with a minimum number of free parameters to quantitatively model the transit-like light curve. The most relevant variables are

shown in Figure 5.4. We assumed a cloud of dust distributed on a circular orbit at the same radial distance as the parent body ( $a = 0.013$  AU). The latter is supposed to not contribute to the eclipse in a measurable way, as suggested by the absence of any transit-like signals during 8 days of *Kepler* photometry. It is therefore also reasonable to assume that the vertical extent of the cloud is negligible compared to the stellar diameter. Hence our model is one-dimensional, and it is expressed in terms of  $\theta$ , the angle between the observer, the center of the star and the orbiting body. This translates to an orbital phase  $\varphi$  according to  $\theta = 2\pi\varphi$ . The planet crosses a chord of length  $r_c$  on the stellar disk, corresponding to an impact parameter of  $b = [1 - (r_c/2R_*)^2]^{1/2}$  for a stellar radius  $R_*$ . The crossed chord, as seen from the cloud orbit, has an angular extension of  $\hat{r}_c = \arcsin(r_c/2a)$ , which is a free parameter of the model.

The cloud of dust is assumed to be optically thin, and its extinction cross-section  $\rho$  is expressed in units of stellar area. It drops exponentially away from the planet and is parametrized by a multiplicative factor  $c_e$  and by an exponential parameter  $\lambda$ , according to

$$\rho(\Delta\theta) = \frac{\rho_0}{\pi R_*^2} e^{-\lambda(\Delta\theta)} \equiv c_e e^{-\lambda(\Delta\theta)}, \quad (5.1)$$

where  $\Delta\theta = (\theta - \theta')$  is the angular distance between the position of the planet and an arbitrary point along the orbit, measured clockwise. The total model light-curve in units of stellar flux as a function of orbital phase  $\varphi$  is

$$I(\varphi) = \frac{1}{\delta} \int_{2\pi\varphi-\delta/2}^{2\pi\varphi+\delta/2} [1 - I_e(\theta) + I_s(\theta)] d\theta, \quad (5.2)$$

i.e., the stellar flux corrected for the extinction component  $I_e$  and the scattering component  $I_s$ , convolved with a boxcar function that simulates the 29.4-minute exposure time of *Kepler*, which is long compared to the intrinsic temporal variations. The exposure time  $\Delta t$  translates into an angular range of  $\delta = 2\pi\Delta t/P$ , where  $P$  is the orbital period of the planet.

The extinction component  $I_e(\theta)$  is given by

$$I_e(\theta) = \int_0^{2\pi} \rho(\theta - \theta') i(\theta', \hat{r}_c) d\theta', \quad (5.3)$$

which is the convolution between the extinction cross-section and the intensity of the crossed stellar disk  $i(\theta', \hat{r}_c)$ . The latter is described by the limb-darkening law  $i(\mu) = 1 - u(1 - \mu)$ , where  $\mu$  is the cosine of the angle between the line of sight and the normal to the stellar surface, and  $u = 0.79$  is the linear limb-darkening coefficient appropriate for a K4V star in the V-band (Claret 2000). Expressing  $\mu$  in terms of  $\theta'$  and  $\hat{r}_c$  gives

$$i(\theta', \hat{r}_c) = 1 - u \left[ 1 - \frac{a}{R_*} \sqrt{\sin^2(\hat{r}_c/2) - \sin^2 \theta'} \right], \quad (5.4)$$

set to zero for  $\hat{r}_c/2 < \theta' < 2\pi - \hat{r}_c/2$ .

The scattering component  $I_s(\theta)$  is given by

$$I_s(\theta) = \pi\omega \left( \frac{R_*}{a} \right)^2 \int_0^{2\pi} \rho(\theta - \theta') \bar{p}(\theta') d\theta', \quad (5.5)$$

where  $\bar{p}(\theta')$  is the Henyey-Greenstein (H-G) phase function (Henyey & Greenstein 1941)

$$\bar{p}(\theta') = \frac{1 - g^2}{4\pi (1 - 2g \cos \theta' + g^2)^{\frac{3}{2}}}, \quad (5.6)$$

set to zero for  $|\pi - \theta'| \leq \hat{r}_c/2$  to account for the secondary eclipse, and containing a single free parameter, the asymmetry parameter  $g$  with  $-1 < g < 1$ .

In Equation 5.5 we assume that the star is a point source. Since the scattering is beamed with a cone angle  $\phi$  for an asymmetry parameter  $g$ , and  $g \simeq \cos \phi$  (Lamers et al. 1997), the effects of the stellar disk become relevant only when  $\phi \leq 27^\circ$ , the stellar diameter seen from the orbit of the cloud. This corresponds to  $g \geq 0.89$  and therefore our best-fitting values (see Table 5.1) should not be significantly affected by the assumption that the star is a point source. Therefore, we do not include the integration over the stellar disk, which significantly speeds up the model computation. Finally, the single-scattering albedo  $\omega$ , i.e., the ratio between the extinction cross-section and the scattering cross-section, is a free parameter.

The model is fitted to the binned light curves with a Markov-Chain Monte Carlo (MCMC) with a Metropolis-Hastings algorithm (Hastings 1970). Sequences of  $5 \times 10^5$  steps are generated starting from different initial conditions, and merged after discarding the first 10% of data to account for the *burn-in*. The mixing between the chains is tested (Gelman & Rubin 1992) and the  $\pm 1\sigma$  errors of the parameters are computed by measuring the interval between 15.8% and 84.2% of the merged distribution. The best-fit values and their uncertainties are listed in Table 5.1, for the average light curve and for the deep and shallow transits, respectively.

## 5.4 Results and discussion

The model parameters describing the fit to the average light curve do not exhibit typical signs of bias due to the fact that we are averaging events of all depths: i) different MCMC chains mix well, indicating that the solution we find is independent of the initial parameter estimates, and ii) the model parameters are intermediate between those of the shallow and deep transit light curves, as expected if the global curve is a combination of the two. Therefore, we will start with discussing the model parameters obtained for the average light curve.

The transits of KIC 1255 b occur at a moderate impact parameter of  $b = 0.63$ . The asymmetric shape of the curve, with a sharp ingress and a slow recovery of the flux in egress, is well explained by a trailing cloud with a density that decreases away from the parent body. The characteristic length of the tail,  $1/\lambda$ , is about 2.5 times the diameter of the stellar disk as seen from the cloud orbit.

The H-G asymmetry parameter  $g$  being close to +1 indicates particles that strongly favor forward scattering over backward scattering. This reproduces the observed flux excess just before ingress. The fact that this happens slightly earlier than the ingress is due to the slow *Kepler* cadence and the limb-darkened stellar profile. Without implementing these two in the model, it is impossible to reproduce the position of the scattering peak. Note that a similar forward-scattering contribution is present

Parameter	Average	Deep	Shallow
$b$	$0.63 \pm 0.03$	$0.46^{+0.02}_{-0.04}$	$0.61 \pm 0.04$
$T_0$	451.9449(3)	451.9461(5)	451.9430(7)
$\lambda$	$5.1 \pm 0.2$	$6.4 \pm 0.3$	$3.86 \pm 0.25$
$c_e$	$0.030 \pm 0.005$	$0.036^{+0.003}_{-0.002}$	$0.012 \pm 0.001$
$g$	$0.874^{+0.011}_{-0.019}$	$0.743^{+0.044}_{-0.064}$	0.87 (fixed)
$\omega$	$0.65^{+0.09}_{-0.10}$	$>0.94$	0.65 (fixed)

Table 5.1: Best-fit parameters and their  $1\sigma$  uncertainties, as derived from the MCMC analysis. From top to bottom: impact parameter, time of mid-transit (in BJD-2,455,000), decay factor, total extinction cross-section (in units of stellar area), asymmetry parameter and single-scattering albedo.

in egress, but it is masked by the dominating absorption of the tail of dust. Finally, the absence of a secondary eclipse is explained by strongly reduced backward scattering.

### 5.4.1 Dependence on depth

A comparison between shallow and deep transits shows that the total extinction cross-section decreases with transit depth, and that its exponential drop is slower for shallower transits. The photometric precision of the shallow light curve is insufficient to detect the forward-scattering peak, therefore we fixed the asymmetry parameter and the albedo to  $g = 0.87$  and  $\omega = 0.65$ , respectively, as resulting from the fit of the global light curve, which has the best photometric precision. Although  $\omega$  and  $g$  for the deep light curve significantly differ from those for the average light curve, we cannot determine whether or not this reflects different physical properties of the particles. In fact, in our MCMC simulations the extinction cross-section and the asymmetry parameter are moderately correlated, due to the fact that the measured transit depth is the summed contribution of the extinction and scattering components. It is impossible to solve this degeneracy with observations at a single wavelength.

### 5.4.2 Constraints on particle size

To constrain the particle size in the cloud, we compared realistic phase functions of silicates with the best-fitting H-G function obtained from the MCMC analysis of the average light curve. Following Bohren & Huffman (1983), we calculated the optical properties of particles given their material (Draine & Lee 1984), shape and size distribution. We assumed spherical grains (i.e, Mie scattering is the dominant process), as expected if the grains liquify before evaporating due to the high temperature. The particle size distribution is described by a power law with a  $-3.5$  exponent, with upper and lower limits left as free parameters. The resulting phase functions

were compared to a range of H-G phase functions constructed by varying  $\omega$  and  $g$  within their  $1\sigma$  uncertainties. A distribution of particles with sizes between 0.04 and 0.19  $\mu\text{m}$  best agrees with the explored range of H-G functions. Although our results are far from conclusive, the analysis suggests that the grains composing the cloud have an average size of  $\sim 0.1 \mu\text{m}$ .

### 5.4.3 The size of the parent body

As explained in Section 5.2.1, during 8 days of *Kepler* observations no transit-like feature is visible. The phase-folded light curve, constructed using the points in that time interval, has an in-transit photometric accuracy of  $2.8 \times 10^{-4}$  per point. This translates into a  $1\sigma$  upper limit of  $1.15 R_{\oplus}$  for the radius of the parent body.

## 5.5 Conclusions

A simple, one-dimensional model of a trailing dust cloud can reproduce the observed light curve of KIC1255 b in exquisite detail. Features such as the flux excess before ingress, the sharp drop in ingress, the pointed shape of the flux minimum and the long flux recovery after egress are all signs of a trailing cloud of dust that periodically occults the star. The most likely origin of this trailing dust is a planetary or sub-planetary body that evaporates due to the intense stellar irradiation. If this is indeed the case, we are presented with the unique opportunity to probe the interior of an exoplanet. Although the geometry of the transit is well constrained by the currently available *Kepler* data, further observations with a faster cadence and multi-wavelength coverage are required to not only constrain the size but also the composition of the grains.

## Bibliography

- Bohren, C. F. & Huffman, D. R. 1983, Absorption and scattering of light by small particles
- Claret, A. 2000, *A&A*, 363, 1081
- Draine, B. T. & Lee, H. M. 1984, *ApJ*, 285, 89
- Gelman, A. & Rubin, D. 1992, *Statistical Science*, 7, 457
- Hastings, W. K. 1970, *Biometrika*, 57, 97
- Henyey, L. G. & Greenstein, J. L. 1941, *ApJ*, 93, 70
- Lamers, H. J. G. L. M., Lecavelier Des Etangs, A., & Vidal-Madjar, A. 1997, *A&A*, 328, 321
- Rappaport, S., Levine, A., Chiang, E., et al. 2012, *ApJ*, 752, 1

# 6

---

## *A search for rotation and atmospheric circulation in the high-resolution transmission spectrum of HD 189733 b*

---

The absorption line profiles in the transmission spectrum of a close-in gas giant depend on the spin rotation and atmospheric circulation of the planet. While the bulk mass of the planet is expected to be tidally locked, atmospheric super-rotation which produced strong eastward jets may significantly enhance the broadening of the line profiles. In addition, strong day- to night-side winds can result in blue-shifted lines. Ground-based high-resolution spectroscopy has the potential to measure these effects. We have conducted a search for these features in the near-infrared, transmission spectrum of the exoplanet HD 189733 b, which was observed at a resolution of 100,000 with VLT/CRIRES around  $2.3 \mu\text{m}$ . We performed the data analysis and signal extraction in a similar way to previous high-dispersion dayside observations. We made use of the changing planet orbital motion to distinguish the Doppler-shifted planet spectrum from the stationary telluric absorption. Subsequently, we cross-correlated the data with models for the planet spectrum and basic atmospheric circulation patterns. We detect the planet transmission spectrum at a S/N of 7.9, by cross-correlating the data with a model containing CO, CO<sub>2</sub>, H<sub>2</sub>O, and CH<sub>4</sub>. The best signal is obtained by applying a velocity broadening of 2.7-3.1 km s<sup>-1</sup> to the model template, indicating a rotational period of 1.9-2.2 days, consistent with the orbital period of the planet and therefore indicating synchronous rotation. This is in line with the theoretical expectation that hot Jupiters reach tidal locking on short timescales. No blueshift due to possible day-to-nightside winds is detected, neither is there evidence for equatorial super-rotation.

Brogi, de Kok, Albrecht et al.  
To be submitted



## 6.1 Introduction

In recent years, high-resolution spectroscopy has enabled robust constraints on fundamental parameters of exoplanet atmospheres. Due to their unique fingerprint at high dispersion, molecular species can be unambiguously identified via line matching, in contrast to the sometimes strong ambiguities in the interpretation of planet spectra observed at low-resolution or with sparse photometric bands. In addition, the planet orbital motion is detected at high spectral resolution. This offers an effective way to disentangle the Doppler-shifted planet spectrum from the contamination of our own atmosphere, which is instead static in wavelength. Furthermore, for non-transiting planets the detection of the planet motion translates into a measurement of the true planet mass and orbital inclination.

High-dispersion observations with CRIRES at the VLT led to the first measurement of the radial velocity of an exoplanet through the detection of CO in the transmission spectrum of HD 209458 b (Snellen et al. 2010), and to the first detection of the atmosphere of a non-transiting planet ( $\tau$  Boötis b, see Chapter 2). These studies were conducted in *K*-band and targeted a ro-vibrational band of carbon monoxide, which is expected to be abundant in hot planet atmospheres in chemical equilibrium, and has a well-known and regularly-spaced sequence of lines. These factors make it one of the best species for detection. More recently, Birkby et al. (2013) and Lockwood et al. (2014) demonstrated the feasibility of high-resolution observations in the *L*-band and detected H<sub>2</sub>O in the atmospheres of a transiting (HD 189733 b) and a non-transiting ( $\tau$  Boötis) planet. The robust detection of water vapor in exoplanet atmospheres has arguably a great importance in the context of exoplanet habitability. Moreover, H<sub>2</sub>O has a much more complicated high-resolution signature than carbon monoxide (see, e.g., Figure 4.3) and the telluric absorption at 3.2-3.5  $\mu\text{m}$  is more severe, making it a good test for the robustness of these observational methods. It is also worth noting that the detection of Lockwood et al. (2014) was obtained by utilizing NIRSPEC at Keck, at only 1/4 of the resolving power of CRIRES (25,000 instead of 100,000), but with a wider wavelength range. This demonstrates that spectral resolution can be partially traded for spectral coverage for this type of observations, as further discussed in Chapter 7. Finally, high-resolution spectroscopy was recently utilized to provide a first estimate of the C/O ratio in the atmosphere of HD 179949 b (Chapter 4). The latter parameter is potentially related to the formation history of planets (Öberg et al. 2011) and to the presence of thermal inversion layers in their atmospheres (Madhusudhan 2012).

In this work we focus on the additional capabilities of high-dispersion observations to directly detect the Doppler signature of rotation and atmospheric circulation from a transiting exoplanet. Already Snellen et al. (2010) reported a marginal detection of winds flowing from the day- to the night-side of HD 209458 b, deduced from the measured  $(-2 \pm 1)$  km s<sup>-1</sup> blue-shift in the total cross-correlation signal. This result was further discussed by Miller-Ricci Kempton & Rauscher (2012) and Showman et al. (2013), who linked the theoretical expectations based on atmospheric circulation models to the observable Doppler signature at high spectral resolution. It is worth noting that the alternative interpretation of the  $-2$  km s<sup>-1</sup> shift as due to

orbital eccentricity (Montalto et al. 2011) is excluded by the latest refinement of the planet orbital parameters (Crossfield et al. 2012; Showman et al. 2013).

Giant exoplanets orbiting very close to their parent star (hot Jupiters) are thought to become tidally locked on timescales of 0.1-100 Myr (Rasio et al. 1996; Marcy et al. 1997), much shorter than the typical age of the observed systems. This configuration leads to extreme temperature contrasts between the permanently illuminated hemisphere and the night-side. The presence of an atmosphere can partially mitigate the temperature contrast, by recirculating the incident stellar energy from the day- to the night-side through winds. It is arguably important to model and observationally constrain the mechanisms driving the energy redistribution, as they have an impact on the global energy balance of exoplanets.

One common outcome of both numerical (e.g., Showman et al. 2009; Rauscher & Menou 2010; Heng et al. 2011) and analytical (Showman & Polvani 2011) simulations is that relatively deep in the planet atmosphere (at pressures of  $\sim 1$  bar) giant planets develop equatorial jet winds streaming eastward (e.g., following the planet rotation). Since those pressures are representative of the planet photosphere and therefore of the broad-band planet thermal emission, this deep circulation shifts the hottest point in the planet atmosphere away from the sub-stellar point. Higher-up in the atmosphere (at pressure of  $\sim 1$  mbar), the dominant wind pattern leads to a global flow from the day side to the night side, crossing the planet terminator at all latitudes. Enriching this basic picture, high-altitude winds can be damped by magnetic drag due to the interaction of the partially-ionized atmosphere with a possible planetary magnetic field (e.g., Perna et al. 2010). As a consequence, wind speeds and the relative importance of equatorial jets and global day- to night-side circulation are expected to vary broadly from planet to planet. Finally, the atmosphere and the planet interior not always reach perfect synchronization due to tidal effects (Showman & Guillot 2002), meaning that global atmospheric super-rotation or sub-rotation are also possible.

Observational constraints on the energy recirculation of hot-Jupiter atmospheres have been placed by broadband observations of secondary eclipses and thermal phase curves (see Cowan & Agol 2011, for a review). Some work indeed confirms the presence of eastward displacements in the maximum of the thermal emission (Crossfield et al. 2010; Knutson et al. 2012), which is in line with the above theoretical predictions. Other work either lacks the continuous phase coverage for assessing such a trend (Harrington et al. 2006; Cowan et al. 2007), or show no evidence for a displacement (Knutson et al. 2009a; Crossfield et al. 2012).

Here we search for the Doppler signature of atmospheric circulation in the high-resolution transmission spectrum of HD 189733 b (Bouchy et al. 2005). This is one of the best-studied exoplanets to date, thanks to the apparent brightness of the host star ( $K = 5.54$  mag). This richness of information translates into observational evidence for rather unique features, such as atmospheric escape (Lecavelier Des Etangs et al. 2010; Jensen et al. 2012) and the prominence of haze (Pont et al. 2008; Sing et al. 2011), masking most of the spectral features in the optical transmission spectrum, except for atomic sodium (Redfield et al. 2008; Huitson et al. 2012).

This planet also has tight constraints on energy recirculation and day/night side

contrasts from multi-wavelength infrared phase curves (Knutson et al. 2007, 2009b, 2012). One of the most distinctive features of the phase curve is a displacement of the planet hot-spot towards the east, and a low day to night side temperature contrast at shorter infrared wavelengths, indicating an efficient heat recirculation between the two hemispheres.

Molecular detections in the near-infrared spectra of HD 189733 b were subject to a strong debate (Swain et al. 2008, 2010; Gibson et al. 2011; Mandell et al. 2011), mostly related to the reliability of HST/NICMOS observations and to the functional form chosen to correct for systematic effects. Presently, low-resolution observations repeated at different times and with different instruments point towards the presence of water and possibly carbon monoxide (Barman 2007; Beaulieu et al. 2008; Charbonneau et al. 2008; Désert et al. 2009). At high-resolution, detections of carbon monoxide in the *K*-band (de Kok et al. 2013) and H<sub>2</sub>O in the *L*-band (Birkby et al. 2013) were reported from dayside observations.

In this work we analyze near-infrared, high-resolution spectra of HD 189733 b observed just before, during, and after the planet transit. Beside searching for the planet absorption lines due to CO, CO<sub>2</sub>, H<sub>2</sub>O, and CH<sub>4</sub>, we aim to detect the spectroscopic signatures of rotation and atmospheric circulation. In Section 6.2 we describe the telescope, instrument, and observations. In Section 6.3 we present our data analysis, with a particular focus on the subtraction of the stellar spectrum. In Section 6.4 we illustrate how the models for the planet atmosphere are computed and the signal is extracted. Finally, the detected signal is presented in Section 6.5 and discussed in Section 6.6.

## 6.2 Observations

We observed two transits of HD 189733 b with the Cryogenic Infra-Red Echelle Spectrograph (CRIRES, Kaeufl et al. 2004) at the ESO Very Large Telescope (VLT) facility. The spectrograph is mounted at the Nasmyth-A focus of the Antu Unit. We opted for the highest available spectral resolution ( $R = 100,000$ ) by observing through the  $0.2''$  slit, and we selected the standard wavelength setting with  $\lambda_{\text{ref}} = 2325.2$  nm, approximately covering the range 2287.5-2345.4 nm. The spectra are imaged on four detectors having  $1024 \times 512$  pixels in the spectral and spatial direction respectively. Gaps of  $\sim 100$  pixel are present in the spectral direction due to the physical separation of each detector. The throughput of CRIRES was maximized by observing in conjunction with the Multi Application Curvature Adaptive Optic system (MACAO, Arsenault et al. 2003). For accurate background subtraction, the spectra were taken by nodding  $10''$  along the slit with no jitter, according to an ABBA sequence.

The first transit was observed as part of the Large Program 186.C-0289 on July 21, 2011. The observations started at 2:15 UT with a seeing above  $2''$ . Due to strong wind from the north, pointing restrictions were applied between 4:05 UT and 5:55 UT, resulting in a gap in the data. When the observations were restarted, the wind maintained steady just below the pointing limit of  $12 \text{ m s}^{-1}$ , but the seeing gradually improved and reached  $1.2''$  at the end of the observations ( $\sim 8:00$  UT). We chose an exposure time of 120 second per spectra, resulting in 20 pairs of AB or BA spectra

observed before pointing restrictions (corresponding to orbital phases  $\varphi = 0.971-0.004$ ), and 19 pairs in the second part of the night ( $\varphi = 0.041-0.069$ ), well after the last contact of the stellar and the planet disks ( $\varphi = 0.017$ ). As a consequence, only 13 of the 39 spectra were taken during transit, and in bad-seeing conditions, resulting in degraded performances of the adaptive optics system.

The second transit of HD 189733 b was observed with the DDT proposal 289.C-5030 on July 30, 2012. The observations started at 1:10 UT and were stopped at 3:14 UT again due to pointing restrictions, corresponding to a range in orbital phase 0.977-0.017. This was sufficient to observe a full transit of the planet. The first spectra were taken at airmass greater than 2 with a 1.2-1.4'' seeing. At 1:22 UT the seeing abruptly dropped below 1'', resulting in significantly higher signal-to-noise ratio due to better performances of the AO system. With 60 seconds of exposure time per spectrum, we collected 45 pairs of AB or BA spectra, of which 39 during the transit of HD 189733 b.

## 6.3 Data analysis

### 6.3.1 Extraction of the one-dimensional spectra

We utilized the CRIFES pipeline version 2.1.3 for the basic calibration and the extraction of the one-dimensional spectra. On each frame, dark-subtraction and flat-field correction were performed by utilizing the standard calibration frames observed the morning after each night. An additional non-linearity correction was applied on the science and calibration frames by using the appropriate set of archival data. Each pair of AB or BA frames was subsequently combined in order to subtract the background, and the one-dimensional spectrum was obtained by optimal extraction (Horne 1986).

The remainder of the data analysis was performed via custom-built procedures in IDL. For each of the CRIFES detectors, the data was organized in two-dimensional arrays containing pixel number (wavelength) and frame number (time/phase) on the horizontal and vertical axes, respectively.

### 6.3.2 Correction of bad-pixels and odd-even effect

Bad-pixels due to cosmic rays and detector cosmetics were corrected as in Chapter 4, by spline interpolating across isolated pixels or bad columns in the data matrix, by linearly interpolating across 2-3 consecutive bad pixels in the spectral direction, and by masking larger groups of bad pixels.

In this work we also corrected for a residual odd-even effect, which is known to affect detector #4 even after the application of calibration frames (see Figure 6.1). It is due to a differential gain between the odd and the even columns of the detector, which is dependent on the pixel position in the array. For each of the spectra on detector #4, we selected the 512 odd and 512 even pixels, and we interpolated them to the full range of 1024 pixels. The ratio of the odd and even interpolated spectra gave us the scaling factor to apply to the even pixels as a function of pixel number

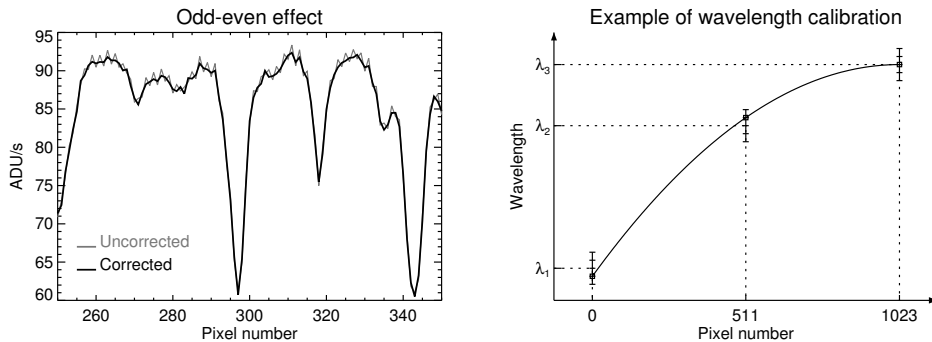


Figure 6.1: Two stages of the data analysis. *Left panel*: correction of a residual odd-even effect in CRIRES detector #4. The grey solid line shows a small portion of one of the 45 spectra observed on July 30, 2012. The solid black line shows the same spectrum after correction. *Right panel*: algorithm for wavelength calibration. A grid of 5 point is constructed around a triplet of trial wavelength values ( $\lambda_1, \lambda_2, \lambda_3$ ). For each grid triplet, the corresponding quadratic fit is computed. The best solution is determined as described in Section 6.3.3 and the triplet of the trial wavelength is updated accordingly. The final solution is found iteratively, by refining the grid step by a factor of 5 at each iteration.

$x$ . We linearly fitted the (pixel, scaling) with three different slopes for  $0 < x < 40$ ,  $40 < x < 511$ , and  $512 < x < 1023$ . These boundaries were found by minimizing the r.m.s. of the corrected spectrum, which was obtained by multiplying the even pixel by the fitted scaling factor. An example of the corrected spectra is shown in the left panel of Figure 6.1 by the black solid line.

### 6.3.3 Alignment of spectra and wavelength calibration

To be able to implement our strategy for removing telluric absorption (see Section 6.3.5), the spectra need to be aligned to a common wavelength scale. In Chapters 2-4, this task was performed by measuring the centroid position of the telluric lines. The star HD 189733 shows absorption lines in the observed wavelength range, subject to a changing Doppler shift due to the changing barycentric velocity of the observer and the stellar radial velocity. Moreover, the line shapes change during transit due to the Rossiter-McLaughlin effect. Since these effects could potentially impact the centroid determination, in this work we did not measure the centroids of telluric lines, but we utilized the cross correlation between the data and a template spectrum to align and determine the wavelength solution of the data.

We first computed a telluric template spectrum via ATRAN<sup>1</sup> for 1.5 mm of precipitable water vapor, the altitude of Cerro Paranal, and a zenith distance of 30 degrees. We verified that the precise tuning of these parameters has a negligible effect on the cross correlation. Subsequently, we computed a stellar template for

<sup>1</sup><https://atran.sofia.usra.edu/>

each of the spectra based on the position, amplitude, and line profile of the stellar CO lines (determined as in Section 6.3.4), and doppler-shifted by the stellar radial velocity. For each observed spectrum, the global template spectrum was obtained by summing the telluric and stellar template constructed as above.

We determined the wavelength solution of each spectrum and each detector by calculating a grid of trial quadratic solutions, which is appropriate for CRIRES data<sup>2</sup>. As shown in the right panel of Figure 6.1, each quadratic solution is given by the parabola passing through the wavelengths of the first, middle, and last pixels of the detector ( $\lambda_1, \lambda_2, \lambda_3$ ). The starting values were given by the default (pixel, wavelength) solution of the CRIRES pipeline. A grid of 5 elements was then constructed around each  $\lambda_i$ , in steps of 0.2 nm. Each of the resulting 125 grid points defines a trial wavelength solution for the data, to which we interpolated the global template. We then computed the cross correlation with the data, selected the best solution based on the highest cross-correlation, and updated the triplet of wavelengths ( $\lambda_1, \lambda_2, \lambda_3$ ). We refined the step size by a factor of 5 (to 0.04 nm) and repeated the computation. After 4 iterations, we adopted the best-fitting solution as wavelength solution for our spectrum. In principle, this gives us a precision of  $3.2 \times 10^{-4}$  nm (0.03 pixels) in the wavelength solution.

We finally aligned all spectra to a common wavelength scale, which we computed by averaging the (pixel, wavelength) solutions of all spectra. The alignment was performed by spline-interpolating each spectrum to the new wavelength scale.

### 6.3.4 Removal of the stellar spectrum

During a large portion of the transit, star and the planet have a similar radial velocity (to within few  $\text{km s}^{-1}$ ), meaning that spectral features present in both the stellar and the planet spectrum are almost superimposed. This is the case of the CO ladder around  $2.3 \mu\text{m}$ , which is a distinctive feature of both the planet and the stellar spectrum. Stellar CO lines have depths of  $\sim 10\%$  with respect to the continuum, while the typical depth of the planet spectral lines is expected to be 50-100 times smaller.

The stellar spectrum cannot be normalized in the same way as the telluric spectrum (see Section 6.3.5), because the star is not completely stationary in wavelength. As mentioned above, the barycentric velocity of the observer and the stellar radial velocity both change during the night, overall by  $0.5\text{-}1 \text{ km s}^{-1}$ . Moreover, the stellar line profiles are distorted by the Rossiter-McLaughlin effect during transit. The non-stationary nature of the stellar spectrum produces residual time-correlated noise, which is amplified by the cross correlation. As a result, we measure spurious cross-correlation signals at orbital velocities different from that of HD 189733 b, but strong enough to partially contaminate the planet signal, as shown in Figure 6.6. Although this contamination does not affect possible signals from  $\text{H}_2\text{O}$ ,  $\text{CH}_4$ , and  $\text{CO}_2$ , we expect CO to have an important contribution to the planet spectrum as well, based on previous high-resolution dayside observations of HD 189733 b (de Kok et al.

<sup>2</sup>See the CRIRES manual at <http://www.eso.org/sci/facilities/paranal/instruments/crides/doc.html>

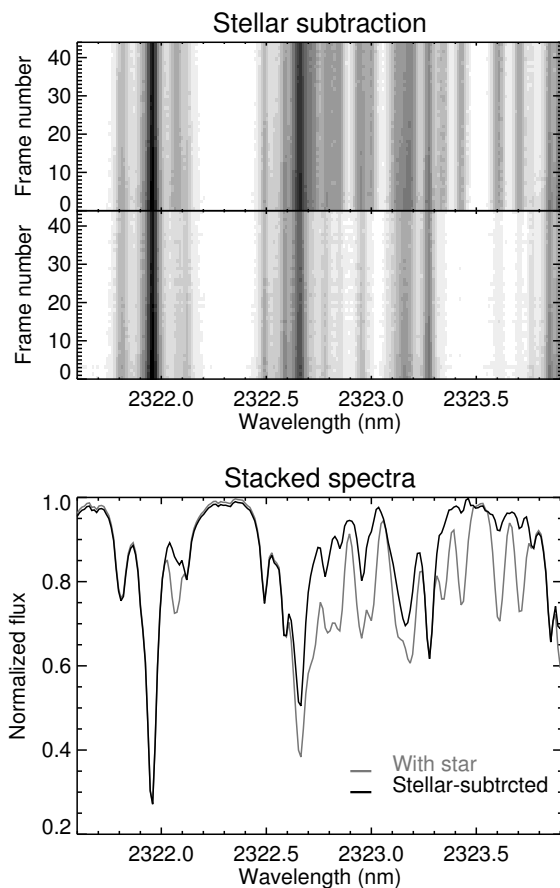


Figure 6.2: Removal of the spectrum of the star HD 189733. *Top panel:* comparison between the original spectral series and the stellar-subtracted spectra, based on the analysis presented in Section 6.3.4. *Bottom panel:* co-added spectral series before (grey line) and after (black line) stellar subtraction.

2013). Therefore, we modeled and subtracted the stellar spectrum in order to avoid spurious cross-correlation signal.

The details of the stellar removal are provided in Appendix 6.A, while an example of the final result is provided in Figure 6.2.

### 6.3.5 Removal of telluric lines

Due to the fact that telluric lines change in depth during the observations but not in position, the telluric spectrum is removed by modeling the flux of each data column (e.g., each wavelength element) in time. In Chapters 2-4, we have fitted the data by geometric airmass, which is the main cause of telluric variations, and then removed residual noise by sampling it directly from the data. In this case, the planet absorption lines can have depths up to  $10^{-3}$  in relative flux, which is approximately

one order of magnitude larger than in a typical dayside spectrum. This makes the planet signal comparable to the typical noise level per spectrum, meaning that a blind removal of systematics might partially wash out the planet signal as well.

We therefore adopted the `SYSTEM` algorithm for de-trending the data (Tamuz et al. 2005; Mazeh et al. 2007), based on the implementation by Birkby et al. (2013). This has the advantage that we can weight the data by their noise, and we can test the impact of the algorithm on artificially-injected planet signal (see Section 6.5.3) in order to determine the desired number of iterations. The ability of weighting by the noise made us prefer the use of `SYSTEM` over Principal Component Analysis, which has also been used in past high-dispersion observations (de Kok et al. 2013).

## 6.4 Modeling and extracting the planet signal

After removing the stellar and telluric lines as explained in Sections 6.3.4 and 6.3.5, we extracted the planet signal by cross-correlating the data with model spectra for the planet atmosphere. In this way we combined all the spectral lines of the planet in a single cross-correlation function (CCF), increasing the signal by a factor of  $\sqrt{N}$ , where  $N$  is the number of strong molecular lines.

We computed the cross correlation with both *narrow* and *broadened* atmospheric models. The former are the output of our radiative transfer calculations described in Section 6.4.1, which do not account for atmospheric circulation or instrumental broadening. The latter are the narrow models convolved with the broadening profiles described in Section 6.4.2.

### 6.4.1 Modeling the planet spectra

The transmission spectrum of HD 189733 b was modeled by following the same prescriptions of Chapter 4 concerning the choice of line lists, line profiles, and collision-induced absorption by hydrogen. We described the terminator atmosphere of the planet by assuming an average temperature-pressure ( $T/p$ ) profile parametrized in order to match the Madhusudhan & Seager (2009) profiles in the lower part of the atmosphere, and with the simplest possible sampling. For  $p > 1$  bar, an isothermal atmosphere at temperature 1750 K was adopted. Between 1 and 0.1 bar, we made the temperature decrease to 1350 K. In the range  $-2.5 < \log(p) < -1.0$ , we tested two opposite profiles, by making the temperature  $T_2$  either increase to 1500 K or decrease to 500 K. For lower pressures (higher altitude), we chose an isothermal atmosphere at temperature  $T_2$ , extending up to  $p = 10^{-10}$  bar. Note that  $T_2 = 1500$  K corresponds to a temperature inversion, which is included in these models reflecting our very limited knowledge of the upper atmosphere of this planet. However, the inversion is so weak and so high in the atmosphere that it does not affect dayside spectra (i.e., it would not produce emission lines in the spectra).

We computed planet transmission spectra by mixing four trace gases expected to be spectroscopically active in the observed wavelength range: CO, H<sub>2</sub>O, CO<sub>2</sub>, and CH<sub>4</sub>. These are also the gases for which detections have been claimed in the literature, although some of them are still under debate (see Section 6.1). We tested molec-



ular Volume Mixing Ratios (VMRs) of  $\text{VMR} = (10^{-5}, 10^{-4}, 10^{-3})$  for carbon monoxide and water vapor, and  $\text{VMR} = (10^{-6}, 10^{-5})$  for carbon dioxide and methane. We also computed models with only CO, only H<sub>2</sub>O, and only CH<sub>4</sub>, in order to assess the individual contribution of each molecule to the total planet signal. CO<sub>2</sub> is expected to produce a spectral signature in detector #1 only, and therefore it was not studied as a single trace gas.

The radiative transfer was performed by computing the optical thickness for 40 altitude points along slant paths through the atmosphere, and then by integrating over altitude and the  $2\pi$  radians of the planet limb to produce the transmission spectrum.

## 6.4.2 Modeling the planet broadening profile

We modeled the broadened planet line profiles by assuming two basic patterns of atmospheric circulation: planet *rotation*, and *equatorial super-rotation*. A global *day-to-night side flow* does not need modeling, as it just produces a blue-shifted cross-correlation signal. We constructed a two-dimensional model for the planet and the star, which is represented in Figure 6.3. We chose the  $x$  and  $y$  directions along and perpendicular to the orbit, respectively. We assigned the coordinates  $(x, y) = (0, 0)$  to the center of the stellar disk and expressed all quantities in units of stellar radius,  $R_S = (0.756 \pm 0.018) R_\odot$  (Torres et al. 2008). The planet was modeled as a disk of radius  $n_P = 50$  pixels. With this choice the step size is  $dx = R_P / (50 R_S) \simeq 0.0031$ , with  $R_P = (1.138 \pm 0.027) R_{\text{Jup}}$  being the planet radius (Torres et al. 2008). Each horizontal slice of the planet disk corresponded to an impact parameter  $b_i$  ranging from  $(b - R_P / R_S)$  to  $(b + R_P / R_S)$ , where  $b = (0.6631 \pm 0.0023)$  is the known impact parameter of HD 189733 b (Agol et al. 2010). The planet center has coordinates  $(x_C, b)$  corresponding to an orbital phase:

$$\varphi(x_C) = \frac{1}{2\pi} \sin^{-1} \left( \frac{x_C}{a} \right), \quad (6.1)$$

where  $a = (8.863 \pm 0.020) R_S$  is the semimajor axis of the orbit (Agol et al. 2010). For each  $b_i$ , the intensity of the stellar chord crossed by the planet during transit was modeled by assuming a quadratic limb-darkening law:

$$I(\mu) = 1 - u_1(1 - \mu) - u_2(1 - \mu)^2, \quad (6.2)$$

with  $\mu$  being the cosine of the angle between the line of sight and the normal to the stellar surface, and  $u_1 = 0.077, u_2 = 0.311$  the limb-darkening coefficients appropriate for a star with  $T_{\text{eff}} = 5000$  K,  $\log g = 4.5 \text{ cm s}^{-2}$ , and solar metallicity, observed in the K-band (Claret & Bloemen 2011). Given the geometry of our problem, Equation 6.2 can be expressed as function of  $(x, b_i)$  through the following:

$$\mu = \sqrt{1 - x^2 - b_i^2}. \quad (6.3)$$

Equation 6.3 is valid for  $-\bar{x}_i < x < \bar{x}_i$ , with  $\bar{x}_i$  being the coordinate of the edge of the stellar disk:

$$\bar{x}_i = \sqrt{1 - b_i^2}. \quad (6.4)$$

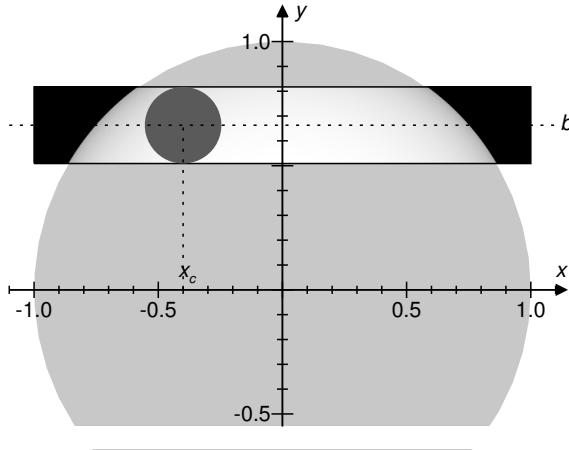


Figure 6.3: Basic geometry of the model utilized for computing the planet broadening profiles. All quantities are expressed in units of stellar radius. The intensities of 100 slices of the stellar disk, corresponding to impact parameters between  $b - R_P/R_S$  and  $b + R_P/R_S$  (the boxed area in the figure), are computed based on a quadratic limb-darkening law (Equation 6.2). The planet, centered in  $(x_c, b)$ , is shifted along the  $x$  direction pixel by pixel. At each position, the light curve is computed as explained in Section 6.4.2

The stellar intensity  $\mathcal{S}_i(x)$  for the slice  $i$  is therefore:

$$\mathcal{S}_i(x) = \begin{cases} I(x, b_i) & \text{for } |x| \leq \bar{x}_i \\ 0 & \text{elsewhere.} \end{cases} \quad (6.5)$$

At the edges of the stellar and planet profiles, sub-pixel approximation is taken into account by multiplying each pixel values by their fractional occupancy.

To test the model, we initially assumed a completely opaque planet disk (0 pixel values). The transit light curve was computed by shifting the planet array one pixel at a time along the  $x$  direction, in the range  $-1.2 < x_c < 1.2$ . At each position, the planet and stellar arrays were multiplied and summed across all pixels in order to obtain the flux. Finally, the light curve is normalized by the total stellar intensity  $I_{\text{tot}}$ , which we computed analytically via the following integral:

$$I_{\text{tot}} = \int_0^{2\pi} \int_0^{n_S} I(r)r \, dr \, d\theta = 2\pi \int_0^{n_S} I(r)r \, dr, \quad (6.6)$$

where  $n_S = 1/dx$  is the number of pixels corresponding to one stellar radius. In the above we have used polar coordinates  $(r, \theta)$  with origin in the center of the stellar disk. Consequently,  $\mu = \sqrt{1 - (r/n_S)^2}$ , which leads to

$$I_{\text{tot}} = \pi \left(1 - \frac{u_1}{3} - \frac{u_2}{6}\right) n_S^2 \simeq 3.026 \times 10^5. \quad (6.7)$$

Our normalized light curve is in agreement with the Mandel & Agol (2002) models at the  $3.5 \times 10^{-5}$  level in relative flux.

We modeled a planet atmospheric ring with the same radius as the planet and with a thickness of 1 pixel. This corresponds to  $\sim 1600$  km in physical units, matching the 5-10 scale heights typically probed by transmission spectroscopy (Madhusudhan et al. 2014). We assigned to each pixel of the ring a velocity consistent with a rigid-body rotation along an axis perpendicular to the orbital plane:

$$v_{\text{ring}} = \frac{2\pi x R_S}{P_{\text{rot}}}, \quad (6.8)$$

where  $P_{\text{rot}}$  is the planet rotational period. An additional equatorial super-rotation is introduced by adding (or subtracting) a wind speed  $v_{\text{eq}}$  to the receding (or approaching) pixels of the planet ring within  $25^\circ$  of latitude.

Given the above velocity field  $v_{\text{ring}}$ , each pixel  $(x_i, b_j)$  of the planet ring contributes to the planet line profile with a Gaussian profile given by:

$$\mathcal{G}(\vec{v}, x_i, b_j) = \mathcal{S}(x_i, b_j) \exp \left\{ -\frac{1}{2} \frac{[\vec{v} - v_{\text{ring}}(x_i)]^2}{\sigma^2} \right\} \quad (6.9)$$

where the width  $\sigma$  is given by

$$\sigma \equiv \frac{\text{FWHM}_{\text{CRIRES}}}{2\sqrt{2\log 2}} \simeq 1.27 \text{ km s}^{-1}, \quad (6.10)$$

where the FWHM of CRIRES is supposed to be constant and equal to  $3 \text{ km s}^{-1}$ .

An example of the modeled line profiles as a function of orbital phase is provided in Figure 6.4, for  $P_{\text{rot}} = 2.217$  days. Distinctive features are the flattened peak at mid-transit, which eventually splits into two separate components in case of fast rotation, and the overall red-shift (or blue-shift) of the peak during ingress (or egress).

### 6.4.3 Cross correlation and signal retrieval

For each of the CRIRES detectors, we cross correlated the observed spectra with each the model spectra described in Section 6.4.1, Doppler shifted according to a lag vector of radial velocities in the range  $\pm 250 \text{ km s}^{-1}$ , in steps of  $1.5 \text{ km s}^{-1}$ , and convolved with the line profiles computed in Section 6.4.2. We also computed the cross correlation with narrow (unconvolved) model spectra for comparison. As a result, we obtained the cross-correlation signal as a function of planet radial velocity and time,  $\text{CCF}(V_p, t)$ . The total cross correlation is then computed by summing the CCFs in time according to the following. The planet orbital velocity is computed from the known orbital period of  $P = 2.21857567(15)$  days (Agol et al. 2010), the stellar mass of  $M_S = (0.806 \pm 0.048) M_\odot$  and the planet mass of  $M_P = (1.144 \pm 0.056) M_{\text{Jup}}$  (Torres et al. 2008) by using Kepler's Third Law:

$$v_{\text{orb}} = \left[ \frac{2\pi G M_S}{P(1 - M_P/M_S)^2} \right]^{1/3} \quad (6.11)$$

Since the orbital inclination of HD 189733 b is  $i = (85.710 \pm 0.024)$  deg (Torres et al. 2008), the planet projected planet orbital velocity is:

$$K_P = v_{\text{orb}} \sin i = (151.3 \pm 10.2) \text{ km s}^{-1} \quad (6.12)$$

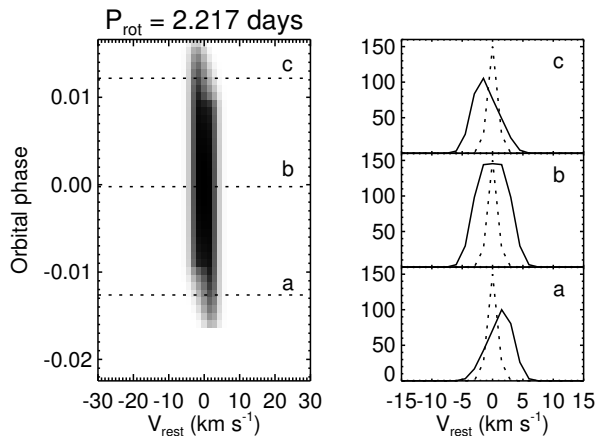


Figure 6.4: *Left panel*: planet broadening profiles computed for a rotational period of 2.217 days, as a function of orbital phase. *Right panel*: cuts of the broadening profiles during ingress (panel *a*), at mid-transit (panel *b*), and during egress (panel *c*). For comparison, the instrument profile of CRIRES is shown with a dotted line.

The measured planet orbital velocity is therefore:

$$v_P(t) = K_P \sin[2\pi\varphi(t)] + v_{\text{sys}} + v_{\text{helio}}(t) \quad (6.13)$$

where  $v_{\text{sys}} = (-2.57 \pm 0.14) \text{ km s}^{-1}$  is the known systemic velocity of HD 189733 (Chubak et al. 2012), and  $v_{\text{helio}}$  is the heliocentric velocity of the observer, computed through the IDL routine `heliocentric.pro`, and  $\varphi(t)$  is the planet orbital phase computed by taking the fractional part of

$$\varphi(t) = \frac{t - T_0}{P}, \quad (6.14)$$

where  $t$  and  $T_0 = 54,279.436714(15)$  are the reduced HJD of our spectra and of mid-transit (Agol et al. 2010), respectively. For each CRIRES detector, the individual CCFs are weighted by the S/N of the corresponding spectrum, as measured before removing the telluric lines. Consequently, the CCFs are shifted to the planet rest frame by linear interpolation, according to Equation 6.13, and summed in time. Finally, the total CCF of the four detector are summed with a weight corresponding to the expected planet signal (see Section 6.5.3). Even though for this planet we know the planet projected orbital velocity with much better accuracy than these measurements require, we also computed the total cross-correlation signal for  $K_P$  in the range  $0\text{-}180 \text{ km s}^{-1}$ , in steps of  $2 \text{ km s}^{-1}$ , as done in Chapters 2-4 for non-transiting planets. This allows us to 1) prove the absence of spurious signals away from the expected position, and 2) investigate possible cross-correlation noise due to stellar residuals.

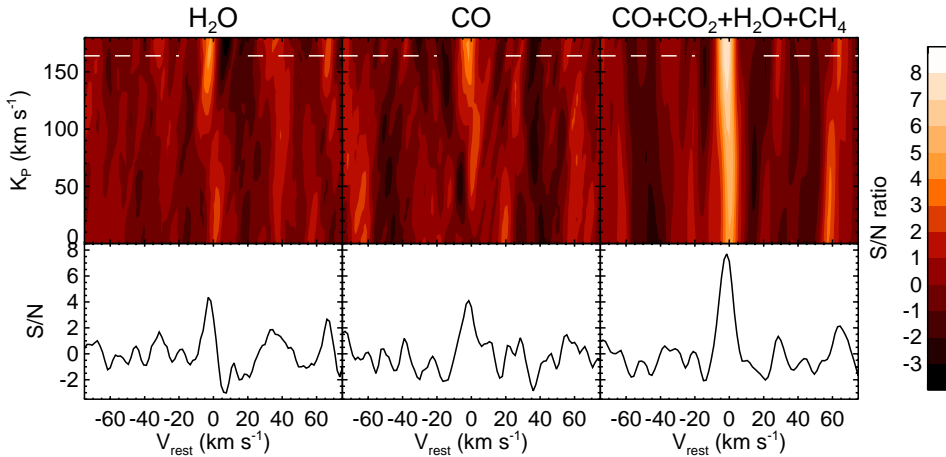


Figure 6.5: Total signal from the transmission spectrum of HD 189733 b obtained by cross-correlating with model containing  $\text{H}_2\text{O}$  only (left panels),  $\text{CO}$  only (mid panels), and a combination of  $\text{CO}$ ,  $\text{CO}_2$ ,  $\text{H}_2\text{O}$ , and  $\text{CH}_4$ . The top panels show the S/N as a function of planet rest-frame velocity  $V_{\text{rest}}$  and projected orbital velocity  $K_p$ . The bottom panels show a cut at  $K_p = 166 \text{ km s}^{-1}$ , which is where the measured signal is maximized.

## 6.5 Results

### 6.5.1 Planet signal from models with single trace gases

We first cross correlated with models containing a single trace gas, including water vapor, carbon monoxide, and methane. For  $\text{H}_2\text{O}$  and  $\text{CH}_4$ , there is no contamination from correlation noise due to stellar residuals, so these species should give the most robust results, if detected. As explained in Section 6.1, water vapor is thought to be present in the atmosphere of HD 189733 b from previous studies (Barman 2007; Beaulieu et al. 2008; Charbonneau et al. 2008; Désert et al. 2009). We indeed measure a signal from  $\text{H}_2\text{O}$  at a signal-to-noise of  $S/N = 4.5$ , by cross correlating with broadened line profiles corresponding to a planet rotational period of  $P_{\text{rot}} = 2.2$  days. For comparison, by cross correlating with a narrow profile we would only obtain a tentative detection with a  $S/N \simeq 2.8\text{-}3.0$ . The S/N is measured by dividing the peak value in the  $(K_p, V_{\text{rest}})$  matrix by the standard deviation of the noise. The signal does not increase if we add an equatorial super-rotation to the model, meaning that we see no evidence for extra atmospheric circulation based on the water vapor signal. Moreover, the highest S/N is obtained when including both in-transit and out-of-transit spectra. The implications of this are discussed in Section 6.6, and are potentially related to the contribution from the planet night side.

A particular care must be observed in studying the cross-correlation signal using template models containing only carbon monoxide. As we highlighted already in Section 6.3.4, the stellar spectrum contains  $\text{CO}$  lines as well, and it is capable to create spurious cross-correlation signal masking the planet signal. This is illustrated

by the left panel of Figure 6.6, which shows the result of the cross-correlation with CO models when the star is not removed. A strong spurious signal due to the star is detected at  $K_P = 50\text{-}100 \text{ km s}^{-1}$ . Differently from Chapter 3, in this case the stellar noise does not peak at  $K_P = 0 \text{ km s}^{-1}$ . This is likely a result of the Rossiter-McLaughlin effect, as the stellar line profiles are distorted by the planet disk crossing the rotating stellar surface. This provokes missing flux in the blue-shifted line wing during ingress, and in the red-shifted line wing during egress, effectively mimicking the Doppler signature of the planet transmission spectrum. The right panel of Figure 6.6 shows the results of subtracting the stellar spectrum as explained in Section 6.3.4. A planet signal is detected with  $S/N = 4.1$ , using a line broadening that corresponds to the same rotational period as for the  $\text{H}_2\text{O}$  signal (2.2 days). If a narrow profile is utilized, the  $S/N$  decreases to 3.1, in line with the  $\text{H}_2\text{O}$  result.

Finally, we do not detect any signal from  $\text{CH}_4$  alone above  $S/N = 2.8$ , independently from the broadening profile applied.

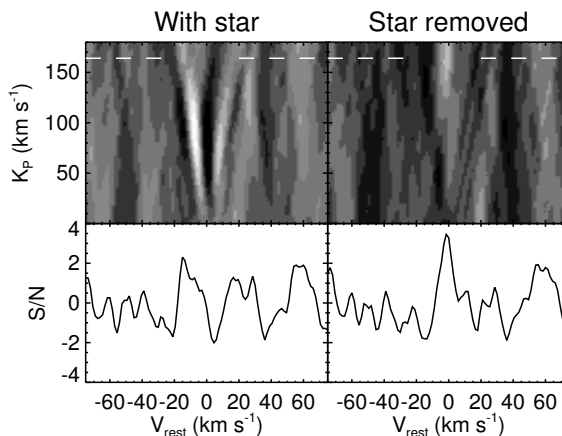


Figure 6.6: Planet signal from models containing CO alone. The left panels show the result of the analysis prior to the removal of the stellar spectrum, the right panels after the stellar subtraction. Top and bottom panels are the same as in Figure 6.5, and the grey scale runs from  $-3$  to  $6$  in  $S/N$ , in linear steps. A planet signal at  $S/N = 4.1$  appears when removing the stellar spectrum as explained in Section 6.3.4.

## 6.5.2 Planet signal from models with all molecular species

We obtain the maximum signal from the transmission spectrum of HD 189733 b when cross-correlating with a template containing  $\log_{10}(\text{VMR}) = (-4, -4, -7, -5)$  for  $\text{H}_2\text{O}$ ,  $\text{CO}$ ,  $\text{CH}_4$ , and  $\text{CO}_2$  respectively, and for an upper atmospheric temperature of  $T_2 = 1500 \text{ K}$ . This model results in a  $S/N = 7.9$ , measured at a planet projected orbital velocity of  $K_P = 168^{+13}_{-20} \text{ km s}^{-1}$  and rest-frame velocity of  $V_{\text{rest}} = -1.35^{+1.3}_{-1.5} \text{ km s}^{-1}$ . These are fully consistent with the known projected orbital velocity of the planet,  $K_P = (151.3 \pm 10.2) \text{ km s}^{-1}$  (Equation 6.12), and with no global

day-to-night side winds. We note that the large uncertainty in  $K_P$  with respect to previous dayside observations at high spectral resolution (Chapters 2-4) is due to the small portion of the planet orbit covered with transit measurements. Furthermore, in the case of HD 189733 b, 2/3 of the transit are spent in ingress/egress, meaning that the spectra in which the planet signal deviates the most from zero radial velocity have the lowest weighting, which further increases the uncertainties. Therefore, in order to obtain the best estimate of  $K_P$ , we indeed utilize the in-transit spectra, but we assign to them equal weighting. In this way the marginal loss of S/N is compensated by a better localization of the planet signal in the  $(K_P, V_{\text{rest}})$  plane.

The planet signal is only detected at  $S/N = 4.2$  when cross-correlating with a narrow model template. A highly-significant increase of the S/N is obtained when convolving the template with rotationally-broadened planet line profiles, for rotational periods ( $P_{\text{rot}}$ ) longer than 1.2 days and shorter than 5.0 days ( $1\sigma$ ), with the maximum S/N detected for  $P_{\text{rot}} = 1.9\text{-}2.2$  days, synchronous with the orbital period. These results are shown in Figure 6.7.

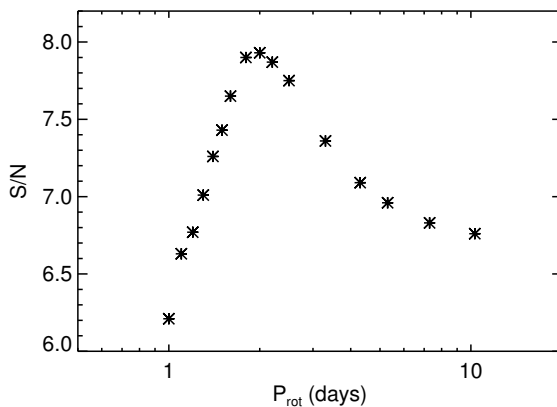


Figure 6.7: Planet signal from our best-fitting model (see Section 6.5.2), as function of the planet rotational period  $P_{\text{rot}}$  utilized for computing the broadened line profiles as in Section 6.4.2. It shows that the maximum S/N is reached for  $P_{\text{rot}} = 1.9\text{-}2.2$  days, consistent with a tidally-locked planet.

In Chapters 2-4, it has been pointed out that high-resolution observations alone cannot constrain absolute abundances, because the information about absolute fluxes is lost during the data analysis. However, relative molecular abundances can be constrained and utilized to estimate the atmospheric C/O ratio. We have conducted such analysis for HD 189733 b, obtaining the results presented in Figure 6.8. Independently from the temperature assumed for the upper atmosphere, our analysis points towards an oxygen-rich planet, with a best-fitting value of  $C/O = (0.5 \pm 0.4)$  ( $2\sigma$  error bars).

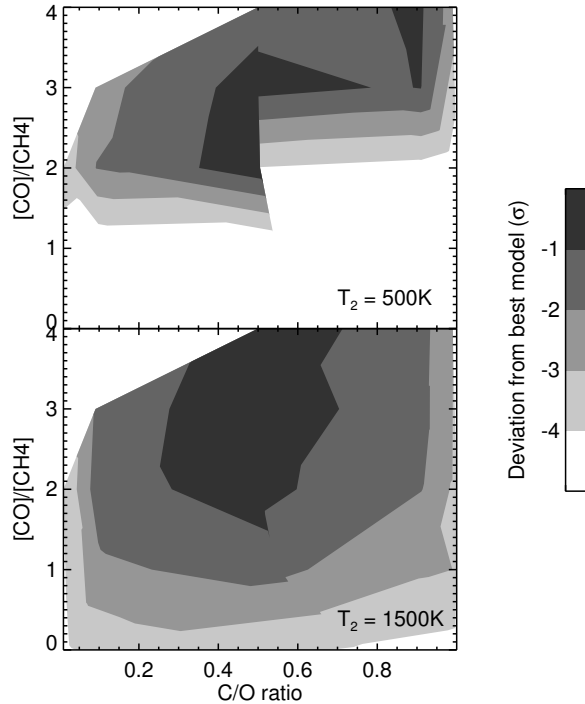


Figure 6.8: Statistical deviation from the best-fitting model for the atmosphere of HD 189733 b at terminator, as a function of C/O ratio. The top and bottom panels show the results for an upper atmospheric temperature of 1500 K and 500 K, respectively. Our analysis clearly points towards an oxygen-rich atmosphere for this exoplanet.

### 6.5.3 Impact of SYSREM algorithm on the measured signal

We tested the SYSREM algorithm with a number of iterations ranging from 2 to 15. The first iterations only remove the major trends (i.e., instrument throughput and airmass), leaving most of the correlated noise in the core of telluric lines. Many iterations effectively remove systematic trends, but also potentially weaken the planet signal by treating it as time-correlated noise. The outcome of these tests is presented in Figure 6.9.

We initially injected an artificial planet signal in the data before stellar subtraction, and we performed the subsequent data analysis and signal retrieval. We consequently measured the signal in each of the CRIRES detectors and determined their corresponding weighting. The left panel of Figure 6.9 shows the strength of the retrieved signal normalized to the maximum value. In addition, the contribution of each of the CRIRES detectors is indicated by the grey-shaded regions, with dark to light grey representing detectors #1 to #4. We tested three representative models for the planet atmosphere, containing H<sub>2</sub>O only (top panel), CO only (middle panel),



and the best mixture of the four trace gases indicated in Section 6.5.2 (bottom panel). From these simulations on artificial data, we concluded that 1) each CRIRES detector reacts differently to the application of SYSREM, and 2) the optimal number of iterations seems to be between 8 and 10.

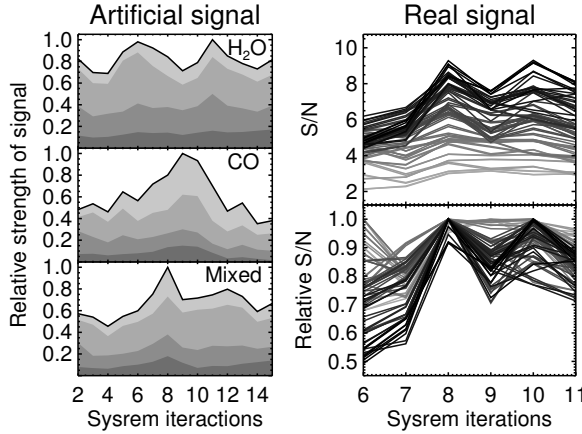


Figure 6.9: Results of the tests conducted on the SYSREM algorithm. *Left panels:* signal retrieved after injecting model transmission spectra of HD 189733 b containing only water (top panel), only CO (middle panel), and four molecular species (CO, CO<sub>2</sub>, H<sub>2</sub>O, and CH<sub>4</sub>) mixed according to the abundances indicated in Section 6.5.2 (bottom panel), as a function of applied iterations of the algorithm. The contribution of each of the CRIRES detectors is indicated by the filled contours, colored from dark to light grey for increasing detector number. *Right panels:* real signal from the transmission spectrum of HD 189733 b, obtained by cross-correlating with the 72 model templates constructed as in Section 6.4.1, as a function of the number of SYSREM iterations. The color coding runs from light gray to black for increasing S/N. The top panel show the total S/N for each of the models, the bottom panel the relative S/N of each model relative to its maximum. As described in Section 6.5.3, these tests suggest that 8 iterations of the algorithm are the most objective choice for our analysis.

We also analyzed the impact of SYSREM on real data, by applying a number of iterations between 6 and 11, and cross correlating with each of the 72 model spectra, as shown in the right panels of Figure 6.9. For each iteration, we measured the highest S/N in a region of the ( $K_p$ ,  $v_{\text{rest}}$ ) diagram centered on the planet signal. In this case, with 8 iterations we obtain the maximum S/N for most of the models (top panel). Even though a higher number of iterations (e.g., 10) can in some cases lead to higher S/N, this choice leads to a much higher spread in the retrieved signal (bottom panel), and therefore does not guarantee an objective criterion for comparing model spectra. Therefore, based on the tests on real and artificial signals, we have applied 8 iterations of SYSREM for this work.

Regarding the weighting of the four CRIRES detectors, our tests on the real signal have been conducted by choosing the weightings in order to maximize the S/N.

Consequently, we have studied the distribution of the weightings for the 72 model spectra and determined an average weighting of [0.45, 0.07, 0.35, 0.15] for the four detectors, which we have utilized for obtaining the total cross-correlation signal as explained in Section 6.4.3.

#### 6.5.4 Absence of signal in the partially-observed transit

A decrease in the total planet signal is observed when including the spectra from the transit partially observed in the first night. In Section 6.2 we have described the degraded observing conditions during those observations. Overall the instrument resolution, throughput, and the resulting S/N were much lower than during the second night of observations. Moreover, only 13 spectra were observed in transit, compared to the 38 of the second night. Due to these factors alone, we expect from the first night no more than 40-50% of the signal measured during the second transit. In addition, our detrending of the data during telluric removal is most effective when the spectra are observed continuously and without abrupt instrumental or atmospheric changes. In the case of the partially-observed transit, the observations were stopped half way and restarted after  $\sim 1$  hour, leading to different instrumental performances and atmospheric condition before and after pointing restriction, and inducing a big jump in the residual systematics in the data, which cannot be completely detrended via the algorithms utilized for these high-resolution observations. We therefore conclude that this lack of signal in 1/3 of the data is, if not totally justified by the poor instrumental performances, at least consistent with them.

## 6.6 Discussion

By observing a transit of HD 189733 b at high spectral resolution, we were able to detect the absorption signals of CO and H<sub>2</sub>O separately, and the combined signal of CO, CO<sub>2</sub>, H<sub>2</sub>O, and CH<sub>4</sub>. The signal from CO is strongly affected by cross-correlation noise due to stellar absorption, and is consequently detected only when an accurate subtraction of the stellar spectrum is performed. We do not detect any methane absorption above a S/N of 2.8. Carbon dioxide is only expected to contribute to detector #1 of CRIFES and therefore it was not tested as a single trace gas. However, it leads to a marginal increase in the S/N when mixed with the other three molecular species.

While models containing the four trace gases mixed always give a comparable or marginally better S/N when summing the CCFs over the in-transit spectra only, the S/N from H<sub>2</sub>O models increases by  $\sim 1$  when including spectra observed both in transit and out of transit. This might indicate that we receive a non-negligible contribution from the night side of the planet. This possibility has been pointed out by de Kok et al. (2014). They stress that high-resolution observations do not measure continuum levels, but only their contrast with respect to the core of absorption lines. Even though the broad-band flux from the planet night side is much lower than from the day side, the line contrast would still be detectable if the  $T/p$  profile becomes very steep, for example due to the absence of the strong stellar forcing. Phase

curve measurements with the Spitzer/IRAC instrument (Knutson et al. 2007, 2009b, 2012) indicate a decreasing contribution from the planet night side from  $24\ \mu\text{m}$  to  $3.6\ \mu\text{m}$ , so it is unclear whether the contrast at  $2.3\ \mu\text{m}$  would be enough to produce a detectable night-side thermal emission, and more observations are required to confirm our result.

We obtain a higher S/N when cross-correlating with model templates convolved with rotationally-broadened line profiles, with a maximum signal reached for a planet rotational period of  $P_{\text{rot}} = 1.9\text{-}2.2$  days, or  $2.7\text{-}3.1\ \text{km s}^{-1}$ . This indicates that the planet is tidally locked and confirms the theoretical expectations that close-in gaseous planets reach synchronization of the orbital and rotational periods on short timescales. We do not detect any signature of equatorial super-rotation, nor do we measure a significant blue-shift in the total cross-correlation signal, which would have suggested the presence of strong (e.g.,  $5\text{-}10\ \text{km s}^{-1}$ ) global winds flowing from the day to the night side of the planet. The presence of a slower wind pattern cannot be tested yet with these measurements, which are limited to a precision of  $1.3\text{-}1.5\ \text{km s}^{-1}$ . We note that the absence of a detected equatorial super-rotation might seem in contrast with the displacement in the maximum planet thermal emission observed at  $3.6$  and  $4.5\ \mu\text{m}$  (Knutson et al. 2012). However, as explained in Section 6.1, this kind of wind pattern is expected to arise deep in the planet atmosphere, close to the level of the continuum. It might be hard to probe these pressures in transmission spectroscopy, because we look through slanted optical paths at the planet terminator. Moreover, our data analysis is designed to arbitrarily renormalize the continuum of the spectra, potentially affecting the signatures of equatorial super-rotation. Finally, haze could obscure the deepest layers of the planet atmosphere, washing out their Doppler signature. However, the detection of molecular absorption presented here indicates that the haze dominating the optical low-resolution transmission spectrum (Sing et al. 2011) must be at least partially transparent at  $2.3\ \mu\text{m}$  when observed at high spectral resolution.

In conclusion, in this work we have combined all the measurements within reach of current high-dispersion observations. We have shown that these are very effective in reliably identifying molecular species, in estimating their relative abundances, and in translating them into a measurement of the C/O ratio. Moreover, we were able to measure the rotation of a hot Jupiter for the first time, and confirm that tidal synchronization is the most likely scenario for this planet, in line with the expectations.

These measurements will be routinely performed with future Extremely Large Telescopes (ELTs) on a much larger sample, thanks to their superior collective power. Moreover, more stable spectrograph and/or higher spectral resolution will potentially improve the detection of wind patterns, allowing us to directly measure atmospheric dynamics in planet outside our Solar System.

## Bibliography

- Agol, E., Cowan, N. B., Knutson, H. A., et al. 2010, *ApJ*, 721, 1861
- Arsenault, R., Alonso, J., Bonnet, H., et al. 2003, in Society of Photo-Optical Instrumentation Engineers (SPIE) Conference Series, ed. P. L. Wizinowich & D. Bonaccini, Vol. 4839, 174–185
- Barman, T. 2007, *ApJL*, 661, L191
- Beaulieu, J. P., Carey, S., Ribas, I., & Tinetti, G. 2008, *ApJ*, 677, 1343
- Birkby, J. L., de Kok, R. J., Brogi, M., et al. 2013, *MNRAS*, 436, L35
- Bouchy, F., Udry, S., Mayor, M., et al. 2005, *A&A*, 444, L15
- Charbonneau, D., Knutson, H. A., Barman, T., et al. 2008, *ApJ*, 686, 1341
- Chubak, C., Marcy, G., Fischer, D. A., et al. 2012, ArXiv e-prints
- Claret, A. & Bloemen, S. 2011, *A&A*, 529, A75
- Cowan, N. B. & Agol, E. 2011, *ApJ*, 729, 54
- Cowan, N. B., Agol, E., & Charbonneau, D. 2007, *MNRAS*, 379, 641
- Crossfield, I. J. M., Hansen, B. M. S., Harrington, J., et al. 2010, *ApJ*, 723, 1436
- Crossfield, I. J. M., Knutson, H., Fortney, J., et al. 2012, *ApJ*, 752, 81
- de Kok, R. J., Birkby, J., Brogi, M., et al. 2014, *A&A*, 561, A150
- de Kok, R. J., Brogi, M., Snellen, I. A. G., et al. 2013, *A&A*, 554, A82
- Désert, J.-M., Lecavelier des Etangs, A., Hébrard, G., et al. 2009, *ApJ*, 699, 478
- Gibson, N. P., Pont, F., & Aigrain, S. 2011, *MNRAS*, 411, 2199
- Harrington, J., Hansen, B. M., Luszcz, S. H., et al. 2006, *Science*, 314, 623
- Heng, K., Menou, K., & Phillipps, P. J. 2011, *MNRAS*, 413, 2380
- Horne, K. 1986, *PASP*, 98, 609
- Huitson, C. M., Sing, D. K., Vidal-Madjar, A., et al. 2012, *MNRAS*, 422, 2477
- Jensen, A. G., Redfield, S., Endl, M., et al. 2012, *ApJ*, 751, 86
- Kaeufl, H.-U., Ballester, P., Biereichel, P., et al. 2004, in Society of Photo-Optical Instrumentation Engineers (SPIE) Conference Series, ed. A. F. M. Moorwood & M. Iye, Vol. 5492, 1218–1227
- Knutson, H. A., Charbonneau, D., Allen, L. E., et al. 2007, *Nature*, 447, 183
- Knutson, H. A., Charbonneau, D., Cowan, N. B., et al. 2009a, *ApJ*, 703, 769

- Knutson, H. A., Charbonneau, D., Cowan, N. B., et al. 2009b, *ApJ*, 690, 822
- Knutson, H. A., Lewis, N., Fortney, J. J., et al. 2012, *ApJ*, 754, 22
- Lecavelier Des Etangs, A., Ehrenreich, D., Vidal-Madjar, A., et al. 2010, *A&A*, 514, A72
- Lockwood, A. C., Johnson, J. A., Bender, C. F., et al. 2014, *ApJL*, 783, L29
- Madhusudhan, N. 2012, *ApJ*, 758, 36
- Madhusudhan, N., Knutson, H., Fortney, J., & Barman, T. 2014, ArXiv e-prints
- Madhusudhan, N. & Seager, S. 2009, *ApJ*, 707, 24
- Mandel, K. & Agol, E. 2002, *ApJL*, 580, L171
- Mandell, A. M., Drake Deming, L., Blake, G. A., et al. 2011, *ApJ*, 728, 18
- Marcy, G. W., Butler, R. P., Williams, E., et al. 1997, *ApJ*, 481, 926
- Mazeh, T., Tamuz, O., & Zucker, S. 2007, in *Astronomical Society of the Pacific Conference Series*, Vol. 366, *Transiting Extrapolar Planets Workshop*, ed. C. Afonso, D. Weldrake, & T. Henning, 119
- Miller-Ricci Kempton, E. & Rauscher, E. 2012, *ApJ*, 751, 117
- Montalto, M., Santos, N. C., Boisse, I., et al. 2011, *A&A*, 528, L17
- Öberg, K. I., Murray-Clay, R., & Bergin, E. A. 2011, *ApJL*, 743, L16
- Perna, R., Menou, K., & Rauscher, E. 2010, *ApJ*, 724, 313
- Pont, F., Knutson, H., Gilliland, R. L., Moutou, C., & Charbonneau, D. 2008, *MNRAS*, 385, 109
- Rasio, F. A., Tout, C. A., Lubow, S. H., & Livio, M. 1996, *ApJ*, 470, 1187
- Rauscher, E. & Menou, K. 2010, *ApJ*, 714, 1334
- Redfield, S., Endl, M., Cochran, W. D., & Koesterke, L. 2008, *ApJL*, 673, L87
- Showman, A. P., Fortney, J. J., Lewis, N. K., & Shabram, M. 2013, *ApJ*, 762, 24
- Showman, A. P., Fortney, J. J., Lian, Y., et al. 2009, *ApJ*, 699, 564
- Showman, A. P. & Guillot, T. 2002, *A&A*, 385, 166
- Showman, A. P. & Polvani, L. M. 2011, *ApJ*, 738, 71
- Sing, D. K., Pont, F., Aigrain, S., et al. 2011, *MNRAS*, 416, 1443
- Snellen, I. A. G., de Kok, R. J., de Mooij, E. J. W., & Albrecht, S. 2010, *Nature*, 465, 1049
- Swain, M. R., Deroo, P., Griffith, C. A., et al. 2010, *Nature*, 463, 637

Swain, M. R., Vasisht, G., & Tinetti, G. 2008, *Nature*, 452, 329

Tamuz, O., Mazeh, T., & Zucker, S. 2005, *MNRAS*, 356, 1466

Torres, G., Winn, J. N., & Holman, M. J. 2008, *ApJ*, 677, 1324

## 6.A Modeling and removal of the stellar spectrum

We utilized archival data of HD 189733 taken with CRIRES and the 0.2'' slit on August 10, 2010 (program 085.C-0852) while the planet was around secondary eclipse. These data were complemented by observations of the telluric standard  $\zeta$  Peg (spectral type B8V) taken during the same night, and morning calibration frames. The central wavelength for these observations ( $\lambda_{\text{ref}} = 2332.82$  nm) was shifted by one CRIRES detector towards the red with respect to our science frames. Therefore, detector #1 of our data was not covered by these auxiliary observations, and an alternative analysis was applied (see below). The spectra of HD 189733 and  $\zeta$  Peg were calibrated in the same way as our transit observations for what concerns dark subtraction, non-linearity correction, flat-fielding, extraction of the one-dimensional spectra, and correction of the odd-even effect and of bad pixels.

### 6.A.1 Creating the telluric spectrum

Subsequently, a telluric spectrum was extracted from the  $\zeta$  Peg observations, by using the fact that the star does not have significant spectral lines at the observed wavelength. Each of the observed spectra of  $\zeta$  Peg was aligned to the mid-spectrum of the series by linearly fitting the difference in the centroid position of telluric lines as a function of pixel value, and by spline-interpolating the spectra based on the fit. A master telluric spectrum was then obtained by averaging the aligned spectra in time. The wavelength solution was finally determined by comparing the pixel position of the telluric lines to their wavelengths listed in the HITRAN database, and by fitting the (pixel, wavelength) relation with a quadratic solution.

### 6.A.2 Creating the stellar spectrum

The calibration spectra of HD 189733 were aligned and wavelength-calibrated similarly to our science spectra. In this case, the template spectrum from the alignment was created by utilizing the master telluric spectrum obtained above and a high-resolution Kurucz spectrum computed for the star. The latter well reproduces the position of the stellar lines, but the amplitudes are incorrect. However, this has a minor effect on the cross correlation. Also, differently from the science spectra, these calibration spectra were shifted by spline interpolation to the wavelength scale of the master telluric spectrum. Subsequently, they were averaged in time and the master telluric spectrum was subtracted. In this way we obtained a high-S/N stellar spectrum of HD 189733.

### 6.A.3 Fitting the CO lines

As a first attempt, we fitted the position and amplitude of all the lines in the stellar spectrum. However, when trying to subtract such a fit from the science frames, some of the positions were not accurate enough. Displacement at the level of 0.2-0.3 pixels were causing stellar residuals, subsequently amplified by the cross correlation. We therefore adopted a different approach, by extracting from the HITRAN database the positions of the deepest lines of the 2-0 R-branch CO ladder in the observed wavelength range, for a temperature of 5000 K. We then fitted the amplitudes of these lines to the stellar spectrum obtained above. In this way we only missed 4 prominent stellar lines not due to CO absorption, while the  $\sim 90$  CO lines were correctly fitted and could be subtracted from the science spectra as explained below. We note that, apart from a global scaling factor, the amplitudes in the HITRAN database were already a close match to the observed spectrum of HD 189733, in particular for the shortest wavelengths (for detector #2 of the science observations). We therefore utilized this scaling factor to subtract the stellar spectrum from detector #1, which is not covered by the above ancillary observations.

### 6.A.4 Subtracting the CO lines

The final stellar spectrum was built by Doppler-shifting the the CO lines fitted as above, according to the stellar radial velocity:

$$v_S = v_{\text{sys}} + K_S \sin[2\pi(\varphi + 0.5)], \quad (6.15)$$

where  $K_S = (205 \pm 6) \text{ m s}^{-1}$  is the stellar radial velocity amplitude of HD 189733 (Bouchy et al. 2005). Each line was consequently convolved with a rotationally-broadened profile (Simon Albrecht, private communication) corresponding to  $v \sin i = (3.316_{-0.067}^{+0.017}) \text{ km s}^{-1}$ , and accounting for the distortion and the light loss due to planetary transit (the Rossiter McLaughlin effect). The amplitudes of the CO lines were fixed to the values determined above.

The stellar-subtracted spectrum  $F_{\text{sub}}(t)$  was finally obtained from the observed spectrum  $F_{\text{obs}}(t)$  and the Doppler-shifted and normalized stellar spectrum  $F_{\text{star}}(t)$  as

$$F_{\text{sub}}(t) = F_{\text{obs}}(t)[1 - F_{\text{star}}(t)]. \quad (6.16)$$

An example of stellar-subtracted data is provided in Figure 6.2.

# 7

---

## *Future exoplanet characterization at high spectral resolution*

---

This thesis has mostly focused on the use of ground-based, high-resolution spectroscopy to characterize the atmospheres of exoplanets. This Chapter is devoted to summarize the unique advantages of this novel technique, the current achievements, possible improvements during the next 5-10 years, and the prospects for the next generation of Extremely Large Telescopes (ELTs).

### **7.1 Advantages of high-resolution spectroscopy**

High-resolution spectroscopy is a particularly robust technique for constraining some of the basic properties of exoplanet atmospheres. It is much less affected by systematics than low-resolution or photometric observations, with noise levels only 10-20% away from the photon noise in most of the cases (see, e.g., Chapter 4). The following planet properties are particularly well constrained by this observational technique:

- **Atmospheric composition:** due to the fact that at very high spectral resolution each molecular species has a unique fingerprint, it is possible to robustly determine the composition of exoplanet atmospheres with this method. This means that, for instance, no spurious signal can be obtained by cross-correlating water lines with methane or carbon monoxide lines. It is a big advantage over low-resolution spectroscopy or broad-band photometry, for which molecular bands often overlap, introducing a level of ambiguity in the interpretation;
- **Planet radial velocities:** high-resolution spectroscopy probes the variations in the planet radial velocity while it moves across the orbit. By pairing planet and stellar radial velocities, the system is treated as a spectroscopic binary and the planet/star mass ratio is determined. For non-transiting planets with a good estimate of the host-star mass, we can solve for the true planet mass and the orbital inclination. In the case of evolved, close-in planet, this is so far the only method capable to access the atmospheres of bodies which do not transit. In this thesis we have determined the planet mass and orbital inclination of non-transiting planets in Chapters 2, 3, and 4;
- **Bulk thermal atmospheric structure:** dayside high-dispersion observations are particularly sensitive to the thermal structure of the planet atmosphere, e.g., to the presence or the absence of a thermal inversion layer. They measure



the depth of molecular lines relative to each other and relative to the planet continuum, which is proportional to the temperature difference between the planet photosphere (formed deep in the atmosphere) and the core of the lines (formed higher up in the atmosphere). For temperature decreasing with pressure (non-inverted atmosphere), the core of the line will form in an atmospheric layer cooler than the continuum, resulting in *absorption* lines. For temperature increasing with altitude (thermal inversion), the core of the line will form in a hotter layer and *emission* lines will be observed. It is worth noting that all the dayside observations presented in this thesis (Chapters 2, 3, and 4) find atmospheres lacking strong thermal inversions. This confirms the general trend of most of the exoplanets characterized to date.

- **Relative molecular abundances and C/O ratio:** high-dispersion observations cannot effectively constrain *absolute* molecular abundances (see below). However, they can provide a measurement of *relative* molecular abundances. These can be translated into a measurement of the atmospheric C/O ratio for hot Jupiters. Current attempts to perform this type of analysis (see Chapters 4 and 6) are limited by the incomplete sensitivity to all the major carbon- and oxygen-bearing molecules in a small spectral range, but see Section 7.3 for strategies to overcome this limitation.

## 7.2 Current limits of high-resolution spectroscopy

High-dispersion observations have only recently become successful in characterizing exoplanets, and mostly due to the work presented in this thesis. It is therefore important to highlight not only the advantages, but also the challenges potentially affecting the method, in order to stimulate a constructive participation of a broader community. In this Section the main limits of the technique, together with possible solutions, are presented.

- **No absolute abundances:** as explained in Section 7.1, observations at high spectral resolution are sensitive to the temperature difference between the two atmospheric layers at which the planet continuum (deep in the atmosphere) and the line cores (higher up in the atmosphere) are formed. This temperature contrast is degenerate with the atmospheric lapse rate (i.e., the rate at which temperature changes with pressure) and the molecular abundances, meaning that multiple combinations of the two variables produce the same observed line depth. Furthermore, our data analysis removes any information about absolute fluxes and broad-band spectral variations. Therefore, there is an additional degree of freedom regarding the temperature of the planet continuum. This renders high-dispersion observations in a narrow spectral range particularly insensitive to absolute molecular abundances and the detailed temperature-pressure ( $T/p$ ) profile;
- **The observable sample is small:** high-resolution spectroscopy is currently limited to stars brighter than  $K = 7-8$  mag and planets with orbital periods less

than 7-8 days, for 10 hours of integration time with a CRIRES-like spectrograph at a 8-meter telescope. This translates in a sample of  $\sim 10$  exoplanet systems across the entire sky;

- **Lack of NIR high-resolution spectrographs:** in July 2014, CRIRES will be removed from the VLT for an upgrade, and it will probably stay idle for 3-4 years. If that will happen, there will be no NIR spectrograph with resolution  $\geq 50,000$  and mounted to a 8-10m class telescope in the world.
- **Molecular line lists at high temperatures:** exoplanet characterization at high spectral resolution is possibly limited by the lack of accurate line lists for the temperatures relevant to close-in planets ( $T > 1000$  K). Incompleteness or inaccuracies in the line position and strength could potentially smear the cross-correlation signal or even cancel it completely (Hoeijmakers et al. in prep.). In response to the need of the exoplanet community for accurate laboratory measurements and quantum-mechanical simulations, updated catalogues have been recently published for a good fraction of molecules relevant to the extreme conditions of hot planets (e.g. Barber et al. 2014; Yurchenko & Tennyson 2014).

### 7.3 The coming years

During the past 3-4 years, exoplanet characterization at very high spectral resolution has just started to show its full potential. Before the next-generation of Extremely Large Telescopes will go online, it is possible to improve and extend the achievements of this novel observational method in the following ways:

- **Observing a wider spectral range:** relative molecular abundances can be better constrained by observing across a wider spectral range, or at multiple wavelengths. As de Kok et al. (2014) pointed out for a CRIRES-like instrument, the best regions to detect the main C- and O-bearing molecules are around  $2.3 \mu\text{m}$  and  $3.5 \mu\text{m}$ . These bands contain significant opacity from CO, CO<sub>2</sub>, H<sub>2</sub>O and CH<sub>4</sub>. It is also possible to test for disequilibrium chemistry, for example by targeting HCN and C<sub>2</sub>H<sub>2</sub> at  $3.1 \mu\text{m}$ . These two molecular species are also important when testing carbon-rich ( $\text{C}/\text{O} > 1$ ) atmospheres, as their abundances in chemical equilibrium become comparable to that of CH<sub>4</sub> (Madhusudhan 2012);
- **Improved design of NIR spectrographs:** the lack of high-resolution infrared spectrographs mounted at 8-10m class telescopes can largely be compensated by instruments with slightly lower resolution mounted at 3-4m class telescopes and having significantly wider spectral range and/or a better throughput. The cross-correlation signal increases approximately with the square root of the number of deep molecular lines, which corresponds to the square root of the spectral range. Furthermore, by substituting narrow entrance slits with, e.g., image slicers and scrambled fibers, the instrument throughput could easily

increase to  $\sim 15\%$ , a factor of  $\sim 5$  greater than for CRIRES. This means that, in terms of signal-to-noise, an instrument capable to cover one entire near-infrared band with the above throughput should be a factor of 5-6 faster than CRIRES in detecting exoplanet atmospheres, which means it would still be advantaged even if mounted at a 2-meter telescope.

The high-resolution signal is also strongly dependent on spectral resolution. Since for giant planets the observed spectral lines are unresolved, their FWHM scales approximately linearly with the resolution, which implies the contrast between the continuum and the line core also scales linearly with the spectral resolution<sup>1</sup> This means that a spectrograph such as NIRSPEC at Keck with  $R = 25,000$  should deliver approximately 1/2 of the signal of CRIRES for equal observing time and spectral range.

- **Pairing low- and high-resolution observations:** some of the degeneracies in the atmospheric retrieval can be solved by pairing observations at high and low spectral resolution. In particular, the planet continuum temperature could be estimated for transiting planets from secondary-eclipse measurements, and for non-transiting planet it could be constrained from broad-band phase-curve variations.
- **Developing consistent retrieval algorithms:** the amount of complementary information carried by low- and high-resolution spectroscopy extends beyond the point discussed above. The two spectral resolution regimes probe different atmospheric pressures, in both transmission and dayside spectroscopy. In order to extract the maximum information from the observations, we need self-consistent retrieval algorithms capable to take all aspects into account. In particular, Bayesian retrieval seems to be favored in this sense, given the high number of (possibly correlated) parameters to include;
- **Optical high-resolution spectroscopy:** early attempts to detect reflected light from exoplanets (Collier Cameron et al. 1999; Charbonneau et al. 1999) only resulted in upper limits, because most of the hot Jupiters have a very low Bond albedo, and because instruments were limited in resolution, spectral range, and stability. Since a few exoplanet hint today towards a relatively high Bond albedo (e.g., Kepler-7 b, Demory et al. 2011), in the near future it might be possible to detect reflected light at high resolution. Furthermore, the planets suspected to host an atmospheric inversion layer should have high-altitude absorbers such as TiO or VO (Hubeny et al. 2003), capable to block the incoming visible starlight. These species should show detectable molecular lines in the optical transmission spectra of the most irradiated exoplanets.
- **Detecting atmospheric circulation:** hot-Jupiter atmospheres are thought to show two main regimes of atmospheric circulation, namely a strong day- to night-side flow or an equatorial super-rotation due to eastward jets (Miller-Ricci Kempton & Rauscher 2012; Showman et al. 2013). Interestingly, these two

---

<sup>1</sup>This scaling approximately holds for  $R = 20,000$ - $200,000$ . At lower resolutions, blending of molecular lines becomes dominant. At higher resolutions, the lines start to be resolved.

regimes would produce a detectable signature in transmission high-resolution spectroscopy. In the former case, the peak of the cross-correlation would be blue-shifted, while in the latter case it would be broadened. Since the disk-averaged wind speed is expected to be small (a few km/s), these effects are comparable with the resolution of the current and planned spectrographs. The stability of the instrument profile is therefore essential in this case, and this requirement seems to be met by most of the upcoming spectrographs, as described above. The detection of rotational broadening in the line profile of the transmission spectrum of HD 189733 b is presented in Chapter 6.

## 7.4 The next decade: Extremely Large Telescopes

The next 5-10 years will likely see another breakthrough in the field of exoplanets, which is the discovery of terrestrial planets in the habitable zone of nearby stars. From statistical work (Kopparapu 2013; Dressing & Charbonneau 2013), we know already that 15-60% of M-dwarfs host a terrestrial planet ( $0.5-1.4 R_{\oplus}$ ) in the habitable zone. The occurrence of terrestrial planets around solar-type stars is more uncertain, due to the incompleteness of radial-velocity and transit surveys. By extrapolating current statistics, about 5% of Suns should host a planets with radius within  $0.5-1.4 R_{\oplus}$  and receiving between  $1/4$  and 1 solar constants ( $340-1360 \text{ W m}^{-2}$ ).

A number of surveys is already scanning the sky looking for planets around M-dwarfs (MEarth South/North, SPECULOOS, ExTrA, APACHE). Moreover, other planned surveys aim to find planets orbiting the brightest stars. The all-sky survey MASCARA (Snellen et al. 2013a) will come online in the next months, and will monitor stars down to  $V = 8$  mag. The TESS space mission, which is supposed to be launched in 2017, will monitor stars 30-100 times brighter than the sample of the *Kepler* mission, finding more than 3000 planets orbiting the brightest known stars, and among these  $\sim 500$  Earth-size and super-Earth planets. This sample will be a treasure to study during the next decade. It is therefore crucial to put the next generation of ELTs in context. When these giants will be online, we will have found terrestrial planets in the habitable zones of their host stars. At that time, we will need to characterize these planets and determine with high confidence the existence of a true Earth twin. In this context, there are a number of unique advantages by observing at high resolution:

- **Characterizing bright systems:** differential (spectro-)photometry of very bright targets will be limited by the lack of comparison stars. Moreover, with ELTs the stars will saturate even for sub-second exposure times. High-resolution spectroscopy allows us to self-calibrate the data (see Chapters 2, 3, 4, and 6), so that no reference star is needed to perform the observations. Moreover, saturation will be avoided thanks to the high-dispersion of the starlight. These will be enormous advantages for studying the sample of the brightest and closest exoplanets;
- **O<sub>2</sub> in terrestrial planets around M-dwarfs:** Snellen et al. (2013b) pointed out that the high-resolution transmission signal of molecular oxygen in the A-

band ( $0.76 \mu\text{m}$ ) relative to the continuum of an M-dwarf is only a factor of  $\sim 3$  weaker than the CO dayside signal detected in  $\tau$  Boötis b. The big difference is that  $\tau$  Boötis is a  $K = 3.4$  mag star, while the most likely  $I$ -magnitude of the nearest M-dwarf hosting a terrestrial planet will be 10-12. This means that, With the E-ELT and a UVES-like spectrograph, we will need 10-50 transit to reach a detection with a  $S/N = 5$ . Given the probability of observing such transits from one single location on Earth, this will take between 4 and 20 years to be reached. Feasible, but challenging;

- **Phase curves:** thanks to the high collecting power of the ELTs, it will be possible to study how the cross-correlation signal varies as function of planet orbital phase. While broad-band phase curve detect the change in the planet continuum emission while the night- and the day-side come in and out of view, at high-resolution phase curves would measure the change in the depth of the spectral lines. For the most irradiated exoplanets, the atmospheric lapse rate could be steeper on the night side than on the dayside (Showman et al. 2009), producing a stronger detected signal (de Kok et al. 2014). Therefore, phase curves at low and high resolution carry complementary information about the planet atmospheres. They can constrain the planet albedo, recirculation efficiency, and the change in the planet  $T/p$  profile during the course of a full day;
- **True planet line spectra:** for the brightest hot Jupiters, the signal provided by an ELT will be enough to detect the planet spectrum directly by shifting the spectra to the planet rest frame and summing them in time, without the need of the cross-correlation. This will finally allow us to measure the true line-by-line spectrum of an exoplanet, without relying on atmospheric models;
- **Winds:** the combination of an extremely large telescope and an extremely high-resolution spectrograph could in principle resolve the vertical wind pattern in hot-Jupiter atmospheres. Based on our model planet spectra, the molecular lines of hot giant planets start to be resolved at a spectral resolution of  $2\text{-}3 \times 10^5$ . Since the wind speed and direction can change as a function of atmospheric pressure, it is in principle possible to measure these changes by looking for asymmetries in the line profile from the core to the wings. For example, a strong jet wind at high altitude and a relatively calm atmosphere at the level of the photosphere would produce a skewed line profile.
- **Combining high spatial and spectral resolution:** direct imaging techniques only recently started to couple high spatial contrast with low-resolution spectroscopic capabilities, in order to better suppress speckle noise. We have designed and recently tested a way to couple high-contrast imaging with high-resolution spectroscopy. In this way, the typical star/planet contrast achievable in imaging ( $10^4\text{-}10^5$ ) can be coupled to the typical contrast we achieve by spectral separation plus cross-correlation ( $1\text{-}2 \times 10^5$  at  $1\sigma$ ), bringing the detectable star/planet contrast to  $10^8$  or more. The ideal way of performing this combination would be to couple integral field units with high resolution spectrographs,

a solution which is planned already for the METIS instrument at the E-ELT. We tested the method with CRIRES at the VLT, by aligning the slit with the star  $\beta$  Pic and its planet companion. With only 1 hours of integration time, we were able to detect the planet signal in the form of CO absorption at  $2.3 \mu\text{m}$ , at a S/N of 7 (Snellen et al. *Nature*, accepted). Furthermore, we detected a broadening in the line profile consistent with a rotational period of about 8 hours.

## 7.5 Final remarks

The technique presented in this thesis represents a breakthrough in exoplanet characterization. It allows us to access the atmospheres of close-in, non-transiting bodies, and to unambiguously assess the presence of molecular species, which is a fundamental requirement of future searches for biomarkers. Moreover, high-resolution spectroscopy does not need a reference star, which makes it a powerful method to apply to bright systems, which will also be the easiest to characterize. It will allow to maximize the yield of future missions searching for planets around the brightest and nearest stars, such as the TESS mission. Finally, in combination with the next generation of ELTs, high-resolution spectroscopy will enable unique and exciting science cases, ranging from the direct detection of wind patterns through their Doppler signature to the two-dimensional surface mapping of the brightest directly-imaged planets, similarly to the recent work on the brown dwarf Luhman 16-B (Crossfield et al. 2014).

In this final Chapter, we have also presented the major challenges of this method, in particular the lack of broad-band spectral information and measurements of absolute fluxes, which impact the estimate of absolute molecular abundances and of the continuum temperature. We have suggested that one way of improving these observations would be to pair low-resolution and high-resolution spectroscopy. This implies the development of new retrieval algorithms capable to treat the information from both types of observations, which is currently missing.

In conclusion, high-dispersion observations from the ground have just started to show their potential, and a broader interest from the community is desirable for bringing the technique to maturity and make it ready for the next generation of telescopes and for the sample of bright, nearby planets which will be available in 5-10 years from now.

## Bibliography

- Barber, R. J., Strange, J. K., Hill, C., et al. 2014, *MNRAS*, 437, 1828
- Charbonneau, D., Noyes, R. W., Korzennik, S. G., et al. 1999, *ApJL*, 522, L145
- Collier Cameron, A., Horne, K., Penny, A., & James, D. 1999, *Nature*, 402, 751
- Crossfield, I. J. M., Biller, B., Schlieder, J. E., et al. 2014, *Nature*, 505, 654
- de Kok, R. J., Birkby, J., Brogi, M., et al. 2014, *A&A*, 561, A150
- Demory, B.-O., Seager, S., Madhusudhan, N., et al. 2011, *ApJL*, 735, L12
- Dressing, C. D. & Charbonneau, D. 2013, *ApJ*, 767, 95
- Hubeny, I., Burrows, A., & Sudarsky, D. 2003, *ApJ*, 594, 1011
- Kopparapu, R. K. 2013, *ApJL*, 767, L8
- Madhusudhan, N. 2012, *ApJ*, 758, 36
- Miller-Ricci Kempton, E. & Rauscher, E. 2012, *ApJ*, 751, 117
- Showman, A. P., Fortney, J. J., Lewis, N. K., & Shabram, M. 2013, *ApJ*, 762, 24
- Showman, A. P., Fortney, J. J., Lian, Y., et al. 2009, *ApJ*, 699, 564
- Snellen, I., Stuik, R., Otten, G., et al. 2013a, in *European Physical Journal Web of Conferences*, Vol. 47, *European Physical Journal Web of Conferences*, 3008
- Snellen, I. A. G., de Kok, R. J., le Poole, R., Brogi, M., & Birkby, J. 2013b, *ApJ*, 764, 182
- Yurchenko, S. N. & Tennyson, J. 2014, *ArXiv e-prints*

---

# Samenvatting

---

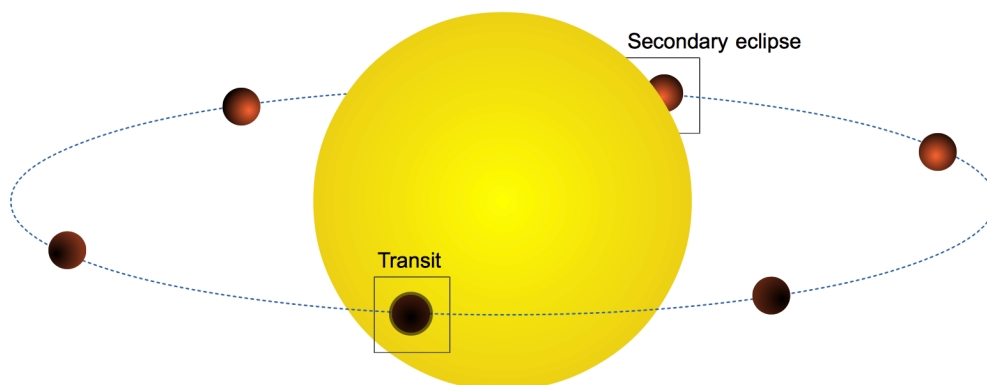
## Een enorme diversiteit aan exoplaneten

Planeten rondom andere sterren dan onze zon worden *exoplaneten* genoemd. De studie van exoplaneten heeft zich in minder dan 20 jaar ontwikkeld van speculatie naar solide waarnemingen, met meer dan duizend ontdekte planeten. Een van de meest in het oog springende eigenschappen van exoplaneten is hun diversiteit, en het ontbreken van planetenstelsels zoals ons zonnestelsel. Er zijn bijvoorbeeld reuzenplaneten die tien keer dichter bij hun moederster staan dan Mercurius, zogenaamde *hete Jupiters*. Recentelijk is ook ontdekt dat de meest voorkomende planeten niet in ons zonnestelsel vertegenwoordigd zijn, de zogenaamde super-Aardes met massa's tussen die van onze planeet en Uranus.

Niet alleen zijn onlangs grote successen behaald in het vinden van exoplaneten, maar ook in het bepalen van hun eigenschappen. Zowel de vorm, grootte en inclinatie van de baan, als de massa en straal van de planeet worden tegenwoordig vaak met een goede nauwkeurigheid bepaald door het combineren van de twee belangrijkste zoekmethodes: de radiële snelheidmethode en de transitmethode. Met de eerste techniek wordt de planeet gevonden door de beweging van de ster om het gemeenschappelijke zwaartepunt. Dit zorgt ervoor dat de straling van de ster roodverschoven wordt wanneer de ster van ons af beweegt, en blauwverschoven als deze naar ons toe beweegt. Dit resulteert in typische verschuivingen tot honderden meters per seconde. Met de tweede methode wordt het licht van het systeem (ster+planeet) nauwlettend in de gaten gehouden om de vermindering van het licht tijdens de passage van de planeet voor of achter de ster waar te nemen (zie Figuur 8.1 voor een illustratie van de geometrie van een planeetovergang).

Planeetovergangen geven ook toegang tot hun atmosfeer. Terwijl een planeet voor de ster langs trekt, sijpelt een klein beetje sterlicht door de planeetatmosfeer heen, waardoor absorptie van atomen en moleculen zichtbaar wordt. Op golflengtes van atmosferische absorptie lijkt de planeet iets groter en wordt er effectief meer sterlicht verduisterd. Dit fenomeen wordt gebruikt om het *transmissiespectrum* van een exoplaneet te meten, wat in feite een maat is voor de straal van de exoplaneet als functie van golflengte. Een andere manier om toegang te krijgen tot de atmosferen van planeten is de missende straling te meten wanneer de planeet achter de ster verdwijnt (een zogenaamde secundaire eclips). In het zichtbare licht is dit meestal gereflecteerd sterlicht. In het infrarood kan zo de warmtestraling van de planeet direct worden waargenomen. Energie vanuit diepe lagen in de planeet wordt op verschillende hoogtes uitgestraald. Net als in de aardse atmosfeer variëren druk en temperatuur als functie van hoogte. Hoewel de druk altijd afneemt met hoogte, kan de verandering in temperatuur ingewikkelder zijn. Dat betekent dat de warmte uit de diepe atmosfeer uitgestraald kan worden in lagen die kouder of warmer zijn. In het geval van warmere lagen (een zogenaamde inversie) zal de planeet helderder lijken (emissielijnen), en in het geval van koudere lagen zwakker (absorptielijnen).





Figuur 8.1: geometrie van een planeet met een overgang. Doordat de waarnemer de baan van de planeet vanaf de zijkant ziet, kan de planeetschijf zich voor (transit) of achter (eclips) de sterschijf bewegen.

Door de helderheid van de planeet als functie van golflengte te meten, gebruikmakende van de secundaire eclips, kunnen astronomen in principe de samenstelling van de atmosfeer meten, alsmede de verticale temperatuurverloop en de mechanismes die de herverdeling van energie van de dagzijde naar de nachtzijde van de planeet bepalen. Dit levert vooralsnog veel vragen op. We begrijpen bijvoorbeeld niet wat de dominante factoren zijn die bepalen of een atmosfeer een inversielaag heeft of niet. Waarschijnlijk hangt dit af van de aanwezigheid van specifieke moleculen die het sterlicht kunnen absorberen, zoals ozon dat in de aardatmosfeer doet. Het zou ook kunnen afhangen van hoe de hoeveelheid koolstof zich verhoudt met die van zuurstof, waardoor sommige chemische stoffen niet of wel kunnen worden gevormd in de planeetatmosfeer. Dit kan weer afhangen van waar de planeet is geboren in de schijf van gas en stof rondom de jonge ster. We hebben veel meer waarnemingen nodig van veel meer planeten om hier achter te komen.

## Het karakteriseren van exoplaneten is een uitdaging

De meeste open vragen zijn een gevolg van de hoge moeilijkheidsgraad van de waarnemingen. De signalen van planeetatmosferen zijn erg zwak. In het beste geval komt er slechts een enkele foton van de planeet voor elke duizend fotonen van de ster. Stabiliteit is daarbij enorm belangrijk, en daarom hebben de ruimtetelescopen altijd een voortrekkersrol gespeeld. Echter hun spiegels zijn niet alleen kleiner vergeleken met telescopen op Aarde, maar deze instrumenten hebben ook een lagere spectrale resolutie, wat betekent dat ze minder goed in staat zijn het licht op te splitsen in individuele golflengtes. Dit maakt de identificatie van absorptiebanden, die vaak in golflengte overlappen, lastig. Bovendien zijn deze telescopen niet voor planeetwaarnemingen ontworpen, waardoor ze ver voorbij hun ontwerpspecificaties worden gebruikt. Hierdoor zijn er vaak systematische effecten aanwezig die

planeetsignalen kunnen maskeren, of een onechte detectie kunnen opleveren. Vanaf de grond is dit trouwens nog erger, omdat onze aardatmosfeer er nog een schepje bovenop doet.

Over de optimale strategie om systematische effecten te verwijderen wordt hevig gedebatteerd. Pas onlangs convergeren exoplaneetwetenschappers, door een collectieve inspanning, naar objectieve data-analyses en reproduceerbare resultaten. Systematische effecten worden pas echt zorgwekkend als men denkt aan het ultieme doel van de exoplaneetwetenschap: het vinden van bewoonbare planeten en het bepalen hoe vaak leven, zoals wij dat kennen, in ons Melkwegstelsel voorkomt. Dit doel heeft robuuste en betrouwbare waarneemmethodes nodig die op een grote verscheidenheid aan planeten toepasbaar zijn. Het werk in dit proefschrift is voornamelijk gericht op het bestuderen en ontwikkelen van een strategieën om de meeste van de bovengenoemde belemmeringen te overwinnen.

## Mijn proefschrift

In dit proefschrift presenteer ik een nieuwe waarneemtechniek om exoplaneet atmosferen op te meten. Deze is gebaseerd op hoge resolutie spectroscopie met grondtelescopieën.

De keuze voor het hoogst mogelijke oplossend vermogen ( $R \sim 100,000$ ) brengt twee fundamentele voordelen met zich mee. Ten eerste worden absorptiebanden opgelost in individuele lijnen, zodat elke soort molecuul een unieke en herkenbare vingerafdruk heeft, wat een eenduidige interpretatie van spectra oplevert. Ten tweede kan de extra absorptie in de aardatmosfeer, wat normaal gesproken de kwaliteit van grondwaarnemingen sterk degradeert ten opzichte van waarnemingen in de ruimte, effectief worden gescheiden van het planeetsignaal. Dit komt doordat deze extra absorptie niet in golflengte verandert, terwijl het planeetspectrum onderhevig is aan een veranderende dopplerverschuiving veroorzaakt door de baanbeweging van de planeet. Samen hebben deze twee effecten het mij mogelijk gemaakt om onomstotelijk de aanwezigheid van koolmonoxide en waterdamp in de atmosferen van vijf exoplaneten te bepalen, wat een verdubbeling betekende van het aantal planeten waarvoor deze moleculaire gassen met enig vertrouwen zijn gedetecteerd (zie Hoofdstukken 2, 3, 4 en 6).

Verder heb ik een aantal metingen verricht die onmogelijk zijn met andere technieken. Ik heb voor het eerst keer signalen gemeten van planeten die geen planeetovergang vertonen, en direct hun omloopbeweging bepaald (Hoofdstukken 2, 3 en 4). Dit vertaalt zich ook in een schatting van hun planeetmassa en inclinaties van hun planeetbanen. Het is me ook gelukt om de rotatie van een exoplaneet waar te nemen (Hoofdstuk 6), welke laat zien dat de planeet waarschijnlijk synchroon met de baanrotatie om haar as draait, zoals onze maan om de aarde, en zoals voorspeld door getijdentheorieën. Een ander interessant aspect van dit proefschrift is dat geen van de waargenomen planeten een inversielaag lijkt te hebben. Terwijl de metingen hieraan op lage resolutie heel moeilijk zijn, produceren de aan- of afwezigheid van inversielagen absorptie- of emissielijnen die relatief makkelijk in deze metingen te bepalen zijn. Tenslotte heb ik laten zien dat hoge-resolutie spectroscopie kan worden

gebruikt om de koolstof-zuurstof verhouding in de atmosfeer te bepalen, alhoewel nog wel met een grote onzekerheid.

## Waarom hete, dichtbijstaande planeten?

In dit proefschrift heb ik de nadruk gelegd op de studie van atmosferen van planeten die heel dicht om hun ster draaien. Hier zijn twee redenen voor. Ten eerste zijn deze planeten het makkelijkst waar te nemen in zowel zichtbaar als infrarood licht. Hun atmosferen zijn heet en wat uitgezet, wat betekent dat ze een groter deel van het sterlicht blokkeren. De warmtestraling van de planeet is ook feller door de hoge temperaturen, wat het contrast tussen ster en planeet vergroot. Zulke hete reuzenplaneten hebben ook als voordeel dat ze waarschijnlijk redelijk homogeen in samenstelling zijn, wat de complexiteit in de atmosfermodellen sterk doet verminderen.

Het is erg belangrijk om waarneemtechnieken te testen op de makkelijkste objecten. Hoewel exoplaneetwetenschappers over het algemeen erg enthousiast zijn over de toekomstige mogelijkheden om aardachtige planeten te vinden en te karakteriseren, worden de exoplaneten die we nu kunnen onderzoeken compleet gedomineerd door hete Jupiters zoals die onderzocht zijn in dit proefschrift. Het is belangrijk om onze meetmethodes op deze objecten te verfijnen, voordat we onze pijlen op zwakkere en complexere planeten richten. Tenslotte zijn deze dichtbijstaande planeten ook fascinerend, omdat ze zich in zulke extreme omstandigheden bevinden. De enorme energie van de ster kunnen de atmosferen van heel kleine planeten compleet wegvagen en uiteindelijk hun oppervlak laten verdampen. Er is al een mogelijke desintegrerende planeet gevonden door de *Kepler* satelliet, en Hoofdstuk 5 van dit proefschrift geeft een analyse en modellering van haar lichtcurve, wat meer bewijs levert voor de desintegratie.

---

# Riepilogo

---

## La sorprendente diversità dei pianeti extrasolari

I pianeti che orbitano stelle diverse dal Sole si chiamano *esopianeti*, oppure *pianeti extrasolari*. In soli 20 anni, la ricerca dei pianeti extrasolari è passata dalla pura speculazione a una solida evidenza osservativa, con più di mille pianeti attualmente scoperti. Una delle caratteristiche più stupefacenti degli esopianeti è la loro varietà, e la mancanza di corpi analoghi nel sistema solare. Per esempio, conosciamo pianeti giganti, detti *pianeti gioviani caldi*, che orbitano dieci volte più vicini al loro sole di quanto faccia Mercurio. Inoltre, sappiamo che i pianeti più comuni nella Via Lattea hanno dimensioni intermedie tra quelle della Terra e di Urano. Non c'è traccia di queste due categorie di pianeti intorno al Sole.

Grandi progressi sono stati fatti non solo nella scoperta dei pianeti extrasolari, ma anche nello studio delle loro caratteristiche. La forma, la dimensione, e l'inclinazione dell'orbita, così come la massa e il raggio del pianeta, sono oggi determinati con una buona accuratezza attraverso la combinazione dei due principali metodi per scoprire esopianeti: le velocità radiali e i transiti. Con il primo metodo il pianeta viene identificato attraverso il moto della stella che lo ospita attorno al baricentro del sistema. Questo moto provoca uno spostamento verso il rosso o verso il blu della radiazione stellare, a seconda che l'astro si allontani o si avvicini a noi. Ne risultano righe stellari soggette all'effetto Doppler, con velocità tipiche di decine o centinaia di metri al secondo. Questo fenomeno è del tutto analogo alla variazione del tono di una sirena posta su un veicolo in movimento, per esempio un'ambulanza. Con il secondo metodo, la luce proveniente dal sistema pianeta + stella è monitorata con precisione per rilevarne una piccola diminuzione dovuta al passaggio del pianeta di fronte o dietro al disco stellare, come mostrato in Figura 9.2.

La scoperta dei pianeti transitanti ci ha anche dato modo di accedere alle loro atmosfere. Durante un transito, una piccola parte della luce stellare filtra attraverso l'atmosfera planetaria per raggiungere l'osservatore, e viene alterata da eventuali atomi o molecole ivi presenti. Essi tendono a bloccare il passaggio dei fotoni a certe specifiche frequenze, in corrispondenza delle quali il pianeta appare più grande, perché assorbe una frazione leggermente maggiore della luce stellare. Questo fenomeno viene utilizzato per osservare il cosiddetto *spettro di trasmissione* di un esopianeta, che è essenzialmente una misura del raggio planetario in funzione della frequenza della luce.

Un altro modo per studiare le atmosfere dei pianeti transitanti è misurare la diminuzione della luce quando passano dietro al disco stellare (eclisse). Nel visibile è possibile misurare la quantità di luce riflessa, mentre nell'infrarosso si può misurare direttamente l'emissione termica del pianeta. Quest'ultima, a seconda della frequenza della luce osservata, proviene da strati atmosferici situati a diverse altitudini. Nell'atmosfera di un pianeta, la temperatura può sia diminuire che aumentare con l'altitudine. Ciò significa che la radiazione termica può provenire da regioni

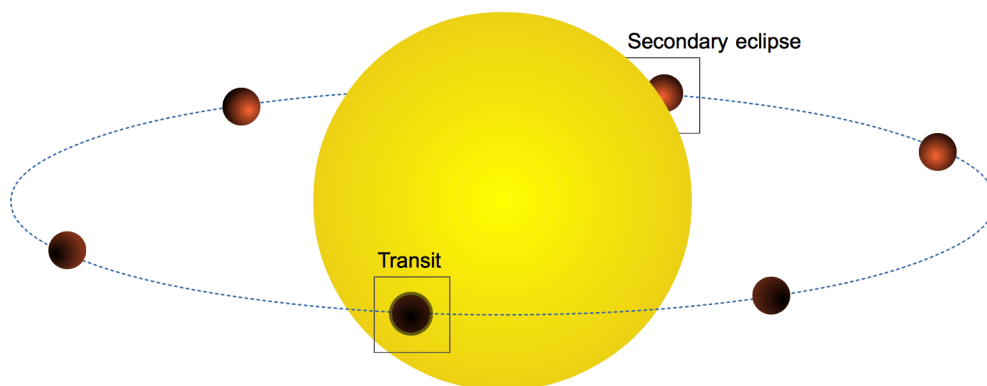


Figura 9.2: Rappresentazione schematica di un pianeta transitante. Data la vista di taglio dell'osservatore, il pianeta passa di fronte al disco stellare (transito) o ne è occultato (eclisse).

atmosferiche più calde o più fredde rispetto alla media. Nel primo caso il pianeta appare più luminoso (righe di emissione), nel secondo caso appare più debole (righe di assorbimento). Misurando la luminosità del pianeta in funzione della lunghezza d'onda gli astronomi possono quindi misurare lo *spettro termico* di un pianeta extrasolare. In pratica ciò si ottiene misurando la diminuzione del flusso ricevuto dal sistema extrasolare durante un eclisse, in funzione della lunghezza d'onda della luce osservata.

Studiando le atmosfere dei pianeti extrasolari nei due modi appena descritti gli scienziati riescono a misurare la loro composizione, la struttura termica in funzione dell'altitudine e i meccanismi che regolano la redistribuzione energetica fra l'emisfero illuminato e quello in ombra. Tuttavia, molti dettagli sono ancora da chiarire. Per esempio, non conosciamo i fattori che determinano quando la temperatura diminuisca o aumenti con l'altitudine. Il livello di irraggiamento stellare potrebbe avere un ruolo importante, così come la presenza di particolari molecole capaci di assorbire la radiazione stellare nell'ottico, in modo simile all'ozono nell'atmosfera terrestre. Un'altra variabile da considerare potrebbe essere l'abbondanza dei vari elementi chimici nell'atmosfera planetaria, potenzialmente connessa alla regione in cui il pianeta si è formato all'interno del disco protoplanetario.

Nonostante gli sforzi degli astronomi, misurare queste quantità è attualmente molto difficile, e limitato a un piccolo campione di oggetti.

## Caraterizzare gli esopianeti è una sfida continua

La maggior parte delle questioni irrisolte nello studio delle proprietà degli esopianeti è connessa a difficoltà osservative. I segnali spettrali delle atmosfere planetarie sono estremamente deboli. Nei casi più favorevoli, solo un fotone su mille appartiene al pianeta piuttosto che alla stella. Inoltre, la strumentazione migliore si trova

nello spazio, dove l'atmosfera terrestre non contamina le osservazioni in modo sensibile. Sfortunatamente gli specchi dei telescopi spaziali sono più piccoli di quelli dei telescopi a terra e gli strumenti sono dotati di una minore risoluzione spettrale. Ciò significa che sono meno efficienti nel separare la luce nelle varie frequenze che la compongono. Conseguentemente, gli astronomi campionano gli spettri dei pianeti extrasolari, potenzialmente ricchi di righe in assorbimento o emissione, con pochi punti sparsi. Questo rende difficile l'individuazione delle specie atomiche o molecolari responsabili delle modulazioni osservate.

In aggiunta, gli strumenti comunemente utilizzati per le osservazioni di esopianeti non sono stati progettati per tale scopo e vengono spinti ben oltre le loro possibilità. Di conseguenza il rumore strumentale è spesso presente ai livelli del segnale astrofisico, e deve essere rimosso efficacemente per evitare false rilevazioni. Infine, osservando dalla superficie terrestre, le variazioni nelle proprietà della nostra atmosfera possono introdurre ulteriori errori sistematici.

Queste limitazioni vanno messe in relazione all'obiettivo finale della ricerca sui pianeti extrasolari, ovvero la scoperta di altri pianeti abitabili oltre alla Terra e la ricerca di altre forme di vita nella Galassia. Questi obiettivi richiedono tecniche di osservazione robuste, affidabili e applicabili al campione più ampio possibile di pianeti. In passato c'è stato un forte dibattito riguardo alle strategie migliori per rimuovere gli effetti sistematici. Grazie allo sforzo collettivo della comunità scientifica, oggi stiamo convergendo verso tecniche di analisi dei dati oggettive, con risultati pienamente riproducibili da gruppi diversi.

Su questa linea, la mia tesi è propone un'inedita strategia osservativa volta a superare la maggior parte degli ostacoli sopra descritti.

## **Il contributo di questa tesi**

Questa tesi presenta una nuova tecnica per studiare le atmosfere dei pianeti extrasolari basata su spettroscopia ad altissima risoluzione condotta con telescopi terrestri.

La scelta di un alto potere risolvante apporta due fondamentali vantaggi. In primo luogo, è possibile individuare le singole righe di assorbimento delle bande molecolari. A questo livello di dettaglio, ogni specie possiede un proprio segno distintivo, simile ad un'impronta digitale. Ciò riduce al minimo le ambiguità nell'interpretazione degli spettri. In aggiunta, la contaminazione dell'atmosfera terrestre (assorbimento tellurico), che di solito riduce la qualità delle osservazioni da terra rispetto a quelle degli osservatori spaziali, può essere efficacemente separata dal segnale dell'esopianeta. Infatti l'assorbimento tellurico è stazionario in lunghezza d'onda, mentre lo spettro del pianeta extrasolare è soggetto a un effetto Doppler variabile dovuto al moto orbitale.

Messi assieme, questi due vantaggi ci hanno permesso di determinare senza ambiguità la presenza di monossido di carbonio e vapore acqueo nelle atmosfere di quattro esopianeti (vedi Capitoli 2, 3, 4 e 6). In aggiunta, è stato possibile misurare alcune proprietà impossibili da determinare con le tecniche precedentemente utilizzate. Per la prima volta è stato possibile studiare l'atmosfera dei pianeti che non

transitano, misurare direttamente il loro moto orbitale e di conseguenza stimare la massa del pianeta e l'inclinazione dell'orbita (Capitoli 2, 3 e 4). Inoltre, si è potuto misurare la rotazione di un pianeta extrasolare (Capitolo 6) e mostrare che il corpo sembra essere in rotazione sincrona, in linea con le predizioni teoriche.

Un altro importante risultato degli studi presentati in questa tesi è che la temperatura decresce con l'altitudine nell'atmosfera dei pianeti osservati. Questo tipo di misura è arduo a bassa risoluzione spettrale. Come spiegato in precedenza, la diminuzione o la crescita della temperatura in funzione dell'altitudine produce righe rispettivamente in assorbimento o in emissione, il cui segno distintivo può essere riconosciuto ad alta risoluzione spettrale durante l'analisi dei dati.

Infine, la spettroscopia ad alta risoluzione è stata utilizzata per fornire una stima del rapporto fra carbonio e ossigeno (C/O, vedi Capitoli 4 e 6).

## **Perché osservare pianeti caldi e vicini alle loro stelle?**

Questa tesi è incentrata sulle atmosfere di pianeti molto vicini alla loro stella madre, per una duplice ragione. Primo, questi pianeti sono i più facili da osservare sia nell'ottico che nel vicino infrarosso. Le loro atmosfere sono calde, dunque molto espanse, il che significa che filtrano una frazione maggiore della luce stellare, producendo un segnale più forte. Le alte temperature aumentano inoltre l'emissione termica del pianeta e dunque il suo flusso rispetto a quello della stella. Infine, i pianeti giganti più caldi dovrebbero essere in equilibrio chimico e la loro composizione uniforme su una larga porzione dell'atmosfera. Ciò riduce la complessità dei modelli atmosferici utilizzati per interpretare le osservazioni.

È estremamente importante verificare le tecniche osservative sugli oggetti più facili da osservare. Sebbene gli studiosi di pianeti extrasolari siano in fibrillazione per la futura ma concreta possibilità di scoprire e caratterizzare pianeti terrestri, il campione correntemente accessibile è formato dai pianeti caldi studiati in questa tesi, ed è importante raffinare le misurazioni su questi oggetti prima di passare a qualcosa di molto più complesso.

Infine, pianeti che orbitano molto vicini alla loro stella sono affascinanti anche per via dell'ambiente in cui sono situati. A causa delle alte temperature e dell'intenso flusso stellare, i pianeti più piccoli rischiano di perdere completamente la loro atmosfera. Nei casi più estremi la loro superficie può venire vaporizzata, in modo più o meno catastrofico. La missione spaziale *Kepler* sembra aver trovato un possibile pianeta in disintegrazione. Il Capitolo 5 di questa tesi presenta un'accurata analisi e un modello della sua curva di luce, volti a produrre ulteriore evidenza di questo affascinante e unico fenomeno.

---

# List of publications

---

## Refereed Publications

1. **Brogi, M.**; de Kok, R. J.; Birkby, J. L.; Schwarz, H.; Snellen, I. A. G. *Carbon monoxide and water vapor in the atmosphere of the non-transiting planet HD 179949 b*, A&A accepted (arXiv:1404.3769).
2. **Brogi, M.**; Snellen, I. A. G.; de Kok, R. J.; Albrecht, S.; Birkby, J. L.; de Mooij, E. J. W. *Detection of molecular absorption in the dayside of exoplanet 51 Pegasi b?* ApJ, 767, 27B (2013)
3. **Brogi, M.**; Keller, C. U.; de Juan Ovelar, M.; Kenworthy, M. A.; de Kok, R. J.; Min, M.; Snellen, I. A. G. *Evidence for the disintegration of KIC 12557548 b*. A&A, 545L, 5B (2012b)
4. **Brogi, M.**; Snellen, I. A. G.; de Kok, R. J.; Albrecht, S.; Birkby, J. L.; de Mooij, E. J. W. *The signature of orbital motion from the dayside of the planet  $\tau$  Boötis b*. Nature, 486, 502B (2012a)
5. **Brogi, M.**; Marzari, F.; Paolicchi, P. *Dynamical stability of the inner belt around  $\epsilon$  Eridani*. A&A, 499L, 13B (2009)
6. Snellen, I. A. G.; Brandl, B. R.; de Kok, R. J.; **Brogi, M.**; Birkby, J. L.; Schwarz, H. *Fast spin of the young extrasolar planet  $\beta$  Pictoris b*. Nature, 509, 63-65 (2014)
7. de Kok, R. J.; Birkby, J. L.; **Brogi, M.**; Schwarz, H.; Albrecht, S.; de Mooij, E. J. W.; Snellen, I. A. G. *Identifying new opportunities for exoplanet characterisation at high spectral resolution*. A&A, 561A, 150D (2014).
8. van Werkhoven, T. I. M.; **Brogi, M.**; Keller, C. U.; Snellen, I. A. G. *Analysis and interpretation of 15 quarters of Kepler data of the disintegrating planet KIC 12557548 b*. A&A, 561A, 3V (2014).
9. Birkby, J. L.; de Kok, R. J.; **Brogi, M.**; de Mooij, E. J. W.; Schwarz, H.; Albrecht, S.; Snellen, I. A. G. *Detection of water absorption in the dayside atmosphere of HD 189733 b using ground-based high-resolution spectroscopy at 3.2  $\mu$ m*. MNRAS, 436L, 35B (2013)
10. de Mooij, E. J. W.; **Brogi, M.**; de Kok, R. J.; Snellen, I. A. G.; Croll, B.; Jayawardhana, R.; Hoekstra, H.; Otten, G. P. P. L.; Bekkers, D. H.; Haffert, S. Y.; van Houtdt, J. J. *Search for Rayleigh scattering in the atmosphere of GJ1214 b*. ApJ, 771, 109D (2013)
11. de Kok, R. J.; **Brogi, M.**; Snellen, I. A. G.; Birkby, J. L.; Albrecht, S.; de Mooij, E. J. W. *Detection of carbon monoxide in the high-resolution day-side spectrum of the exoplanet HD 189733b*. A&A, 554A, 82D (2013)



12. Snellen, I. A. G.; de Kok, R. J.; le Poole, R.; **Brogi, M.**; Birkby, J. L. *Finding Extraterrestrial Life Using Ground-based High-dispersion Spectroscopy*. *ApJ*, 764, 182S (2013)
13. de Mooij, E. J. W.; **Brogi, M.**; de Kok, R. J.; Snellen, I. A. G.; Kenworthy, M. A.; Karjalainen, R. *The GROUSE project. III. K<sub>S</sub>-band observations of the thermal emission from WASP-33b*. *A&A*, 550A, 54D (2013)
14. de Mooij, E. J. W.; **Brogi, M.**; de Kok, R. J.; Koppenhoefer, J.; Nefs, S. V.; Snellen, I. A. G.; Greiner, J.; Hanse, J.; Heinsbroek, R. C.; Lee, C. H.; van der Werf, P. P. *Optical to near-infrared transit observations of super-Earth GJ 1214b: water-world or mini-Neptune?* *A&A*, 538A, 46D (2012)

## Conference Proceedings

1. Snellen, I.; de Kok, R. J.; de Mooij, E. J. W.; **Brogi, M.**; Nefs, S. V.; Albrecht, S. *Exoplanet atmospheres at high spectral resolution: A CRIRES survey of hot Jupiters*. *IAUS*, 276, 208 (2011)
2. de Mooij, E. J. W.; de Kok, R. J.; Nefs, S. V.; **Brogi, M.**; Snellen, I. *The GROUnd-based Secondary Eclipse project*. *IAUS*, 276, 478 (2011)

---

# Curriculum Vitae

---

I was born on May 12, 1983 in Grosseto, Italy, where I spent the first 19 years of my life and completed my pre-university education. In 1989 I started primary school, and in 1994 middle school. In the meanwhile, I began to be fascinated by the night sky and astronomy in general, so I decided to attend a science-oriented lyceum, from which I graduated in 2002 with the highest grade.

I subsequently moved to Pisa and enrolled in the Science Faculty for the Bachelor courses (laurea triennale) in General Physics. At that time, I was already determined to eventually study Astrophysics. In 2006, under the guidance of Prof. Paolo Paolicchi, I got my Bachelor Degree with the highest grade, presenting a research project on the analytical formalism for predicting the effects of secular resonances in dynamical evolution of celestial bodies.

After obtaining my Bachelor Degree, I started the Master courses in Astrophysics. Approximately one year thereafter, I decided to base my Master Thesis on the dynamical stability of the Habitable Zones of known exoplanets, in collaboration with Prof. Paolo Paolicchi and Prof. Francesco Marzari. A spin-off project of this work resulted in a publication in *Astronomy & Astrophysics* (Brogi et al. 2009). At the end of the project, I graduated Cum Laude and started to look for a PhD project.

In the Fall of 2009, I won a PhD position in Pisa, although not in Astrophysics. I decided to resign and search for a project in exoplanet science, intrigued by the subject in general, but in particular by observations of exoplanet atmospheres and the quest for an Earth-twin. As a result, I started my research as a PhD at Leiden Observatory, in the Netherlands, under the guidance of Prof. Ignas Snellen. As a main project, I developed a novel observational technique to probe the atmospheres of exoplanets, and I was the first to apply it to non-transiting planets, obtaining their masses and orbital inclinations (Brogi et al. 2012b, 2013, 2014). In addition, I analyzed data from the *Kepler* spacecraft in collaboration with Prof. Christoph Keller, which led to the first quantitative evidence for the evaporation of one of the *Kepler* planet candidates (Brogi et al., 2012b).

In early 2014 I have been awarded with a NASA Hubble Fellowship, which I will take at University of Colorado, Boulder, starting from September 2014. In the context of the Fellowship, I will work in collaboration with Jean-Michel Désert on the ideas presented in the final chapter of this thesis.



---

# Acknowledgements

---

Being able to defend my PhD thesis is the result of a long path that started when I was still a child. I am grateful to many people for their support throughout this journey.

First of all, none of my achievements would have been possible without my parents, so they deserve a special thanks in my mother tongue. Mamma e babbo, avete sempre creduto in me e sostenuto i miei sogni. Vi siete resi conto di quanto il cielo stellato mi ispirasse fin dall'adolescenza, e avete fatto in modo che potessi completare gli studi scientifici. So bene quanti sacrifici abbiate fatto, date le condizioni economiche della nostra famiglia. Per questo, per essere genitori meravigliosi e per il vostro amore incondizionato, vi sarò sempre grato.

I grew up in a small rural town, where attachment to the land and to practical and tangible things is still strong. This does not encourage the choice of science and research as a job. I am grateful to all the people who believed in me at the right moment and were supportive throughout my journey. First of all to my relatives, and in particular to my uncle Paolo and my cousins Francesca, Ilaria, and Luca. Secondly, to some of my teachers. With his unconventional methods, Enzo Flaminio boosted my interest for science during middle school. Grazia Stilli, my high-school literature teacher, significantly helped me to develop a critical view of life.

I have shared a large part of my life with two special friends. Sara and Giuliano, we have experienced so many things together! Not only have we shared an apartment in Pisa during university, but also our adolescence, weekends, parties, achievements and failures. So many good memories include you two, and you never judged me for my ideas or my behavior. When I needed your help you were there, and I still feel you very close even though we seldom meet anymore. Not by chance, you will sit at my side during the defense!

I shared memorable moments, the heights and the lowest points of my university years with a very special group of friends: Ale (and by that I mean il Bocco, il Cilla and DJ pacco), Ali, Damiano, il Mancio, il Leo, il Petro, Rosa, Vera. We are now all scattered across Italy and Europe, but certainly my life today partly depends on the good times that we had together, on our mutual support during troublesome times, and even on our many arguments.

My journey towards the doctorate has not been always easy. In the darkest moments, music has given me the right inspiration to go on. To my uncle Cristiano, wherever he is now, goes the highest merit, as he taught me everything I know, with endless patience. Thanks to my amazing friends and musicians Edoardo, Francesco, and Luca, for making the dream of performing live the music of Pink Floyd possible.

I feel privileged to have spent the last four years as a PhD student in the Netherlands. Living in such a welcoming country, working in a vibrant department, and meeting so many people from all over the world, truly opened my mind. Not all of these people were or are astronomers. Olmo, thanks for trying to teach me thai-chi. I was certainly the worst student in the group, but we had great fun and I will

always remember that. I hope you will make soon your way, and my best wishes for the future. Cosma, thanks for your improvised stories full of cynicism and sarcasm. Yuval, we had a lot of fun while you were in Leiden. Thanks for starting the tradition of home-brewed beer and for passing it to Marissa! Thanks to Evelijn, Yvonne, and Jeanne. Their help with all the practical matters made my moving to the Netherlands an extremely smooth transition, and my stay an enjoyable stay.

I incredibly enjoyed working in the Leiden exoplanet group. I always felt respected and treated as a colleague, rather than as a student. All my ideas have been taken seriously and often encouraged, which acquainted me with independent research very soon during the PhD. After traveling to conferences, visiting other institutes, and chatting with many astronomers, I can say that I rarely met other research groups led with such a care and success. I want to thank Ernst for his patience during my first year, for sharing his technical knowledge with me, and for always promoting collaborations and constructive discussion. Jayne, it has been a real pleasure to work with you and share the successes of the last years, the craziness of our job-hunting, and social time during conferences. Remco, thanks for helping me to understand the theoretical background behind our observations, which gave me the key to interpret our complex measurements and reach so many exciting results. Tiffany, a long time has passed since we first met in room 101. I enjoyed every bit of it, first as a friend, and then when you started to work in exoplanets. Fortunately we will meet at many other conferences in the future! Maria and Tim, collaborating with you was a great experience. You are fantastic colleagues and even more amazing in partying mood. It's a pity that you only moved from Utrecht almost at the end of your PhD, and my best wishes with your future! Anna-Lea, Emanuele, Henriette and Julien: thanks for your enthusiasm, for all our chats, and for caring so much about the social aspects of our academic life, which are too often underrated. All the best with your projects!

To my officemates, Rafa, Eva, Elisabetta, Saskia, and Clément, thanks for making our workspace so nice and livable! Rafa, the time we have shared as friends, and the way you care about your family while being such a successful scientist inspire me incredibly. My best wishes to you, Lara and Leonardo!

I greatly appreciate the distinctive social character of the Sterrewacht. I am grateful to all the colleagues sharing their ideas about science and life with me during coffee breaks, lunch time, Friday borrel, nights out and parties. Alex, Ali, Andra, Bram, Carina, Carl, Carla, Cristobal, Daniel, Ernst, Francisco, Heather, Hendrik, Jaya, Jeanette, Jesse, Joana, Kalle, Mariam, Mher, Magnus, Monica, Nienke, Pedro, Remco, Renske, Sebastiaan, Steven, Vachail, Willem, thanks for the time spent together!

With a small group of colleagues I have a special bond. They made my life in Leiden special, and certainly their support and our friendship contributed to the positive outcome of the last four years. Marissa, we met as soon as I moved in Leiden. Thanks for guiding me through the mysteries of the English language with patience, for introducing me to everyone you knew at the time, and for sharing the secrets of home-brewed beer. Thanja, it has been a real pleasure to accompany you at the piano. Thanks for dragging me to perform live again after many years.

By now you have probably realized how much playing helps me, and I hope it is the same for you! Berenice and Jesús, you both enjoy challenges, and you have the rare gift to use them to cheer you up. Thanks for dragging me out of apathy and laziness throughout these years, for the battles playing Munchkin, and for our small competitions about best food, best weather, and about everything good that comes out of Spain and Italy. It is much better to look at our countries from this perspective! Speaking of which, my special thanks to the "Italian crew". It would have been much harder without you guys. We shared the mixed feelings of being abroad and grieved for the troubles of our homeland. Mattia, sei stato un coinquilino fantastico per più di due anni. Grazie per avermi insegnato che alcuni fatti della vita si digeriscono molto meglio con un po' di sarcasmo e umorismo. Marco, sei un integralista del beach-volley e delle torte il lunedì pomeriggio. Grazie per le nostre partite tiratissime, per le chiacchierate sulle difficoltà della vita accademica, e per le risate che ci fai sempre fare a pranzo e in Kaiser Lounge. Silvia (pron. Sylbia): tra le molte cose che abbiamo condiviso, grazie per avermi fatto rendere conto che il sessismo nel mondo accademico esiste, e tutti dobbiamo prenderne atto se vogliamo cambiare la situazione. Nicola, in questi quattro anni abbiamo brindato assieme, corso assieme per centinaia di chilometri e parlato delle cose importanti, condividendo una certa visione della vita. Dobbiamo assolutamente mantenere vive tutte queste tradizioni in futuro, ok? Sergio and Petra, thanks for the amazing moments we spent together on this and the other side of the ocean. I hope it will be soon my turn to host you during your trips to the States! Alessandra e Fabio, ci siamo conosciuti quasi alla fine di questo mio percorso, ma mi sono divertito tantissimo con voi. Grazie per le nostre cene e le nostre uscite e tantissimi auguri per il futuro!

Finally, a special thanks in true *itañol*. Irene, eres così especial que un capítulo entero no sería suficiente para contarlo. Tu iluminas cada día de mi vida y lo vuelves único, nunca dudas de mi capacidades y siempre encuentras la manera de sacarme una sonrisa y alegrarme. Gracias por compartir con migo estos cuatro años, y espero de afrontar este futuro loco y incierto siempre juntos.